

Excess cataloged X-ray and radio sources at galaxy-cluster virial shocks

Gideon Ilani,^{*} Kuan-Chou Hou,[†] and Uri Keshet[‡]

Physics Department, Ben-Gurion University of the Negev, POB 653, Be'er-Sheva 84105, Israel

We detect a highly significant excess of X-ray (2RXS) and radio (NVSS, GMRT, VLSSr) catalog sources when stacked around MCXC galaxy clusters and groups, narrowly confined within $\lesssim 100$ kpc of the $\sim 2.4R_{500}$ virial shock radius (inferred from previous continuum stacking), with similar X-ray ($\sim 4\sigma$ for 443 clusters) and radio ($\sim 4\sigma$ for 485 clusters) characteristics ($> 5\sigma$ joint). The excess sources show 10–100 kpc scales, $L_X(0.1\text{--}2.4\text{ keV}) \simeq 10^{42\text{--}43}\text{ erg s}^{-1}$ or $\nu L_\nu(\nu = 1.4\text{ GHz}) \simeq 10^{40\text{--}41}\text{ erg s}^{-1}$ luminosities, and a preferentially radial radio-polarization. The narrow localization and properties of the excess identify these sources not as AGN, often invoked speculatively for excess X-ray sources at cluster outskirts, but rather as infalling gaseous clumps interacting with the virial shock, probably galactic halos and possibly outflow remnants. The local excess of such discrete, radio-to- γ -ray sources around an object can probe its virial shock also at high redshifts and sub-cluster scales.

1. INTRODUCTION

Several studies have reported a radially-broad excess of X-ray sources in the outskirts of galaxy clusters. These include a $\gtrsim 5\sigma$ excess at $1.5 \lesssim r \lesssim 3$ Mpc radii in stacked *Chandra* data around 24 relaxed, redshift $0.3 < z < 0.7$ MACS clusters [1], a $\sim 4\sigma$ excess at $2 \lesssim r \lesssim 3$ Mpc in stacked *XMM-Newton* data around 22 luminous, $0.9 < z \lesssim 1.6$ clusters [2], and a statistically significant excess at normalized, $2 < \tau \equiv r/R_{500} < 4$ radii in stacked *XMM-LSS* field data around 19 clusters of $0.14 < z < 0.35$ [3]. Here, the subscript 500 refers (henceforth) to the radius around the center of a cluster enclosing a mass density ρ that is 500 times larger than the critical mass density of the Universe. The excess sources were usually assumed to be associated with active galactic nuclei (AGN). Their excess at the cluster periphery was tentatively attributed to an enhanced rate of major galaxy mergers [*e.g.*, 1, 4, and references therein]. Part of the excess was speculated to arise from gravitational lensing of background quasi-stellar objects [3] or from foreground structures [2].

In contrast, other analyses, including larger studies, have found no excess of peripheral sources. In particular, no X-ray source excess was found beyond $r = 1$ Mpc using *Chandra* data around 27 disturbed, $0.3 < z < 0.7$ MACS clusters [1] or 148 clusters of $0.1 < z < 0.9$ [5], and no excess of optical, IR or radio-selected cataloged AGN was found at the outskirts of 2300 infrared-selected clusters [6]. Searches for a source excess performed after normalizing distances to typical cluster scales such as R_{500} did not show a consistent signal, either; for example, a local deficit of X-ray sources was found at $2 < \tau < 3$ around 14 clusters of $0.43 < z < 1.05$ [3].

More recently, a $\sim 3\sigma$ excess of *Chandra* X-ray sources was reported [7] in a fairly narrow, $2 < \tau < 2.5$ range of normalized radii around a small sample of five $z \sim 1$, mostly disturbed clusters. This signal is dominated by two clusters, each with about ten excess $2.0 < \tau < 2.5$ sources with respect to neighbouring bins. The excess sources show $10^{42.5}\text{ erg s}^{-1} \lesssim L_{0.5\text{ keV}}^{8.0\text{ keV}} \lesssim 10^{44}\text{ erg s}^{-1}$ luminosities, where energy or frequency subscripts (superscripts) denote low (high) band limits, henceforth. These sources were again tentatively attributed to enhanced AGN activity associated with excessive galaxy mergers or gas stripping.

However, an excess of AGN over such a narrow range of radii at the outskirts of clusters would be unnatural, especially taking into account projection (and, in other studies, also stacking) effects. Indeed, the rate of galaxy mergers is thought to evolve quite gradually, rising well before the accreted galaxies reach the cluster outskirts, and remaining high after pericentric crossing [*e.g.*, 8]. AGN activity can be affected by the intracluster medium (ICM) through several channels, notably, in this context, by ram pressure stripping of hot halo gas [*e.g.*, 9], but these processes are thought to be important only once the galaxy approaches the central, $r \lesssim 1$ Mpc region of the cluster [8, and references therein].

Therefore, a sharp spike in the radial profile of the density of sources would indicate a localized, sudden change in the environment. Interestingly, the structure formation, or virial, shock of a galaxy cluster, long anticipated to lie in the $2 < \tau < 3$ range according to cosmological simulations [*e.g.*, 10, 11], provides a natural candidate for such a sharp environmental transition. Indeed, as an infalling object crosses the virial shock (VS), it should see the ambient pressure suddenly jump by orders of magnitude as the infalling surrounding plasma is violently slowed down and heated, accompanied by the generation of magnetic fields and shock-accelerated relativistic particles (cosmic rays, CRs) carrying a substantial fraction of the elevated thermal energy. While crossing a VS is unlikely to trigger an AGN, and the processes by which it could lead to the emergence of bright excess X-ray or radio sources may be a-priori unclear, the VS could explain

^{*} Posthumously. Gideon Ilani was killed in action on December 10, 2023. This paper is based on his research.

[†] Institute of Astronomy and Astrophysics, Academia Sinica, PO Box 23-141, Taipei 10617, Taiwan

[‡] keshet.uri@gmail.com

at least the position and sharpness of the signal.

Moreover, recent studies have identified stacked VS signals in precisely the same $2 < \tau < 2.5$ region harboring the excess [7] X-ray sources. Such stacking analyses include a $> 5\sigma$ signal at $2.2 \lesssim \tau \lesssim 2.5$ in *Fermi*-LAT γ -ray data around 112 extended clusters, interpreted as CR electrons (CREs) inverse-Compton (IC) scattering cosmic microwave background (CMB) photons [12, 13]; a $\gtrsim 5\sigma$ synchrotron counterpart at $2.4 \lesssim \tau \lesssim 2.6$ in OVRO-LWA radio data around 44 massive clusters [14]; a significant drop around $2.0 \lesssim \tau \lesssim 2.6$ in *Planck* y -parameter around 10 galaxy groups [15]; and a projected y -parameter drop starting at $\tau \simeq 2$ in South Pole Telescope data around 500 clusters [16]. Such stacked VS signals corroborate the IC, synchrotron, and Sunyaev-Zel'dovich (SZ) signals detected separately or simultaneously in individual nearby clusters [17–20], and roughly coincide with the splashback feature inferred from a localized drop in the logarithmic slopes of galaxy density profiles [21, 22]. Interestingly, stacked data suggest a secondary, weaker and broader IC [13], synchrotron [14], and possibly also SZ [16] signal around $\tau \simeq 6$; if verified, this would suggest an elongated averaged VS morphology of ~ 2.5 ellipticity ratio, as indicated in Coma [17, 18].

Following these VS detections and reports of excess peripheral X-ray sources, we carry out an all-sky analysis of cataloged X-ray and radio sources in the peripheries of galaxy clusters and groups (henceforth clusters, for brevity). To this end, X-ray sources from the Second *ROSAT* All-Sky Survey (RASS) Source Catalog [2RXS; 23] and radio sources from the National Radio Astronomy Observatory (NRAO) Very Large Array (VLA) Sky Survey [NVSS; 24] are stacked around extended clusters selected from the Meta-Catalog of X-ray detected Clusters of galaxies [MCXC; 25]. We find an excess of sources in both catalogs (with respect to the field, dominated by foreground or background sources seen in projection), with striking similarities between X-ray and radio signals, localized surprisingly narrowly near the predetermined VS radius. The radio signal is verified also in the Giant Metrewave Radio Telescope (GMRT) All-Sky 150 MHz [26], and the Very Large Array (VLA) Low-Frequency (74 MHz) Sky Survey Redux (VLSSr) [27] source catalogs, used to estimate the radio-source spectra. We then statistically characterize the properties of the excess sources, and constrain the physical processes by which the VS could lead to such a local excess of X-ray and radio sources.

The paper is organized as follows. We describe the cluster and source catalogs, along with our selection criteria, in §2, and outline our stacking and modelling methods in §3. The results are presented and phenomenologically modelled in §4. The properties of the excess sources are inferred statistically in §5, and their physical origin is explored in §6. Finally, our results are summarized and discussed in §7.

The Supplementary material provides supporting and auxiliary information regarding the spectra of the excess

X-ray sources (§A), limitations on source size estimates (§B), the evaluation of excess confidence levels (CLs) under Poisson statistics (§C), various convergence and sensitivity tests (§D), additional properties of the excess sources (§E), and the absence of a significant VS signal from 2RXS–NVSS pairs (§F) or identified AGN (§G). All (field+excess) sources found near the VS are listed in §H.

We adopt a Λ CDM cosmological model with a Hubble constant $H_0 = 68 \text{ km s}^{-1} \text{ Mpc}^{-1}$, a mass fraction $\Omega_m = 0.3$, and a 76% hydrogen mass fraction, yielding a mean particle mass $\bar{m} \simeq 0.59 m_p$. The center of a galaxy cluster is defined as its X-ray peak, and an adiabatic index $\Gamma = 5/3$ is assumed for the ICM. Confidence intervals are 68% containment projected for one parameter.

2. DATA PREPARATION

Here, we describe the catalogs and our data preparation procedure. The MCXC cluster catalog is discussed in §2A, the 2RXS catalog of X-ray sources (subscript X) in §2B, and the NVSS radio catalog (subscript ν) in §2C. Table I summarizes the main properties of the catalogs.

A. Cluster catalog and selection criteria

The MCXC catalog of galaxy clusters [25], based on a compilation of the *ROSAT* all-sky survey and *ROSAT* serendipitous catalogs, is particularly suitable for our purposes as it facilitates a uniform normalization to a fixed overdensity. The catalog, with 1743 nearby clusters, was used in previous stacking analyses [13, 14], and provides the redshift and characteristic length scale R_{500} of each cluster, so the corresponding angular scale θ_{500} can be estimated.

We apply the following nominal cuts to the MCXC, in order to select the clusters most suitable for source stacking and to avoid contaminations.

1. Sufficiently extended clusters to resolve the virial ring. The source catalog resolutions are $45''$ (FWHM in radio) and $\sim 2'$ (detection cell in X-rays), whereas the thickness of the virial ring in continuum emission was estimated as $\sim \theta_{500}/3$ [13, 14], so we conservatively require $\theta_{500} > 3 \cdot 2' = 6'$. This cut is independently justified as it coincides with the MCXC turnaround angle, below which the number of detected clusters diminishes.
2. Clusters that are less extended than typical foreground structures. The power spectrum of sources in the 2RXS (NVSS) catalog shows substantial structure on $\gtrsim 3^\circ$ ($\gtrsim 1^\circ$) scales, suggesting extended foregrounds. To avoid contaminating the VS region with such putative structures, we impose an upper, $\theta_{500} \leq 0.3$ limit.
3. Sufficiently massive galaxy groups. In order to focus on galaxy clusters and rich galaxy groups, but

avoid individual galaxies and poor groups which may not show the same type of peripheral sources, we impose a lower $M_{500} \geq 10^{13} M_{\odot}$ mass limit.

4. Avoiding confusion in regions of a high sky-projected density of clusters. The MCXC shows such high densities, with nearly overlapping projected virial radii, in two regions, around Galactic coordinates $\{l, b\} \sim \{315^{\circ}, 32^{\circ}\}$ and $\sim \{12^{\circ}, 50^{\circ}\}$ [13]. We avoid these regions, by excluding all clusters within 5° of these two sky positions. This cut is in practice redundant, as the other cuts already exclude all clusters in these two busy regions.
5. Avoiding large Galactic structures. The Loop-I and Fermi bubble regions are excluded from the nominal analysis, to avoid any possible effects they may have on the catalogs. For this purpose, we adopt simplified models of these two structures. Loop-I is modeled as a disk centered on $\{l, b\} = \{329, 17.5\}$, with a radius of 55° [e.g. 28, 29]. The Fermi bubble is crudely modeled as the region defined by $|b| \leq 55^{\circ}$ and either $l < 30^{\circ}$ or $l > 330^{\circ}$.
6. Additional cuts are imposed on the Galactic latitude $|b|$, to avoid the bright Galactic plane, and on the declination, Dec. These cuts are specific to each source catalog, so are detailed below.

The above cuts leave a reduced sample of $N_{c,X} = 443$ clusters for stacking X-ray sources, and a sample of $N_{c,\nu} = 485$ clusters for radio stacking. These clusters have redshifts in the range $0.017 < z < 0.24$, and masses in the range $10^{13} M_{\odot} < M_{500} < 9 \times 10^{14} M_{\odot}$; these and additional sample properties are provided in Table I. The MCXC includes ~ 50 (~ 90) clusters which harbour an-

other MCXC cluster inside (twice) their virial radius, about 80%–90% of which survive our cluster cuts. These clusters with nearby neighbours are not excluded from our nominal analysis, but we verify in §D that excluding close pairs does not alter our results significantly.

B. X-ray source catalog and cuts

The 2RXS catalog is most suitable for stacking X-ray sources, as it is presently the deepest and cleanest X-ray all-sky survey available [23]. The catalog is based on RASS observations using the position-sensitive proportional counter (PSPC), providing $\sim 1.3 \times 10^5$ sources in the $[0.1, 2.4]$ keV energy range. The projected density n_X of X-ray sources on the sky is shown in Fig. 1 (left panel). Table I summarizes some relevant properties of the catalog and its sources (in column 3).

Softer X-rays undergo more photo-absorption by neutral hydrogen atoms in the Galaxy. The resulting optical depth exceeds unity for $\epsilon \simeq 0.1$ keV photons at $|b| \lesssim 30^{\circ}$ Galactic latitudes. Therefore, for the nominal X-ray analysis, we place an extended cut on the Galactic latitude of the clusters, retaining only those with $|b| \geq 30^{\circ}$.

The number of sources in a catalog diminishes as one increases the threshold on the minimal likelihood \mathcal{L} of source detection, defined such that the false-positive source probability is $e^{-\mathcal{L}}$. The decline in the fraction of spurious sources as \mathcal{L} increases has been estimated using simulations [23]. The 2RXS catalog compromises on $\mathcal{L} \geq 6.5$, corresponding to $\gtrsim 3\sigma$ source detection with a $\sim 30\%$ fraction of spurious sources in the catalog. Aiming for a smaller, $\sim 10\%$ fraction of spurious sources, we adopt $\mathcal{L} \geq 8$ in our nominal analysis, corresponding to $\gtrsim 3.4\sigma$ source detection.

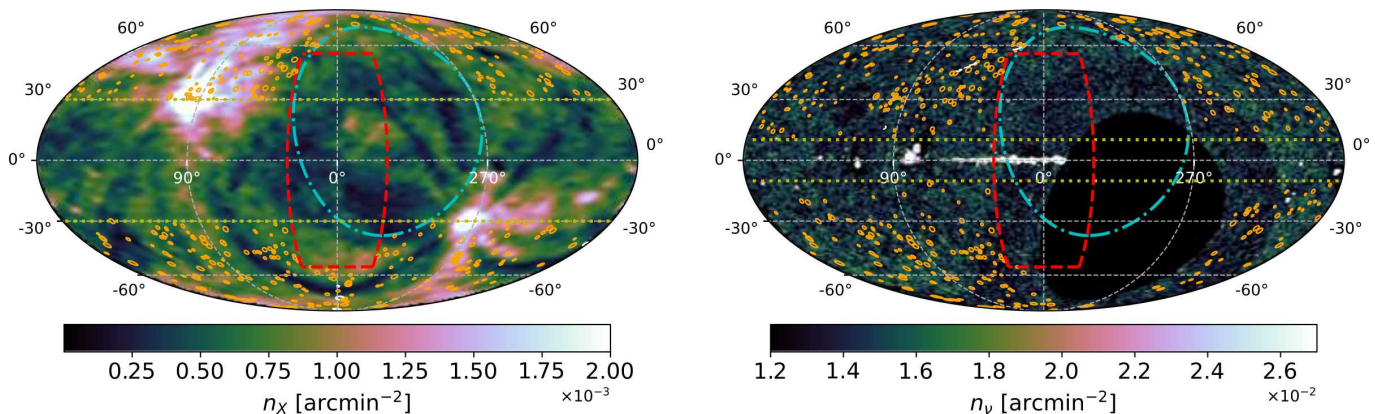


FIG. 1. Hammer-Aitoff all-sky projection of source density (cubehelix [30] color map) and cluster sample (orange circles of radius $5\theta_{500}$), for X-ray (left panel; 2RXS) and radio (right panel, NVSS; note diminished exposure at low declinations, with no Dec $< -40^{\circ}$ sources) analyses. Also shown are the cuts of the Galactic plane (dotted yellow lines), the Fermi bubbles (dashed red curves), and Loop-I (dot-dashed cyan).

TABLE I. Catalog and stacking properties.

	Property	Symbol	2RXS	NVSS
Catalog	Photon range	ϵ, ν	0.1–2.4 keV	1.44 ± 0.05 GHz
	Sky coverage		All-sky	Dec $> -40^\circ$ (82% sky)
	Minimal flux ^a	F_{\min}	10^{-13} erg s ⁻¹ cm ⁻²	3.4 mJy (99% compl.)
	Detection threshold		$\mathcal{L} > 6.5$	$I_\nu > 2$ mJy beam ⁻¹
	Base map resolution		$\sim 45''$ (pixel size)	45'' (FWHM)
	Source size (see §B)	$r, \{a, b\}$	$r \geq r_{psf} \simeq 40''$	$14'' < 2b < 2a < 286''$
	Total source number		1.3×10^5	1.8×10^6
Cuts	Latitude cut	b	$ b > 30^\circ$	$ b > 10^\circ$
	Cluster declination cut	Dec	—	Dec $> -35^\circ$
	Source flux ^a cut	F_X^*	$F_X < F_X^* \equiv 7 \times 10^{-12}$ erg s ⁻¹ cm ⁻²	$F_\nu > F_\nu^* \equiv 100$ mJy
	Source likelihood cut	\mathcal{L}	$\mathcal{L} > 8$	—
Clusters ^b	Number of clusters	N_c	$N_{c,X} = 443$	$N_{c,\nu} = 485$
	Redshift median (range)	z	0.077 (0.017–0.228)	0.081 (0.017–0.233)
	Angular radius median (range)	θ_{500}	$0^\circ.15$ ($0^\circ.10$ – $0^\circ.30$)	$0^\circ.14$ ($0^\circ.10$ – $0^\circ.30$)
	Mass median (range)	M_{500}	1.5 (1.0 – 8.7) $\times 10^{14} M_\odot$	1.6 (1.0 – 9.0) $\times 10^{14} M_\odot$
Results ^b	Mean field source density	f	5360 sr ⁻¹	5760 sr ⁻¹
	ICM-region sources (expected field)	$\mathcal{N}(\mathcal{F})$	107 (~ 82)	102 (~ 92)
	VS-region sources (expected field)	$\mathcal{N}(\mathcal{F})$	119 (~ 77)	128 (~ 87)
	VS SW-overdensity (significance)	δ_{SW}	0.54 (4.4σ Poisson-corrected)	0.47 (4.0σ)

^a — Energy flux (specific energy flux) in X-rays (radio). The cuts are explained in the text.

^b — After cuts. Source numbers \mathcal{N} are summed over all clusters. VS sources are listed in §H.

We define the X-ray energy flux $F_X \equiv F_{0.1 \text{ keV}}^{2.4 \text{ keV}}$ as the specific flux F_ϵ integrated over the *ROSAT* band. The catalog provides flux estimates based on three different emission models: a power-law spectrum, the optically-thin thermal plasma emission model Mekal [31], and optically thick, black-body emission. In most or all relevant cases, the model fits are not sufficiently accurate to identify which emission model is most appropriate. Therefore, we henceforth adopt the power-law estimate of F_X , which is a simpler fit available for the largest number of sources; our results are not sensitive to this choice (see §D). We nevertheless consider below the fitted source temperatures, as well as the fitted photon power-law index Γ_X defined by $F_\epsilon \propto \epsilon^{1+\Gamma_X}$.

X-ray sources in the analyzed sky region. The 2RXS catalog is dominated by foreground sources brighter than the stacked clusters themselves. To reduce foreground confusion, we impose an upper flux limit that removes sources whose luminosities would exceed the typical, $L_X \simeq 10^{45}$ erg s⁻¹ luminosity of the entire ICM even around the most distant ($z_{\max} \simeq 0.23$) clusters in our sample, thus retaining only $F_X < F_X^* \equiv 7 \times 10^{-12}$ erg s⁻¹ cm⁻² sources. Note that this F_X^* cutoff is already quite close to the 2RXS $\sim 10^{-13}$ erg s⁻¹ cm⁻² sensitivity threshold [23]. In §D, we show that our results are not sensitive to the precise choice of flux cut; for example, a high $F_X^* = 10^{-10}$ erg s⁻¹ cm⁻² changes the significance of excess virial sources by only $\sim 2\%$. In fact, a significant, $\sim 4\sigma$ signal persists even with no flux cut at all, despite the strong foreground.

Figure 2 (left panel) shows the energy flux histogram of

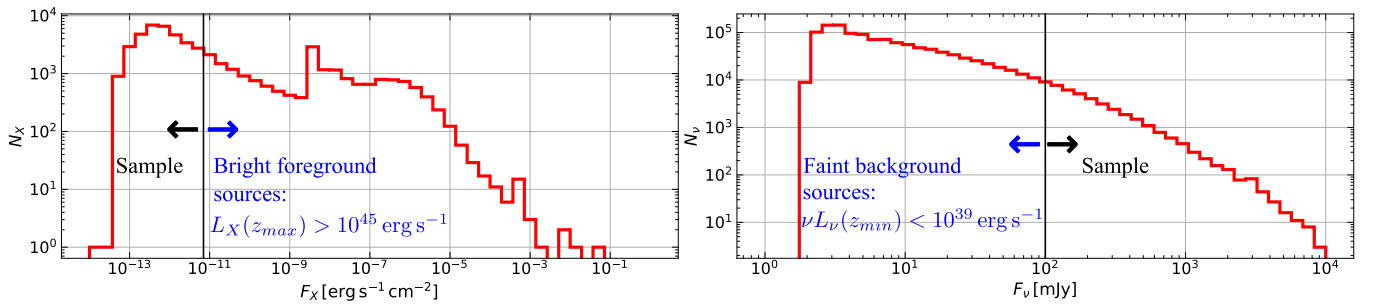


FIG. 2. The logarithmic energy flux F_X (specific flux F_ν) histogram of 2RXS (NVSS) sources in the analyzed sky is shown in the left (right) panel, along with our nominal flux thresholds (black vertical lines with explanatory labels). Our results are not sensitive to the precise choice of thresholds; see text.

C. Radio source catalog and cuts

We use the extensive NVSS catalog for radio sources, unless otherwise stated. This catalog covers only $\sim 82\%$ of the sky, but radio waves are not substantially absorbed in the galaxy, so the catalog can be used at lower latitudes than in X-rays. Consequently, NVSS allows for the stacking of a similar and even slightly larger number of clusters than with 2RXS. The projected density n_ν of catalog radio sources on the sky is shown in Fig. 1 (right panel). Table I summarizes some relevant properties of the catalog and of its sources (in column 4).

The NVSS catalog covers the northern sky at declinations $\text{Dec} > -40^\circ$ (J2000). Figure 1 shows an apparent decline in n_ν with decreasing Dec even somewhat north of this declination. Therefore, we impose a corresponding cut on the declination of clusters used for radio stacking, nominally keeping only those with $\text{Dec} > -35^\circ$.

While Galactic absorption does not impose a substantial difficulty at the 1.4 GHz frequency of the NVSS, there is a marked excess of Galactic foreground sources at $|b| \lesssim 3^\circ$. To avoid these sources, we place a conservative cutoff on the latitudes of clusters used in the radio analysis, retaining only those with $|b| \geq 10^\circ$.

The NVSS catalog does not provide information concerning the likelihood of radio source detection, but it does impose a minimal $L_\nu > 2 \text{ mJy beam}^{-1}$ intensity threshold, leading to a specific flux (*i.e.* spectral flux density) distribution with $F_\nu \gtrsim 2.5 \text{ mJy}$; for sources above 3.4 mJy, the NVSS completeness is 99% [24].

A histogram of the specific flux of NVSS sources is shown in the right panel of figure 2. This catalog is strongly dominated by faint background sources (in contrast to the bright foreground source of 2RXS), due in part to star-forming galaxies, whose luminosity function peaks near $\nu L_\nu \sim 10^{39} \text{ erg s}^{-1}$ [*e.g.*, 32]; for the most part, these sources are not expected to be associated with the low-redshift clusters in our sample. We therefore impose a lower specific-flux limit that removes sources with luminosities lower than this peak luminosity even around the nearest ($z_{\min} \simeq 0.017$) clusters in our sample, thus retaining only sources of $F_\nu \gtrsim F_\nu^* \equiv 100 \text{ mJy}$. In §D, we show that changing the radio flux cutoff by 50% has only a $\sim 15\%$ effect on the significance of our results, and our choice is conservative. Interestingly, the signal persists even if one avoids a flux cut entirely, thus retaining the large number of faint background sources, but expectedly diminishes to the $\sim 2\sigma$ level.

3. STACKING ANALYSIS METHOD

We normalize sky distances around each cluster by its θ_{500} , radially bin the data onto circular annuli about the center of the cluster, and stack the resulting normalized, binned, radial distribution over all clusters in the sam-

ple. Stacking is performed for X-ray and radio sources separately, although we later consider also the joint distribution and the significance of the joint excess. The following procedure thus pertains separately to the stacking of 2RXS and NVSS sources, as well as GMRT and VLSSr sources considered later.

For each cluster, we define the normalized radius $\tau \equiv \theta/\theta_{500}$, where θ is the angular distance from the center of the cluster. Alternatively, in order to generate stacked 2D maps (shown in §4 and in §D), *i.e.* without radial binning, we replace τ by its two-dimensional analog $\boldsymbol{\tau} \equiv \{\tau_x, \tau_y\}$. For the purpose of stacking, we define the region of interest (ROI) as $\tau < \tau_{\max} = 10$, choosing τ_{\max} to be about four times larger than the VS radius inferred from stacking *Fermi*-LAT or LWA data. Our results are not sensitive to the choice of τ_{\max} and all other stacking parameters, as shown in §D.

In order to test for a putative local excess of sources and determine its significance, one must estimate the sky-projected density of background or foreground sources, henceforth referred to colloquially as field sources, in the vicinity of each cluster. In our nominal approach, we consider a fixed projected density of field sources around each cluster, measured outside its ROI, in the so-called field region defined by $\theta_{\min} < \theta < \theta_{\max}$. We choose $\theta_{\min} = 3^\circ$ slightly larger than the ROI radius, *i.e.* $\theta_{\min} > \tau_{\max}\theta_{500}$, of any cluster in our sample. We take $\theta_{\max} = 5^\circ$ sufficiently larger than θ_{\min} , for good statistics and to overcome foreground fluctuations over $\gtrsim 1^\circ$ scales. Alternative choices of $[\theta_{\min}, \theta_{\max}]$, as well as more elaborate, non-constant field models, are examined in §D.

When testing for virial-shock signals, it can be useful to examine, in addition to the field region outside the VS, also the region just inward of the shock, beyond its range of influence. For this purpose, we designate the range $1.0 < \tau < 1.5$ as a so-called ICM region. The upper limit on this region is chosen sufficiently far from the virial radius to reduce the projected effects of the shock. The lower limit is chosen to balance sufficient statistics with limited evolutionary effects and central-source contamination.

For a typical $\Delta\theta \sim \theta_{500}/3$ resolution for X-ray sources (and \sim twice better resolution for radio sources) around our least extended clusters, and for consistency with [13] and [14], we designate $\Delta\tau = 0.25$ as our nominal radial bin size, but explore also smaller and larger bins. We therefore designate the anticipated VS region as the $2.25 < \tau < 2.5$ bin, where the strongest VS signal is expected based on continuum γ -ray [13] and radio [14] detections in stacked MCXC clusters.

For each catalog, τ bin, and cluster \mathbf{c} , we compute the solid angle $\Delta\Omega(\tau, \mathbf{c})$ and number $\mathcal{N}(\tau, \mathbf{c})$ of sources falling within the bin. The dimensionless projected density of catalog sources can now be estimated as

$$n(\tau, \mathbf{c}) = \frac{\mathcal{N}(\tau, \mathbf{c})}{\Delta\Omega(\tau, \mathbf{c})}, \quad (3.1)$$

where

$$\Delta\omega(\tau, \mathbf{c}) \equiv \frac{\Delta\Omega(\tau, \mathbf{c})}{\theta_{500, \mathbf{c}}^2} \quad (3.2)$$

is the solid angle normalized to a square θ_{500}^2 pixel. The number $\mathcal{F}(\tau, \mathbf{c})$ of field sources anticipated in the bin is extrapolated from the field region, giving the analogous dimensionless projected field density

$$f(\tau, \mathbf{c}) = \frac{\mathcal{F}(\tau, \mathbf{c})}{\Delta\omega(\tau, \mathbf{c})}, \quad (3.3)$$

and the implied fractional overdensity

$$\delta(\tau, \mathbf{c}) \equiv \frac{\mathcal{N}(\tau, \mathbf{c}) - \mathcal{F}(\tau, \mathbf{c})}{\mathcal{F}(\tau, \mathbf{c})} = \frac{n(\tau, \mathbf{c}) - f(\tau, \mathbf{c})}{f(\tau, \mathbf{c})}. \quad (3.4)$$

In our nominal, uniform field model, with a constant dimensionless projected density $f(\mathbf{c})$ around each cluster \mathbf{c} , the field distribution becomes $\mathcal{F}(\tau, \mathbf{c}) = f(\mathbf{c})\Delta\omega(\tau, \mathbf{c})$.

In the $\mathcal{F} \gg 1$ limit, one may approximate its distribution as normal, as we verify using control cluster samples in §3C. We may then infer the Z-test significance of any $\mathcal{N} > \mathcal{F}$ excess with respect to the field-only null hypothesis,

$$S \simeq \frac{\mathcal{N} - \mathcal{F}}{\sqrt{\mathcal{F}}}. \quad (3.5)$$

In practice, individual cluster bins at small radii typically show $\mathcal{F} < 1$, so the significance S should be estimated from Poisson statistics (see §C) or from control clusters (see §3C). One may co-add the $N_{\text{cat}} = 2$ catalogs, similarly estimating the joint Z-test significance

$$S_{\text{joint}} \simeq \frac{1}{\sqrt{N_{\text{cat}}}} \sum_i^{N_{\text{cat}}} S_i, \quad (3.6)$$

where S_i is the significance profile in each catalog.

There is some freedom in the method in which these quantities may be stacked over clusters. Following previous MCXC stacking analyses [13, 14], we consider two extremes. In the so-called source-weighted (SW) co-addition method, discussed in §3A, direct quantities (source numbers, solid angles) are stacked separately over all clusters and then combined to infer derived quantities (source densities, overdensities, excess significance levels). In the cluster-weighted (CW) co-addition method, discussed in §3B, derived quantities are first computed on a cluster-by-cluster basis, and only subsequently stacked. The results in §4 show good agreement between the two methods in the VS region, indicating that many clusters contribute fairly evenly to the stacked signal.

The nominal significance levels S obtained above and below, based on approximating the distribution as normal and using standard error propagation, are generalized for Poisson statistics (see §C), and tested using samples of control clusters, as described in §3C. We present simplified models for the radial dependence of the excess in §3D, and discuss in §3E the procedure of fitting these models to the data and assessing them using the TS-test.

A. Source-weighted co-addition

The SW stacking method assigns an equal weight to each source, rather than to each cluster. In each normalized angular τ bin, we thus separately co-add, over all clusters, both the number of sources,

$$\mathcal{N}(\tau) \equiv \sum_{\mathbf{c}=1}^{N_c} \mathcal{N}(\tau, \mathbf{c}), \quad (3.7)$$

and the solid angle

$$\Omega(\tau) \equiv \sum_{\mathbf{c}=1}^{N_c} \Delta\Omega(\tau, \mathbf{c}), \quad (3.8)$$

where N_c is the number of clusters in the sample.

The dimensionless projected number density of sources, co-added over clusters in the bin τ , can now be computed as

$$n_{\text{sw}}(\tau) = \frac{\mathcal{N}(\tau)}{\bar{\omega}(\tau)}, \quad (3.9)$$

where the dimensionless $\bar{\omega}(\tau) \equiv \Omega(\tau)/\bar{\theta}_{500}^2$ is obtained by normalizing to the mean $\bar{\theta}_{500}^2 \equiv N_c^{-1} \sum_{\mathbf{c}} \theta_{500, \mathbf{c}}^2$; this normalization has no effect on our subsequent results. The statistical uncertainty in n_{sw} may be estimated as

$$\sigma[n_{\text{sw}}(\tau)] \simeq \frac{\sqrt{\mathcal{N}(\tau)}}{\bar{\omega}(\tau)}. \quad (3.10)$$

Source-weighted estimates such as $n_{\text{sw}}(\tau)$ are somewhat skewed toward extended clusters or clusters in strong-field regions, which may harbour a larger number of sources and so may dominate the numerator of Eq. (3.9). This bias is offset in part by the comparable extents of all clusters in our sample, and by avoiding regions with known contaminations.

The above approach is applied analogously to field sources, modelled with some distribution $\mathcal{F}(\tau, \mathbf{c})$ based on the field region. In analogy with Eqs. (3.7)–(3.9), the co-added number of field sources is

$$\mathcal{F}(\tau) \equiv \sum_{\mathbf{c}=1}^{N_c} \mathcal{F}(\tau, \mathbf{c}), \quad (3.11)$$

with co-added dimensionless projected density

$$f_{\text{sw}}(\tau) = \frac{\mathcal{F}(\tau)}{\bar{\omega}(\tau)}. \quad (3.12)$$

The significance of a local excess of sources with respect to the field-only null hypothesis can now be estimated as in Eq. (3.5),

$$S_{\text{sw}}(\tau) = \frac{\mathcal{N}(\tau) - \mathcal{F}(\tau)}{\sqrt{\mathcal{F}(\tau)}}, \quad (3.13)$$

in the $\mathcal{F}(\tau) \gg 1$ limit of a normal distribution.

Finally, the overdensity δ_{sw} of sources with respect to the field can be estimated as

$$\delta_{\text{sw}}(\tau) = \frac{n_{\text{sw}}(\tau)}{f_{\text{sw}}(\tau)} - 1, \quad (3.14)$$

with an associated uncertainty

$$\begin{aligned} \sigma[\delta_{\text{sw}}(\tau)] &\simeq \frac{n_{\text{sw}}(\tau)}{f_{\text{sw}}(\tau)} \sqrt{\frac{\mathcal{N}(\tau) + \mathcal{F}(\tau)}{\mathcal{N}(\tau)\mathcal{F}(\tau)}} \\ &\simeq [1 + \delta_{\text{sw}}(\tau)] \sqrt{\frac{2}{f_{\text{sw}}(\tau)\bar{\omega}(\tau)}}. \end{aligned} \quad (3.15)$$

The second approximation holds when the excess is small compared to the field; it is shown here for completeness, but is not used in practice below.

B. Cluster-weighted co-addition

The CW stacking method assigns the same weight to each cluster, rather than to each source. In a given cluster \mathbf{c} , the significance of a local excess of sources with respect to the field-only null hypothesis is estimated as

$$S(\tau, \mathbf{c}) \simeq \frac{\mathcal{N}(\tau, \mathbf{c}) - \mathcal{F}(\tau, \mathbf{c})}{\sqrt{\mathcal{F}(\tau, \mathbf{c})}}. \quad (3.16)$$

Under the null hypothesis, we may approximate $S(\tau, \mathbf{c})$ as a random variable of zero mean and unit standard deviation. The CW co-added significance of the excess over the field may now be estimated as

$$S_{\text{cw}}(\tau) = \frac{1}{\sqrt{N_c}} \sum_{\mathbf{c}=1}^{N_c} S(\tau, \mathbf{c}). \quad (3.17)$$

Cluster-weighted estimates are somewhat skewed by clusters with low field values, where $|S(\tau, \mathbf{c})|$ can have artificially large values.

In the same method, we co-add densities over the sample of clusters to obtain the average stacked dimensionless projected density

$$n_{\text{cw}}(\tau) = \frac{1}{N_c} \sum_{\mathbf{c}=1}^{N_c} n(\tau, \mathbf{c}), \quad (3.18)$$

with the associated uncertainty

$$\sigma[n_{\text{cw}}(\tau)] = \frac{1}{N_c} \sqrt{\sum_{\mathbf{c}=1}^{N_c} \frac{n(\tau, \mathbf{c})}{\Delta\omega(\tau, \mathbf{c})}}. \quad (3.19)$$

The co-added dimensionless projected density of field sources then become

$$f_{\text{cw}}(\tau) = \frac{1}{N_c} \sum_{\mathbf{c}=1}^{N_c} f(\tau, \mathbf{c}). \quad (3.20)$$

The local overdensity of sources above the field may be defined in each cluster as

$$\delta(\tau, \mathbf{c}) = \frac{n(\tau, \mathbf{c})}{f(\tau, \mathbf{c})} - 1, \quad (3.21)$$

so the stacked overdensity is

$$\delta_{\text{cw}}(\tau) = \frac{1}{N_c} \sum_{\mathbf{c}=1}^{N_c} \delta(\tau, \mathbf{c}), \quad (3.22)$$

with an associated uncertainty

$$\sigma[\delta_{\text{cw}}(\tau)] = \frac{1}{N_c} \sqrt{\sum_{\mathbf{c}=1}^{N_c} \frac{n^2(\tau, \mathbf{c})}{f^2(\tau, \mathbf{c})\mathcal{N}(\tau, \mathbf{c})}}, \quad (3.23)$$

where we neglected fluctuations in \mathcal{F} .

C. Poisson and control sample simulations

In the absence of any signals and source correlations, the statistical distribution of the small number of source counts in each radial bin within each cluster would follow a Poisson distribution, with a source density fixed by the foreground. However, the statistical significance and uncertainty estimates in Eqs. (3.5)–(3.6), (3.10), (3.15)–(3.17), (3.19), and (3.23) invoke, for simplicity, normally-distributed foreground counts. We run Monte-Carlo Poisson simulations to test and correct for this non-Poissonian approximation. Such simulations do not, however, capture structures and correlations in the actual catalogs. We therefore study, in addition, the statistics of the actual catalog sources around a large number of control (or mock) cluster samples, in order to test for systematics and validate our method.

Our Monte-Carlo Poisson simulations involve drawing, from a Poisson distribution, 10^6 random foreground source-counts for each τ bin in each cluster, based on the estimated foreground source-density $\mathcal{F}(\tau, \mathbf{c})$ of the cluster in each catalog. These counts represent $\mathcal{N}(\tau, \mathbf{c})$ under the field-only null hypothesis.

The control sample analysis is based on $\sim 10^6$ samples of control clusters for each catalog, each such sample including N_c clusters with the same θ_{500} values as in the real cluster sample, but placed in random positions within the allowed, *i.e.* non-masked, part of the sky. We stack the real catalog sources around each such control cluster, and calculate the corresponding distributions of foreground and excess source properties, just as in the real sample.

For both Monte-Carlo simulations and control-sample tests, we then study the resulting distributions of $S(\tau)$ values, each quantifying the significance of the putative excess above the foreground in a particular instance. Figure 3 shows the $\pm 1\sigma, \pm 2\sigma, \dots$ CLs of S around the median of its distribution, as inferred from the corresponding 68%, 95%, \dots containment values. These CLs are shown

based on both Poisson simulations and control samples, for both X-ray and radio catalogs, using both SW and CW stacking methods.

As expected, the results approach Eqs. (3.13) and (3.17) at large τ , where $\mathcal{F} \gg 1$, but deviate substantially at small τ . The deviations are particularly large for $\mathcal{N} < \mathcal{F}$ source deficits, but we are mostly interested in the $S > 0$ significance of a positive excess. The approximate agreement of the $S = 0, +1, +2 \dots$ curves with the corresponding Poisson and control-sample containment fractions confirms that our nominal §3A and §3B estimates capture the significance of the excess reasonably well, with small errors ΔS in S . Quantitatively, for the relevant, $\tau > 1$ range, we find modest, $|\Delta S|/S \lesssim 10\%$ fractional errors, except for radio CW stacking where $|\Delta S|/S \lesssim 15\%$. While small, this ΔS should be accounted for at the VS region.

Much of the ΔS difference is attributed to the inaccurate normal-distribution approximation of Poisson statistics. Indeed, the Poisson and control-sample es-

timates are in much better agreement with each other, for both positive and negative S , and even for $\tau < 1$. The difference ΔS between them is very small in X-rays, where $|\Delta S|/S \simeq 4\%$ ($|\Delta S|/S \simeq 2\%$) for $S > 0$ ($S < 0$), and is acceptable for radio SW stacking, where $|\Delta S|/S \simeq 6\%$ ($|\Delta S|/S \simeq 2\%$). For these cases, we henceforth apply an analytic correction (§C), correcting our nominal-distribution estimates for Poisson statistics; the relevant Eqs. (C.1)–(C.2) are shown to accurately follow the simulated Poisson results in Fig. 3. The overall agreement between Poisson and control-sample results indicates that systematic effects and correlations are weak, and our Poisson-statistics estimates are reliable.

For radio CW stacking, however, Poisson and control-sample estimates differ by a more substantial $\Delta S/S \simeq 10\%$ ($\Delta S/S \simeq 3\%$) for $S > 0$ ($S < 0$), perhaps due to extended sources or sidelobes misidentified as multiple sources. In this case, we henceforth interpolate the control-sample CLs in order to obtain a more accurate estimate of S .

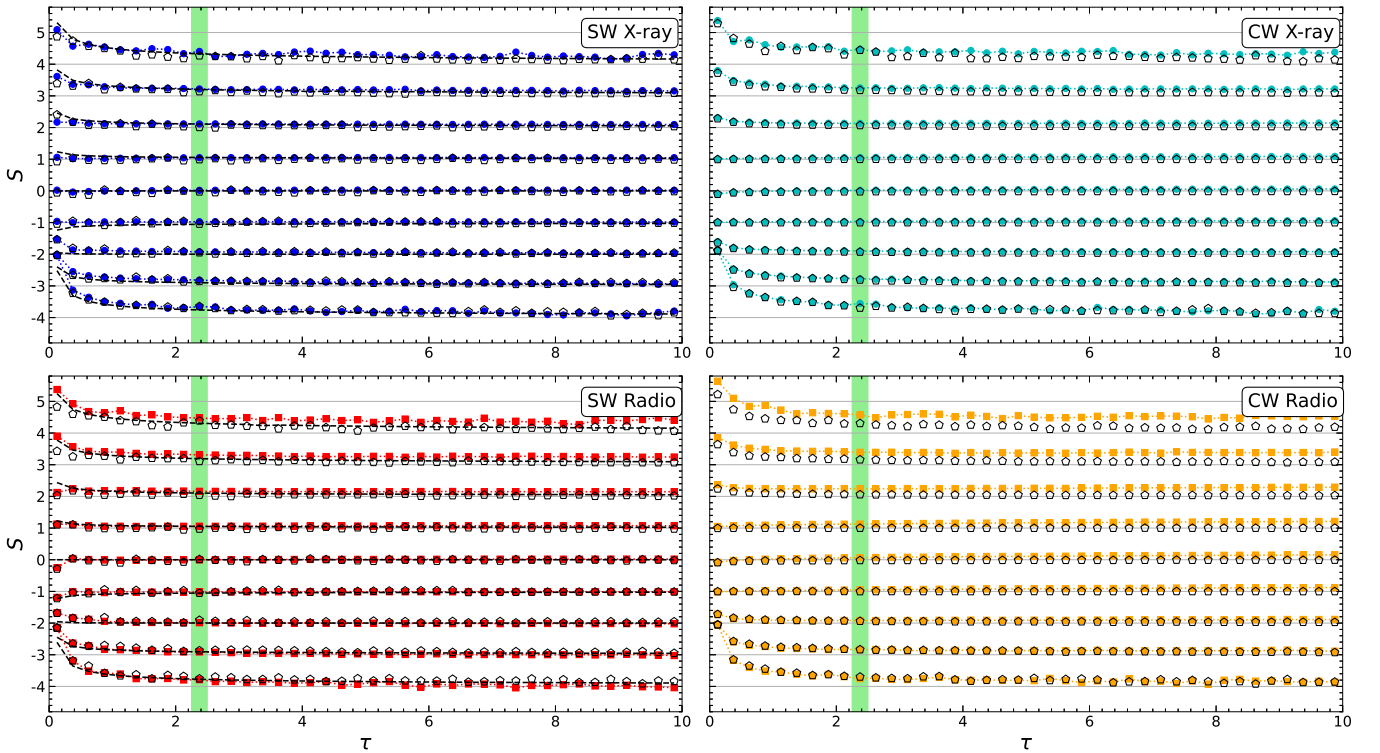


FIG. 3. Statistical foreground analysis of SW (left panels) and CW (right) stacked X-ray (upper panels) and radio (bottom) sources. The $\pm 1, \pm 2, \pm 3, \dots$ CLs of control sample (filled colored symbols with dotted guides to the eye) and Poisson distribution estimates (black; empty symbols are Monte-Carlo simulations, dashed lines are the SW analytic approximation of §C) with respect to their median are plotted as a function of the normalized radius $\tau \equiv \theta/\theta_{500}$ from the center of the cluster, against our nominal, normal-distribution approximation $S(\tau)$ (thin solid horizontal lines with left ticks). The anticipated VS region (the $2.25 < \tau < 2.5$ bin of previous γ -ray [13] and radio [14] stacked detections) is highlighted (vertical green shading).

D. Stacked source-excess models

For a significant $S > 0$ excess, we use the TS-test to determine the CL at which the foreground-only null hypothesis is rejected in favor of one of two simple, effective models for the projected, dimensionless source-density $n(\tau)$: (i) a planar model, of a 2D ring around the cluster oriented within the plane of the sky; and (ii) a shell model, obtained by projecting a spherical 3D shell around the cluster.

For the planar model, we take $n(\tau)$ proportional to a 2D Gaussian of peak radius τ_{sh} and width $\Delta\tau_{\text{sh}}$, giving the three-parameter model

$$n_{\text{planar}}(\tau) \equiv \frac{n_0\tau_{\text{sh}}}{\sqrt{8\pi}\Delta\tau_{\text{sh}}^2} \exp\left[-\frac{(\tau - \tau_{\text{sh}})^2}{2\Delta\tau_{\text{sh}}^2}\right]. \quad (3.24)$$

The prefactor is chosen such that in the $\Delta\tau_{\text{sh}} \rightarrow 0$, thin-ring limit, a normalized solid-angle integration yields

$$\int n(\tau) d\omega \simeq \pi\tau_{\text{sh}}^2 n_0 \quad (3.25)$$

sources inside the VS. Here, $d\omega$ is the solid-angle element $d\Omega$ normalized by either θ_{500}^2 (for SW) or $\theta_{500,c}^2$ (CW), and n_0 is a constant dimensionless source density.

For the shell model, it suffices for our purposes to consider a zero-width 3D shell, giving upon projection the two-parameter model [e.g., 18]

$$n_{\text{shell}}(\tau) \equiv \frac{n_0\tau_{\text{sh}}\Theta(\tau_{\text{sh}} - \tau)}{2\sqrt{\tau_{\text{sh}}^2 - \tau^2}}, \quad (3.26)$$

where Θ is the Heaviside step function. The normalization is chosen to again satisfy Eq. (3.25), to facilitate a meaningful comparison of n_0 in the two models.

E. Model fitting and TS-Test

We estimate the best-fit model parameters by a least-squares procedure. In general, one may minimize

$$\chi^2 \simeq \sum_{\tau,c} \frac{[\mathcal{N}(\tau,c) - \mathcal{F}(\tau,c) - \mathcal{M}(\tau,c)]^2}{\mathcal{F}(\tau,c) + \mathcal{M}(\tau,c)}, \quad (3.27)$$

where $\mathcal{M}(\tau,c)$ is the model excess at radial bin τ in cluster c , and we exclude (henceforth) the innermost, $\tau < 1.5$ bins, to avoid the noisy centers of clusters. However, clusters typically have some inner bins with no sources at all, so the above quantity is not well-approximated by a χ^2 distribution. We therefore consider figures of merit based on the stacked quantities.

For SW stacking, we consider $\mathcal{N}(\tau)$, already co-added over clusters, as the relevant random variable, leading to

$$\chi_{\text{sw}}^2 \simeq \sum_{\tau} \frac{[\mathcal{N}(\tau) - \mathcal{F}(\tau) - \mathcal{M}(\tau)]^2}{\mathcal{F}(\tau) + \mathcal{M}(\tau)}, \quad (3.28)$$

where $\mathcal{M}(\tau) = \sum_c \mathcal{M}(\tau,c)$ is accordingly the model excess co-added over clusters. For CW stacking, taking $S_{\text{cw}}(\tau)$ as the relevant random variable yields

$$\chi_{\text{cw}}^2 \simeq \sum_{\tau} \frac{\left[\sum_{c=1}^{N_c} \frac{\mathcal{N}(\tau,c) - \mathcal{F}(\tau,c) - \mathcal{M}(\tau,c)}{\sqrt{\mathcal{F}(\tau,c)}}\right]^2}{\sum_{c=1}^{N_c} \left[1 + \frac{\mathcal{M}(\tau,c)}{\mathcal{F}(\tau,c)}\right]}. \quad (3.29)$$

In both methods, one may also sum over the two catalogs in order to fit both X-ray and radio signals simultaneously and estimate their joint significance.

Minimizing χ^2 is equivalent in the normal-error approximation to finding the maximum \mathcal{L}_{max} of the likelihood $\mathcal{L}(\chi^2) = \exp(-\chi^2/2)$. The significance of the excess within the model is estimated from the test statistic [33]

$$\text{TS} \equiv -2 \ln \frac{\mathcal{L}_{\text{max},-}}{\mathcal{L}_{\text{max},+}} = \chi_-^2 - \chi_+^2, \quad (3.30)$$

where a subscript ‘-’ (‘+’) refers to the best-fitted model without (with) the modelled excess. Then TS has an approximate chi-squared distribution χ_n^2 of order $n \equiv n_+ - n_-$, *i.e.* with the number of degrees of freedom added by the excess-source model [34]. Our single-parameter 1σ confidence intervals are defined through $\text{TS} = 1$ after projecting onto the given parameter.

For modelling, we nominally adopt a $\Delta\tau = 1/6$ resolution, to better capture the radial profile; results for other resolutions are given in §D. We use Monte-Carlo simulations to verify that although the data is not normally distributed, χ^2 in both Eqs. (3.28) and (3.29) indeed follows the expected χ^2 distribution (see §C), and so can be used to estimate the TS-based CLs, denoted σ_{TS} .

4. VIRIAL EXCESS AND ITS IMPLICATIONS

Our nominal stacking procedure yields the significance $S(\tau)$ profiles of the radially binned excess in Fig. 4, with the SW significance $S(\tau_x, \tau_y)$ of the 2D excess illustrated in Fig. 5. Fractional source overdensity $\delta(\tau)$ profiles are shown in Fig. 6, along with their effective modelling summarized in Table II and in more detail in Table III. Each panel in these figures shows results for both X-ray and radio catalogs, as well as a joint analysis of both catalogs. Additional results and models are provided in §D.

A. Stacking

The stacking results are only weakly sensitive to the details of the analysis, as shown by the various sensitivity tests and method variations in §D, as well as by the similar results obtained in Figs. 4 and 6 using the SW (left panels) vs. CW (right panels) co-addition methods. In Fig. 5 and in the models of Table II and §4B, we

focus on the more conventional and well-calibrated SW stacking; CW models are deferred to Table III.

As expected, the centers of the stacked clusters show a strong excess of both X-ray and radio sources associated with the ICM. This $\tau \lesssim 1.5$ excess reaches very high, $\delta \simeq 50$ ($\delta \simeq 20$) central overdensities in X-rays (radio), detected at extremely high, $S \simeq 100$ ($S \simeq 40$) CLs. These and all subsequent CLs include the aforementioned correction for Poisson-statistics.

We are more interested here in cluster peripheries, where a nearly identical, highly significant, $\delta \simeq 0.5$ overdensity is identified in both X-ray (4.4σ) and radio (4.0σ) sources. In both catalogs, this excess is highly localized, found in the same anticipated region (highlighted in Figs. 3-6), and peaked around the same $\tau \simeq 2.4$ normalized radius, identified previously as the VS in γ -ray [13] and radio [14] continuum stacking. Indeed, a joint-catalog analysis indicates a very high confidence, 5.9σ detection. Below, we discuss this signal, henceforth referred to as the VS excess, in detail.

In addition to the central and VS signals, both catalogs show evidence for a very peripheral, $5.5 \lesssim \tau \lesssim 7.5$ excess. This weak, $\delta \simeq 0.2$ overdensity presents in both X-rays and radio at a low, $S \simeq 2$ significance in our nominal resolution scans. However, the signal is very extended, and so presents with a more significant, $\sim 2.5\sigma$ detection at low resolution. Furthermore, as the X-ray and radio signals overlap, a joint-catalog analysis implies a more significant, $\sim 3\sigma$ overdensity. Interestingly, a sim-

ilar peripheral weak excess was previously identified independently, in continuum γ -ray, radio, and SZ analyses, suggesting non-spherical, elongated VS morphologies; see discussion in Ref. [13].

B. Modeling

Consider first the VS excess in X-ray sources. Fitting a planar (shell) model places the shock at $\tau_{\text{sh}} = 2.44^{+0.06}_{-0.19}$ ($2.50^{+0.00}_{-0.02}$), detected at a TS-significance of 3.8σ (3.3σ), as inferred from $\text{TS} \simeq 20.6$ with $n = 3$ degrees of freedom ($\text{TS} \simeq 14.2$ with $n = 2$). The width of the shock in the planar model is $\Delta\tau_{\text{sh}} = 0.03^{+0.04}_{-0.03}$; for a cluster of median sample parameters ($z \simeq 0.077$ and $\theta_{500} \simeq 0.15$), this corresponds to only ~ 20 kpc. Given our prior knowledge of the VS radius, the effective significance of the detection is higher. For instance, if one adopts as priors a shock radius $\tau_{\text{sh}} = 2.4$ (based on [13] and [14]) and a sub-resolution shock width, then the TS-confidence rises to 4.5σ (for $n = 1$ remaining free parameter).

Modeling the radio-source excess yields very similar results. Here, the planar (shell) model indicates a shock of similar radii $\tau_{\text{sh}} = 2.44^{+0.04}_{-0.05}$ ($2.54^{+0.06}_{-0.03}$), detected at a 3.8σ (3.3σ) CL. The shock width in the planar model, $\Delta\tau_{\text{sh}} = 0.12^{+0.05}_{-0.04}$, is larger than inferred from X-rays, corresponding to ~ 90 kpc for median (see Table I) cluster parameters. Here too, if one adopts as priors $\tau_{\text{sh}} = 2.4$ and a sub-resolution shock width, the detection TS-confidence rises to 4.5σ .

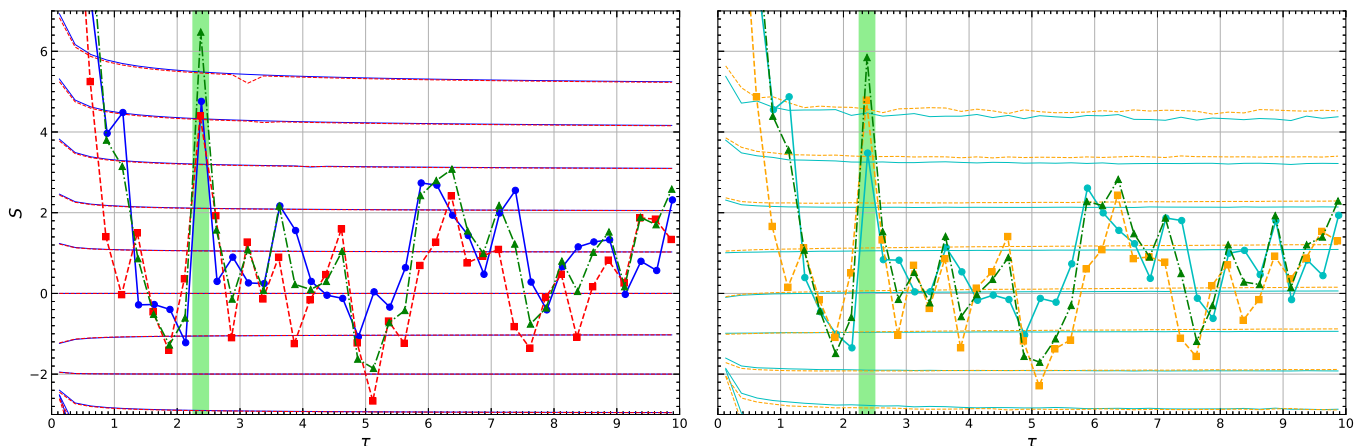


FIG. 4. Significance $S(\tau)$ profiles of the SW/CW (left/right panel) co-added excess of X-ray (blue/cyan disks with solid guides to the eye), radio (red/orange squares with dashed guides), and co-added X-ray+radio (green triangles with dot-dashed guides) sources around our nominal MCXC cluster sample. Corrected confidence levels (thin, approximately horizontal curves) for X-ray (solid curves) and radio (dashed) are based on either a Poisson approximation (for SW, where they are accurate) or control clusters (for CW). The anticipated VS region is highlighted as in Fig. 3.

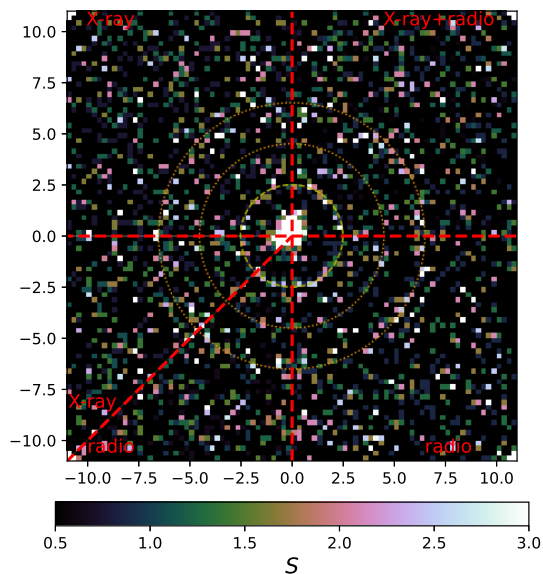


FIG. 5. Excess-source significance S in sky coordinates $\{\tau_x, \tau_y\}$ for SW-stacked and folded (see labels) X-ray (folded onto left quadrant and octant), radio (bottom quadrant and octant) and joint (upper right quadrant) catalogs. Dotted circles at $\tau = 2.5, 4.5,$ and 6.5 are guides to the eye. Stacked source images around individual clusters are rotated randomly around the center of the cluster before cluster co-addition.

The X-ray and radio excess signals closely overlap, so a joint-catalog analysis produces similar results, at a higher CL. Here, the planar (shell) model indicates a $\tau_{\text{sh}} = 2.41^{+0.02}_{-0.02}$ ($\tau_{\text{sh}} = 2.50^{+0.82}_{-0.77}$) shock, detected at 5.3σ (4.4σ). The corresponding (planar model) shock width $\Delta\tau_{\text{sh}} = 0.10^{+0.03}_{-0.02}$ translates to ~ 80 kpc for the median

($z \simeq 0.079$ and $\theta_{500} \simeq 0.14$) parameters of the joint cluster sample. Adopting as priors a $\tau_{\text{sh}} = 2.4$ shock radius and a sub-resolution shock width would raise the TS-confidence to 5.8σ .

TABLE II. Nominal VS modeling.

Model	Cat.	$n_{0,X}^*$	$n_{0,\nu}^*$	τ_{sh}	$\Delta\tau_{\text{sh}}$	TS	σ_{TS}
(1)	(2)	(3)	(4)	(5)	(6)	(7)	(8)
Shell	2RXS	$8.2^{+1.4}_{-3.4}$	—	$2.50^{+0.00}_{-0.04}$	—	14.2	3.3
Shell	NVSS	—	$8.1^{+2.4}_{-2.3}$	$2.54^{+0.06}_{-0.03}$	—	14.0	3.3
Shell	Joint	$7.3^{+2.3}_{-2.1}$	$6.8^{+2.2}_{-2.1}$	$2.50^{+0.03}_{-0.78}$	—	25.8	4.4
Planar	2RXS	$5.5^{+1.6}_{-1.5}$	—	$2.35^{+0.05}_{-0.02}$	$0.03^{+0.04}_{-0.03}$	20.6	3.8
Planar	NVSS	—	$6.5^{+2.1}_{-1.8}$	$2.44^{+0.04}_{-0.05}$	$0.12^{+0.05}_{-0.04}$	20.4	3.8
Planar	Joint	$5.8^{+1.7}_{-1.5}$	$5.9^{+1.9}_{-1.7}$	$2.41^{+0.02}_{-0.02}$	$0.10^{+0.03}_{-0.02}$	38.1	5.3

Nominal (SW; $\Delta\tau = 1/6$) best-fitted parameters; additional models are provided in Table III. Table columns: (1) Effective VS model (planar or shell); (2) Stacked catalog (2RXS, NVSS, or the two catalogs jointly); (3) and (4) Normalized, $n_0^* \equiv 10^3 n_0$ X-ray and radio source densities in Eqs. (3.24) or (3.26); (5) Dimensionless shock radius; (6) Dimensionless signal width; (7) TS value; (8) TS-based significance.

Curiously, we find similar source densities for the VS excess in the X-ray and radio catalogs. With the planar model, for instance, $n_0 \simeq 5 \times 10^{-3}$ (sources per θ_{500}^2) in X-rays and $n_0 \simeq 7 \times 10^{-3}$ in radio; the shell model yields n_0 values similar but slightly higher due to the 3D projection. The exact difference between X-ray and radio peak densities is not particularly meaningful, as n_0 is somewhat sensitive to details such as catalog parameters and cuts. Despite their similar properties, in §F we show that X-ray and radio excess signals are not dominated by the same individual objects.

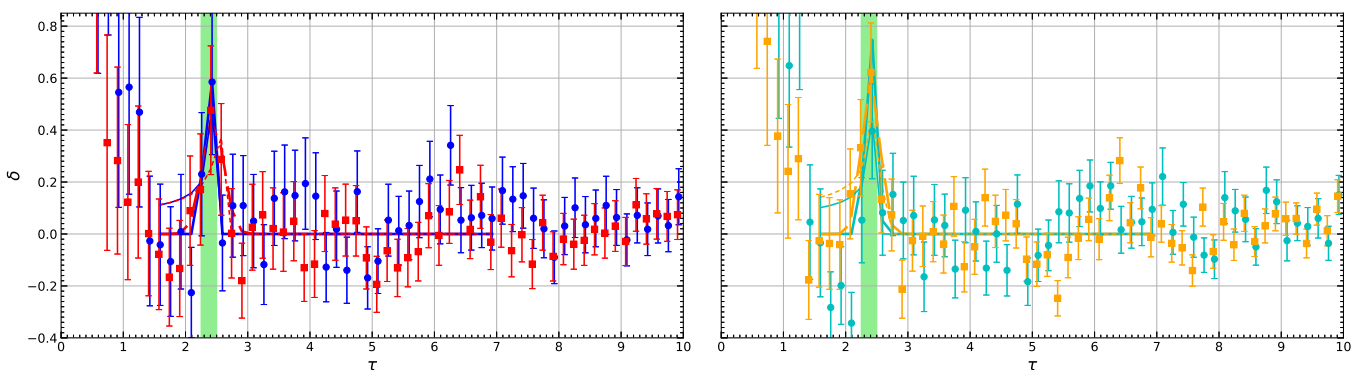


FIG. 6. Stacked fractional $\delta(\tau)$ overdensity (same notations as in Fig. 4), along with the best-fitted planar (thick curves, three-parameter) and shell (thin, two-parameter) models for the X-ray (solid curves) and radio (dashed sources).

As argued in §1, an excess of AGN in a narrow radial range at the far outskirts of clusters would be highly unnatural. Our above results establish systematically and quantitatively that both X-ray and radio sources emerge in a very narrow, $\Delta r/r \lesssim 20$ radial range, at least in a large fraction of clusters. This sharp excess is inconsistent with enhanced AGN triggering, given the weak environmental gradients found at these large, $\gtrsim 2$ Mpc radii, and the low ambient pressure even behind the VS. We conclude that the signals are unrelated to AGN; indeed, we find no significant localized signal when examining or stacking sources associated with identified AGN, as shown in §G. Moreover, the properties of the excess sources, discussed in §5, are inconsistent with AGN.

The robust spatial coincidence of the excess with the previously-determined VS location indicates that the excess is associated with the shock itself, and is most likely triggered by it. While the shock provides the strong spatial localization necessary to account for the sharpness of the excess, its downstream pressure is still far too weak to penetrate into the very center of a galaxy and trigger an AGN, so it is necessary to explore alternative models. Indeed, the constraints derived in §5 on the properties of the excess sources indicate that they constitute a different class of objects, explored in §6.

5. PROPERTIES OF VS EXCESS SOURCES

The $\delta \simeq 0.5$ fractional overdensity of both X-ray and radio catalog sources within the narrow VS range indicates that roughly $\sim 1/3$ of the sources therein are associated with the VS, while the remaining $\sim 2/3$ majority are field sources. The sources found in the VS regions, listed in §H, are mostly unidentified; note that these peripheral sources lie well outside the radii of known ICM radio sources, including halos, relics, and even mega-halos [35], and cannot be attributed to the smooth distribution of cluster sources or to AGN (§G). While we cannot attribute individual sources to the VS, the most likely properties of those VS-induced sources can be deduced from a differential statistical analysis that compares the properties of sources in the VS region to their field counterparts.

Consider some source property \mathbb{P} of interest, such as flux, spectral index, or size. Figures 7–14 compare, for various such properties, the distribution of \mathbb{P} among sources in the VS region ($2.25 < \tau < 2.5$) to \mathbb{P} among sources in the ICM region ($1.0 < \tau < 1.5$) and in the field. Here, we adopt a normalized, $7 < \tau < 35$ radial field range, instead of the fixed angular scale invoked earlier for field removal, in order to obtain a better behaved VS-to-field source-number ratio. In addition to the nominal analysis, we also consider different field regions ($10 < \tau < 30$) and cuts that do not exclude the FB and Loop-I regions, in order to improve the statistics. For additional tests and source properties, see §E.

When relevant, we show analogous X-ray (left panels)

and radio (right panels) \mathbb{P} properties on the same figure. Each figure presents both differential $N(\mathbb{P}) \equiv dN/d\mathbb{P}$ (top panels) and cumulative $N(< \mathbb{P})$ (bottom panels) distributions in the VS region (solid and dot-dashed green), compared to equivalent field (thick dashed and thin dotted red) and ICM (dot-dashed and double dot-dashed magenta) distributions scaled to the same Ω . Bottom panels highlight also the cumulative, $N_{\text{VS}}(< \mathbb{P}) - N_{\text{F}}(< \mathbb{P})$ distribution (solid blue) and the $S(\mathbb{P}) = [N_{\text{VS}} - \mu(N_{\text{F}})]/\sigma(N_{\text{F}})$ local significance (dashed green) of the VS excess, with respect to the field distribution N_{F} inferred from > 200 random field samples.

Figure 7 shows the logarithmic, $\mathbb{P} = \log_{10} F$ energy flux distribution. In X-rays, the VS excess arises mostly in the $2 \times 10^{-13} \text{ erg s}^{-1} \text{ cm}^{-2} \lesssim F_X \lesssim 2 \times 10^{-12} \text{ erg s}^{-1} \text{ cm}^{-2}$ flux range, dominating the cumulative distribution at local $\gtrsim 3\sigma$ significance levels, and appears unaffected by our higher F_X upper limit. In radio, the excess arises mostly in the $10^2 \text{ mJy} \lesssim F_\nu \lesssim 10^3 \text{ mJy}$ range, with a local $\gtrsim 2\sigma$ significance increasing towards lower F_ν , suggesting additional excess sources below our lower F_ν cutoff. The local excess of bright sources with ~ 5 Jy flux, seen in the figure, can probably be disregarded, as it is associated with only two sources and is not robust against changes in analysis details.

The cataloged sources do not have readily available associated redshifts. Assigning sources to the redshift of the nearby MCXC cluster, as seen in projection, produces an intrinsic, albeit noisy, estimate of the typical luminosity of excess VS sources. Figure 8 thus shows that the excess is associated with $10^{42} \text{ erg s}^{-1} \lesssim L_X \lesssim 10^{43} \text{ erg s}^{-1}$ 2RXS sources and with $10^{40} \text{ erg s}^{-1} \lesssim \nu L_\nu \lesssim 10^{41} \text{ erg s}^{-1}$ NVSS sources. (The luminosity of excess GMRT sources is a factor ~ 2 lower than in NVSS; see Fig. E.6.) Again, local excess signals at lower or higher luminosities cannot be substantiated, as they are associated with few sources and are not robust against changes to the analysis details.

Consider the (unlikely) possibility that the VS excess signals in X-rays and in radio arise from the same power-law spectrum, extending over more than eight orders of magnitude in photon energy (although the implied synchrotron origin of the X-rays is ruled out in §6). For the relevant VLA and *ROSAT* channels, the associated photon spectral index would then be

$$\alpha \equiv -\frac{d \ln L}{d \ln \nu} \simeq 0.81 \left(\frac{100 \nu L_\nu}{L_X} \right)^{0.067}, \quad (5.1)$$

providing a robust reference value for a spectral analysis.

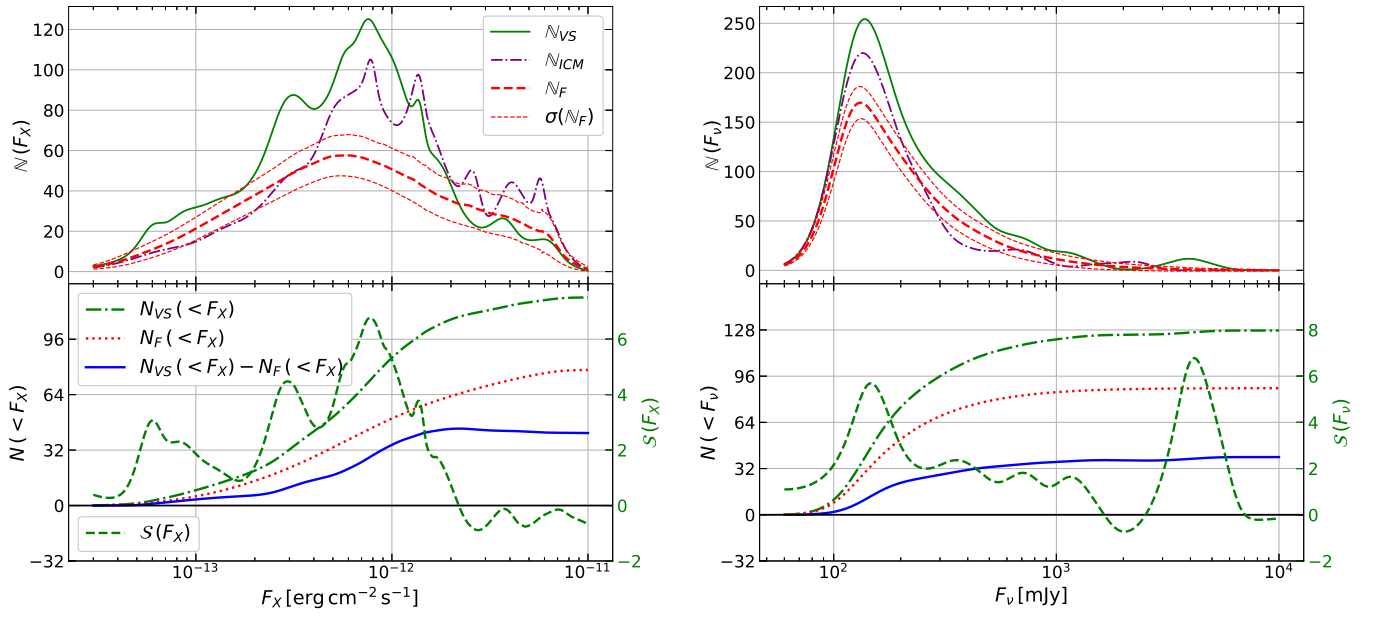


FIG. 7. Differential $N(\mathbb{P})$ (top panels) and cumulative $N(< \mathbb{P})$ (bottom panels with left axes) distributions of logarithmic, $\mathbb{P} = \log_{10} F$ energy flux in X-rays (left panels) and radio (right panels). Differential distributions are shown for the VS region (solid green) and comparable ICM (dot-dashed magenta) and field (red; thick dashed for mean value and thin dotted for 1σ dispersion) estimates; see text. Bottom panels show, in addition to the cumulative distributions in the VS region (dot-dashed green), field estimate (dotted red), and their difference (solid blue), also the local significance of the VS excess (dashed green with right axes). In radio, we add a $\sigma_{\text{smooth}}^2 \equiv (0.2 F_\nu)^2$ smoothing variance to the F_ν uncertainty, for visibility.

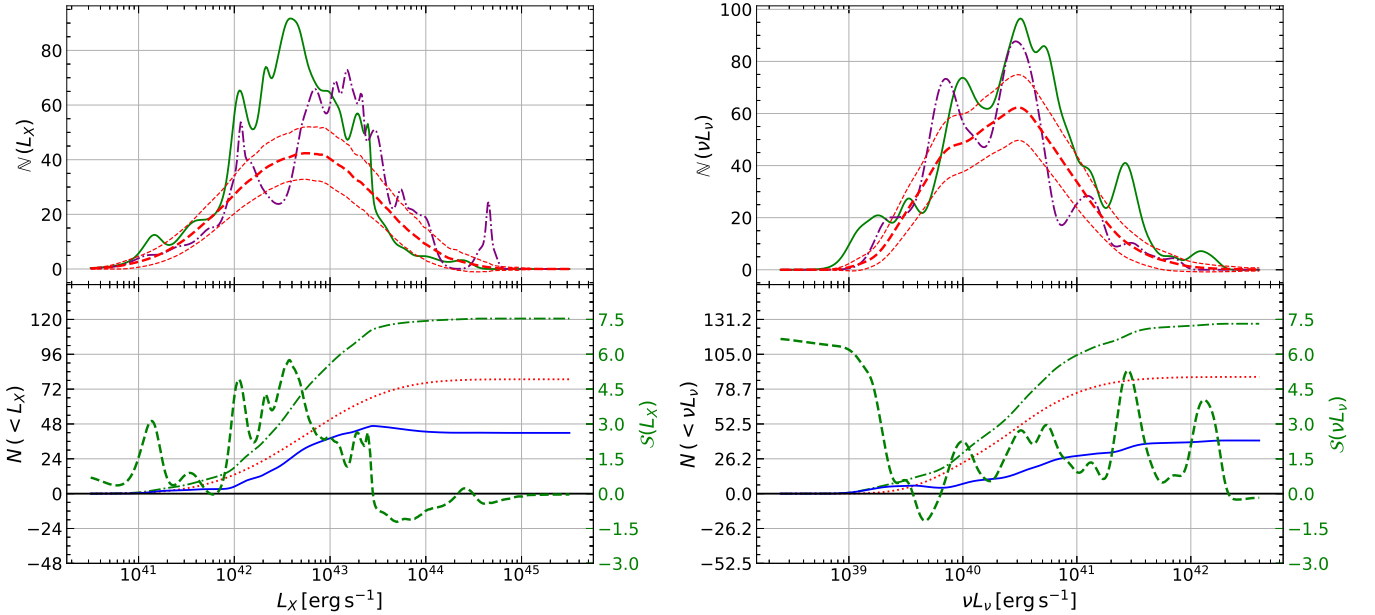


FIG. 8. Distribution of luminosity, $\mathbb{P} = \log_{10} L_X$ in X-rays (left) and $\mathbb{P} = \log_{10} \nu L_\nu$ with added $\sigma_{\text{smooth}}^2(L_\nu) \equiv (0.2 L_\nu)^2$ variance (for visibility) in radio (right); notations are as in Fig. 7.

The spectral index $\alpha_{150\text{ MHz}}^{1.4\text{ GHz}}$ is estimated by matching sources in the GMRT and NVSS catalogs through a projected proximity, $\theta < \theta_{\text{max}} = 30''$ angular separation criterion. Most ($\sim 90\%$) GMRT sources then show an NVSS counterpart, with only a small, $\pi\theta_{\text{max}}^2 N_{\text{NVSS}} N_{\text{GMRT}} / (4\pi f_{\Omega} N_{\text{pairs}}) \sim 1\%$ fraction of the resulting $N_{\text{pairs}} \simeq 5.6 \times 10^5$ pairs being false, chance associations. Here, $N_{\text{NVSS}} \simeq 1.6 \times 10^6$ and $N_{\text{GMRT}} \simeq 5.8 \times 10^5$ are respectively the numbers of NVSS and GMRT sources in the relevant, $f_{\Omega} = 82\%$ fraction of the sky. Defining $\mathbb{P} = \alpha_{150\text{ MHz}}^{1.4\text{ GHz}}$ for each pair, the radio VS excess may be inferred from Fig. 9 to arise mostly from $0.5 \lesssim \alpha_{150\text{ MHz}}^{1.4\text{ GHz}} \lesssim 0.8$ sources. The considerable $\alpha_{150\text{ MHz}}^{1.4\text{ GHz}} < 0.6$ excess suggests that this hard synchrotron power-law spectrum does not extend up to X-ray energies.

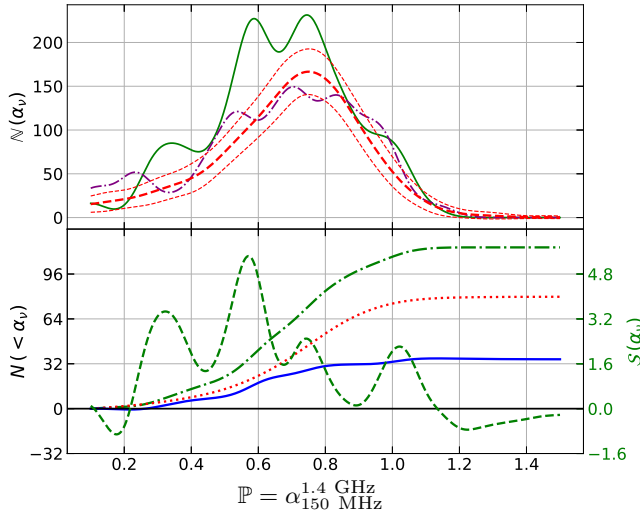


FIG. 9. Distribution of $\mathbb{P} = \alpha_{150\text{ MHz}}^{1.4\text{ GHz}}$ radio spectral indices among GMRT-NVSS catalog pairs; notations as in Fig. 7.

This estimate is broadly consistent but somewhat harder than in Eq. (5.1), and in the absence of NVSS-2RXS pairs (see §F), we cannot support such α_{ν} values persisting out to X-rays. Moreover, while we cannot localize any excess in the X-ray spectral index Γ_X obtained from power-law fits, both Mekal and black-body fits suggest $k_B T \gtrsim 1\text{ keV}$ excess-source temperatures, as shown in Figs. 10 and A.2, where k_B is the Boltzmann constant. The combined implications of hard power-law spectra in radio and thermal spectra in X-rays are discussed in §6.

The VS excess is associated in radio with sources of elevated linear polarization, in the 1–10% range, as indicated by Fig. 11. Here we use the bias-corrected, linearly polarized flux density and its associated position angle, available for most sources in the NVSS catalog; see [24] for details. Again assigning sources to a nearby projected MCXC cluster, we may estimate the typical angle ϕ between the source polarization vector and the radius, *i.e.* the line connecting it to the center of cluster. As Fig. 12 shows, the polarization is preferentially radial ($\phi \simeq 0$), corresponding to magnetic fields aligned perpendicular

to the cluster radius.

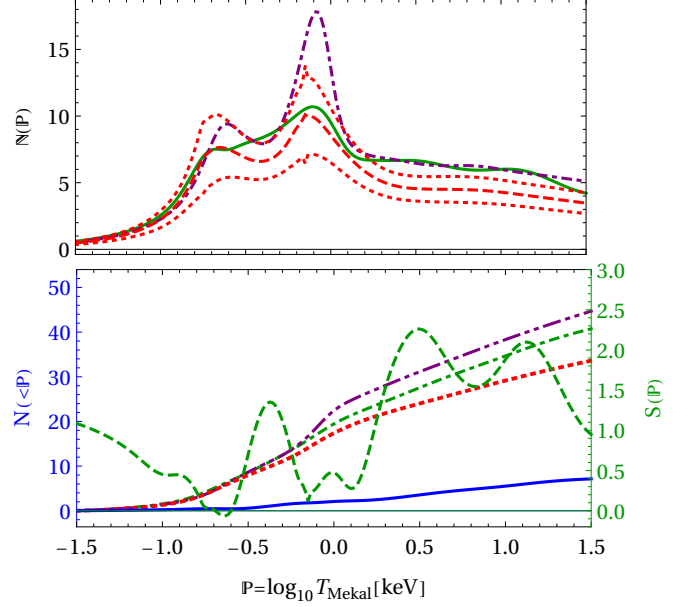


FIG. 10. Distribution of the $\mathbb{P} = \log_{10} k_B T$ Mekal-fitted temperature; notations as in Fig. 7. Here we show also the cumulative ICM-source distribution (double-dot magenta).

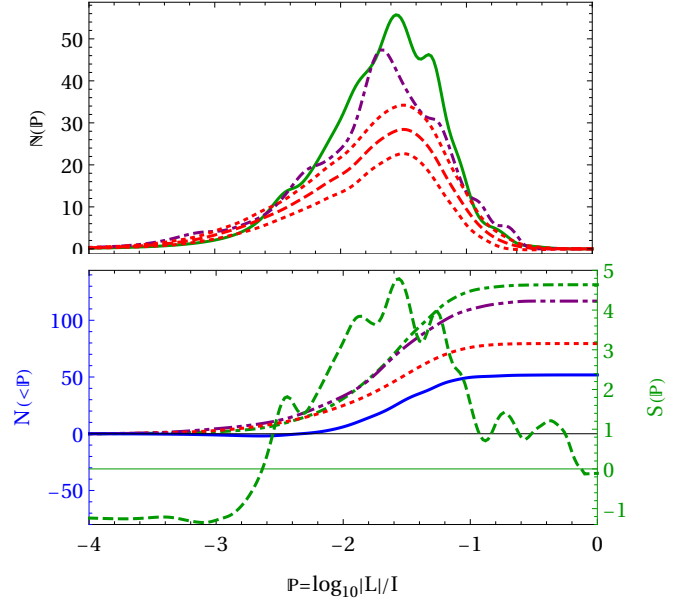


FIG. 11. Distribution of the $\mathbb{P} = \log_{10} |L|/I$ linearly-polarized radio fraction; notations as in Fig. 10.

This effect is quite robust, strengthening at high Galactic latitudes or at high declinations [where the typical Galactic Faraday rotation at NVSS frequencies drops below $\sim 30^\circ$; see, *e.g.*, 36], as illustrated by the figure. Such a polarization supports the association of the sources not only with the cluster, but also specifically with its VS, suggesting that the emission arises from a gaseous medium shocked by the VS, resulting in enhanced tan-

gential magnetic fields. While the measured polarizations carry substantial uncertainties, the elevated polarized flux and the correlation between polarization vectors and radii among VS (but not field) sources suggest that the polarization effect is real.

Assigning again sources with nearby projected MCXC clusters, we may estimate the typical sizes of sources in the VS region. Figure 13 thus suggests that the X-ray excess is dominated by sources of $30 \text{ kpc} \lesssim R \lesssim 100 \text{ kpc}$ radii, whereas the radio excess arises from sources with semi-major axes in the range $10 \text{ kpc} \lesssim a \lesssim 100 \text{ kpc}$. An analogous examination of the semi-minor axes b of the radio sources suggests that the VS excess arises from elongated sources, of $6 \text{ kpc} \lesssim b \lesssim 30 \text{ kpc}$. Similarly estimating the dimensionless (normalized to R_{500}) scales yields $0.05 \lesssim \tau_R \lesssim 0.15$, $0.02 \lesssim \tau_a \lesssim 0.2$, and $0.01 \lesssim \tau_b \lesssim 0.15$, associated respectively with the X-ray radius and the radio semi-major and semi-minor axes (see §E). These scales are broadly consistent with the width $\Delta\tau_{\text{sh}}$ of the stacked VS signal, as derived in §4.

The distribution of the angle φ between the semi-major axis of a radio source and the line connecting it to the center of the cluster, presented in Fig. 14, appears bimodal. A significant excess is found for sources elongated both around $\varphi \simeq 30^\circ$, and perpendicular ($\varphi \simeq 90^\circ$) to the cluster radius; again, any well established φ excess would support the association of the virial excess with the cluster, and specifically with the VS. The second, $\varphi \simeq 90^\circ$ excess (see also Fig. E.4) is associated with the more ex-

tended sources, which appear to be stretched along the VS; however, we cannot substantiate this excess, as it vanishes at high declinations as shown in the figure.

We examine the dependence of the VS excess upon cluster mass by crudely splitting the cluster sample into three M_{500} bins, as shown in Fig. 15. The bins are adjusted to include a roughly fixed, ~ 150 number of clusters per bin, to provide comparable statistics in each bin; this is achieved only approximately, as we adopt the same mass bins for both X-ray and radio analyses. The figure suggests that the mass dependence of the VS excess is weak, unlike the strong mass dependence expected [37–39], simulated [10, 40], and indicated observationally [14] for smooth accretion.

It is interesting to examine the properties of the ICM-region, $1 < \tau < 1.5$ excess, featuring sources clearly associated with the cluster, but residing away from its center and probably not directly related to its VS. These sources are somewhat brighter than the VS sources in X-rays, extending out to $\sim 10^{44} \text{ erg s}^{-1}$, but not in radio, where a deficit is seen above $\sim 10^{40.5} \text{ erg s}^{-1}$. The source spectra indicate $\sim \text{keV}$ temperatures in X-rays; the radio spectra cannot be determined, as their distribution does not significantly differ from the field. The sources are comparable to the VS sources in terms of size, $30 \text{ kpc} \lesssim R \lesssim 70 \text{ kpc}$ in X-rays, and $5 \text{ kpc} \lesssim a \lesssim 50 \text{ kpc}$ in radio. Finally, while these sources show a linear polarization fraction somewhat smaller than in the field, there is a low-significance indication of preferred polarization in the radial ($\varphi \simeq 90^\circ$), and not the tangential, direction.

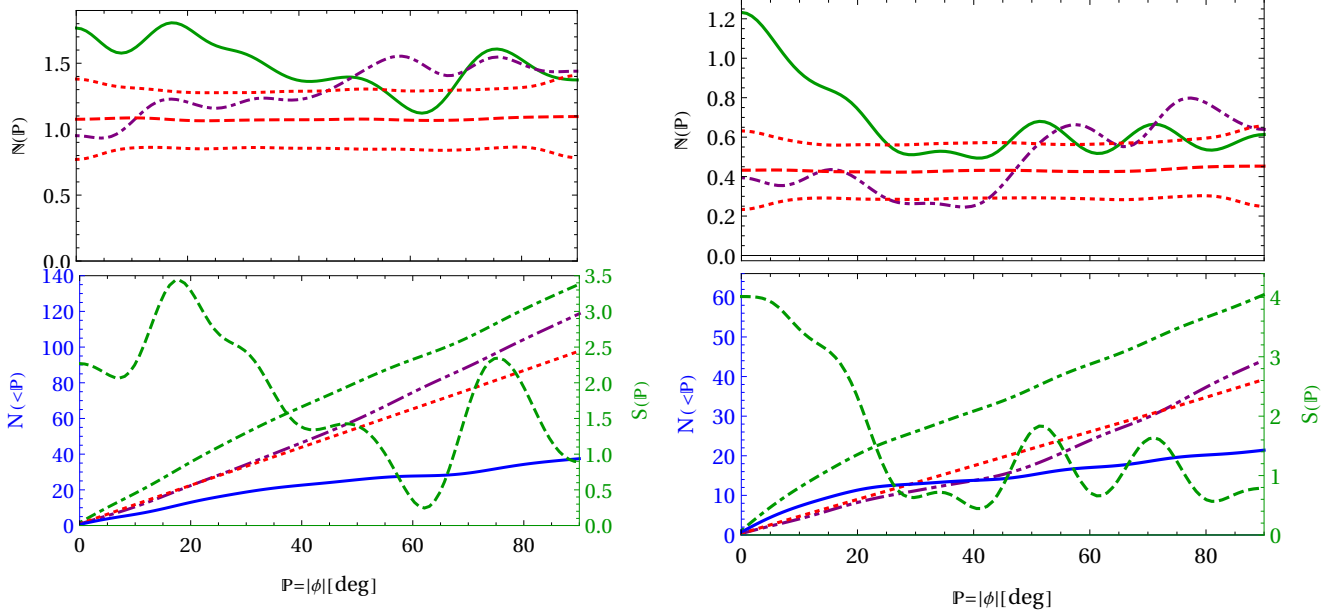


FIG. 12. Distribution of the $\mathbb{P} = |\phi|$ angle between polarization vector and cluster radius for all (left) and $\text{Dec} > 20^\circ$ (right) sources; notations and sources as in Fig. 11. A $\sigma_{\text{smooth}}^2(\varphi) = (5^\circ)^2$ variance is added for visibility.

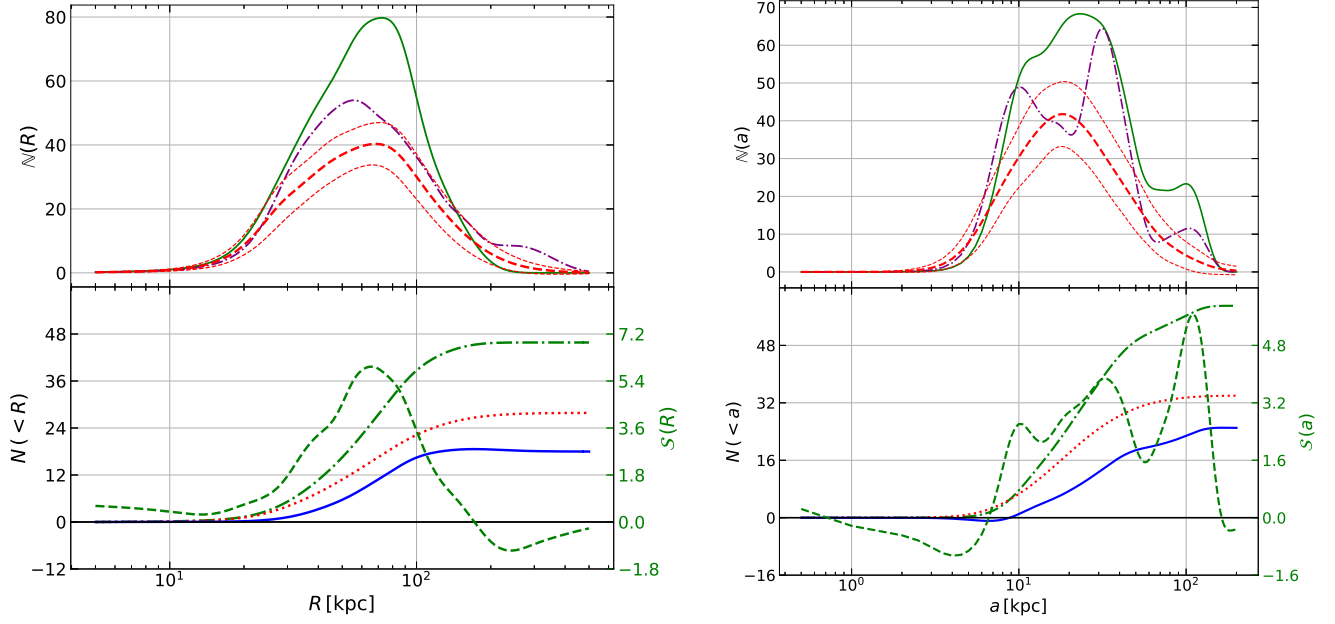


FIG. 13. Distribution of source size: radius $\mathbb{P} = R$ in X-rays (left) and semi-major axis $\mathbb{P} = a$ with added $\sigma_{\text{smooth}}^2(a) \equiv (0.2a)^2$ variance in radio (right) for visibility; notations are the same as in Fig. 7. Normalized (to θ_{500}) and semi-minor axes are shown in Figs. E.2 and E.3.

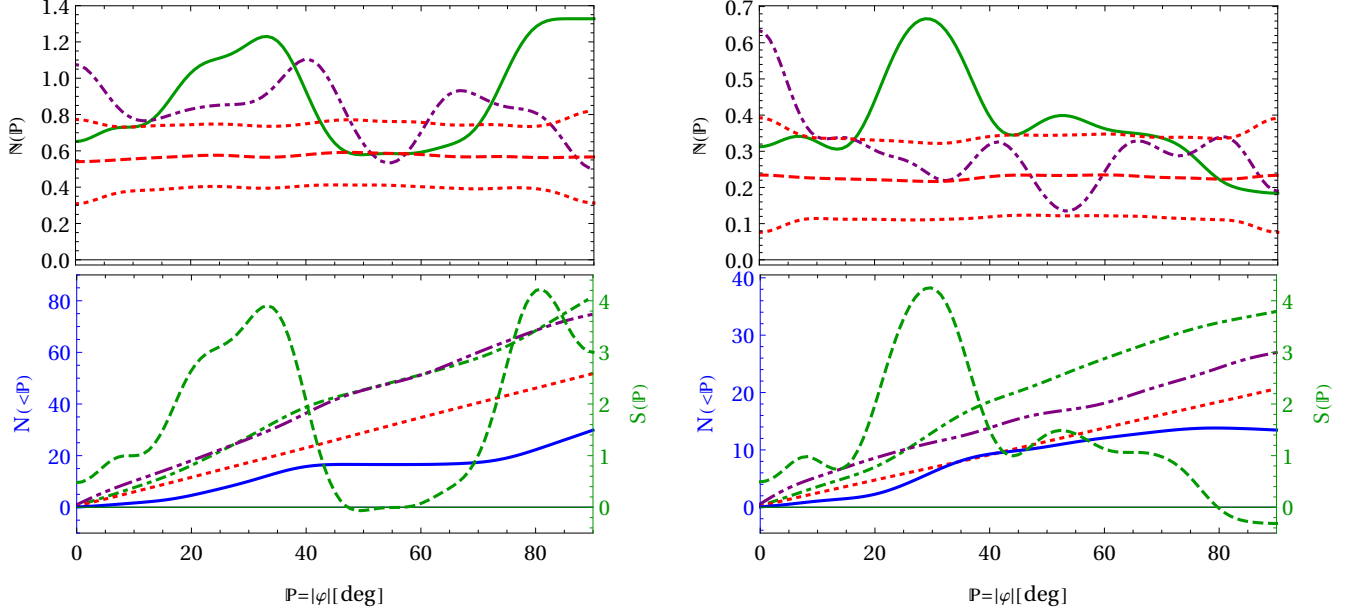


FIG. 14. Distribution of the $\mathbb{P} = |\varphi|$ angle between source elongation and cluster radius for all (left) and $\text{Dec} > 20^\circ$ (right) sources; notations and sources as in Fig. 11. A $\sigma_{\text{smooth}}^2(\varphi) = (5^\circ)^2$ variance is added for visibility.

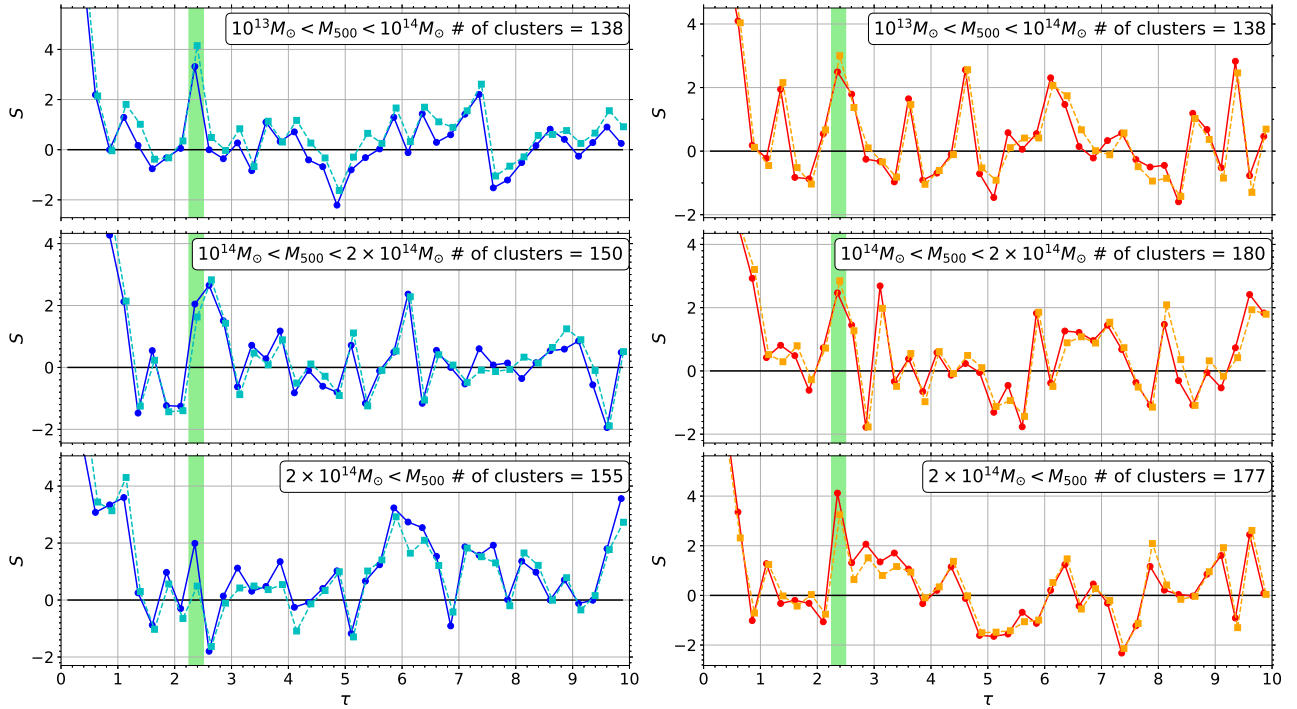


FIG. 15. Significance $S(\tau)$ profile of excess X-ray (left panel) and radio (right) sources in different M_{500} bins (see legend); other notations are the same as in Fig. 4.

6. ORIGIN OF THE VS SOURCES

The above results show a highly significant excess of X-ray and radio catalog sources narrowly peaked near the same, $\tau \simeq 2.4$ normalized radius where previously stacked γ -ray [13] and radio [14] continuum signals were attributed to VS-induced emission. This spatial coincidence indicates that the excess sources are directly associated with the VS of their host cluster, especially considering the very narrow, $\Delta\tau \simeq 0.1$ width of their stacked excess. Indeed, it is difficult to envision how a well-localized spike in source density at this particular radius could arise without involving the VS. The conclusion is further supported by anecdotal evidence, such as the well-defined angles of radio source polarization and possibly also elongation with respect to the host cluster. Here, we consider the physical mechanism by which the VS may induce the excess sources, as implied by the stacked signal (§4) and statistical source properties (§5).

The comparable and narrow widths of the X-ray and radio signals suggests that the sources radiate, or, more likely, brighten significantly, only during VS crossing or soon thereafter. For a body of length $l = 100l_{100}$ kpc, such brightening would span a normalized $\Delta\tau \simeq 0.1l_{100}$ radial extent during the $t \simeq l/v_s \simeq 0.1l_{100}T_1^{-1/2}$ Gyr passage of the body into the $k_B T_d \simeq T_1$ keV ICM, approximating its infall through the VS as fixed at the $v_s \simeq (16k_B T/3\bar{m})^{1/2}$ shock velocity. This conclusion is supported by the $0.02 \lesssim \{\tau_R, \tau_a\} \lesssim 0.2$ extent of the in-

dividual sources comprising the excess, being comparable and not much smaller than the signal width.

The $\Delta P \lesssim 0.02 \text{ eV cm}^{-3}$ pressure change induced by the VS [e.g., 19, 20, 41, 42] is much too weak to penetrate down to the vicinity of compact bodies, certainly those found in the centers of galaxies. As anticipated in §1, our results thus challenge previous claims that a well-localized excess of X-ray sources near the virial radius could be attributed to AGN. Indeed, sources already associated with identified AGN show no significant localized excess; see §G. Instead, sources triggered by the VS are likely to be extended and gaseous. Indeed, this conclusion is directly corroborated by the inferred, 10–100 kpc extent of the excess sources, as well as by the polarization angle of the radio emission.

Specifically, the extent, spectrum, and polarization of the radio sources identify them as synchrotron emission from an extended distribution of CREs which have not fully cooled, gyrating in the predominantly tangential magnetic fields B amplified by the VS. For the $\gamma_\nu \simeq 2 \times 10^4 B_1^{-1/2}$ Lorentz factor of the 1.4 GHz radio-emitting CREs, the cooling length

$$l_{\text{cool}} \simeq v_s t_{\text{cool}} \simeq v_s \frac{6\pi m_e c f_B}{\sigma_T \gamma_\nu B^2} \simeq 110 \frac{\sqrt{B_1 T_1}}{1 + 0.1 B_1^2} \text{ kpc} \quad (6.1)$$

is comparable to the width of the signal at the $B_1 \equiv B/1 \mu\text{G} \simeq 1.9$ maximum of the cooling time $t_{\text{cool}}(B)$. Here, c is the speed of light, σ_T is the Thomson cross-section, m_e is the electron mass, and we defined the frac-

tions $f_e \equiv 1 - f_B$ and

$$f_B \equiv \frac{B^2/8\pi}{u_{cmb} + B^2/8\pi} \simeq \frac{0.1B_1^2}{1 + 0.1B_1^2} \quad (6.2)$$

of IC and synchrotron CRE emission, u_{cmb} being the CMB energy density.

For the \sim few $0.1\mu\text{G}$ fields anticipated over > 10 kpc scales, $l_{\text{cool}} \propto \nu^{-1/2}$ is shorter than our nominal $\Delta\tau$ resolution by a factor of a few at 1.4 GHz, but not at low frequencies. Interestingly, some possible 74 MHz broadening is found at low-significance by comparing the stacked NVSS, GMRT, and VLSSr profiles (see Fig. E.5).

In contrast to radio, the $\epsilon = \epsilon_1$ keV X-ray sources are unlikely to arise from non-thermal, neither IC nor synchrotron, emission. Indeed, IC emission over the relevant scales, dominated by $\gamma_e \simeq 10^3 \epsilon_1^{1/2}$ CREs scattering CMB photons, would extend over a far too long, $l_{\text{cool}} \simeq 2(T_1/\epsilon_1)^{1/2}$ Mpc cooling length, greatly exceeding the width of the signal; IC emission is also too faint to explain the sources, as shown below. The opposite problem of $l_{\text{cool}} \lesssim 9(T_1 B_1/\epsilon_1)^{1/2}$ pc cooling and $l_{\text{acc}} < cl_{\text{cool}}/v_s$ acceleration lengths much too short to explain the signal would arise if X-rays were synchrotron emission, also requiring a radio spectrum similar to Eq. (5.1), which is softer than inferred in §5, as well as an ongoing acceleration of excessively energetic, $\gamma \gtrsim 10^{8.5}(\epsilon_1/B_1)^{1/2}$ CREs. In either case, if CREs were responsible for the X-ray sources, we would expect to find at least a few 2RXS–NVSS pairs, absent in the present data.

Therefore, the X-ray excess is likely dominated by thermal emission from hot plasma. Indeed, the X-ray spectral fits are marginally more consistent with excess sources having high, $k_B T \gtrsim 1$ keV temperatures, than with sources of power-law spectra (see Figs. 10, A.1, and A.2). In addition, the evidence suggests (albeit at low confidence) that the radio signal has a radial extent ~ 2.5 times wider than in X-rays (see Table II) and that the radio a and b distributions extend to scales somewhat larger than the X-ray radius R (see Figs. 13, E.2, and E.3), consistent with a thermal X-ray component being more compact than its relativistic, radio counterpart.

X-ray emission from the hot plasma halo around a galaxy of mass M_{500} is thought to follow the same $L_{0.5 \text{ keV}}^{2.0 \text{ keV}} \simeq 10^{43} (M_{500}/10^{14} M_\odot)^{1.85}$ erg s $^{-1}$ scaling that extends up to galaxy-cluster scales [43, for a mean $C_{\text{bolo}} \simeq 1.1$ bolometric correction factor]. Such a halo around an infalling galaxy would substantially brighten if a fair fraction f_s of its mass is shocked, with f_s being plausibly large if the density profile is shallow (*e.g.*, $n \propto r^{-0.9}$ in Ref. [44]). For instance, the $[0.1, 2.4]$ keV luminosity $L_X \simeq 2L_{0.5 \text{ keV}}^{2.0 \text{ keV}}$ of $k_B T = 0.1$ keV plasma, compressed (factor ~ 10 brightening) and heated (factor ~ 2 brightening for $Z = 0.2$ metallicity) by a (typical: see below) Mach $\Upsilon \simeq 3.3$ shock, could account for at least the fainter of the $L_X \simeq 10^{42-43}$ erg s $^{-1}$ sources. The shocked halos of the more massive galaxies or galaxy aggregates could account for sources of higher luminosities and larger, $R \simeq 100$ kpc radii. Note that a shock is

driven also into the ICM, but is weak: $\Upsilon \simeq 3/\sqrt{5} \simeq 1.3$.

Infalling galactic halos processed by the VS could also explain the excess radio sources, through the acceleration or reacceleration of CREs and the magnetization of the plasma. When CRE scattering is sufficiently isotropic [45], diffusive shock acceleration [46–49] injects a CRE power-law spectrum of index $p \equiv -d \ln N/d \ln E \simeq 2(\Upsilon^2 + 1)/(\Upsilon^2 - 1)$. The $\alpha_{150 \text{ MHz}}^{1.4 \text{ GHz}} \simeq 0.55\text{--}0.8$ radio indices can thus be attributed to non-cooled CREs accelerated by $\Upsilon \simeq [1 + 2/(\alpha - 1/2)]^{1/2} \simeq 2.8\text{--}6.4$ shocks, which compress the gas and the tangential magnetic fields by a factor $1 + 3/(2\alpha) \simeq 2.9\text{--}3.7$, thus accounting for the radial polarization. Such shocks require plausible $16(5\Upsilon^2 - 1)^{-1} k_B T_d/(1 + 3\Upsilon^{-2}) \simeq (0.1\text{--}0.3)T_1$ keV pre-shock galactic-halo temperatures. Considering the main, $\alpha \simeq 0.55$ excess in Fig. 9 and accounting for partial CRE cooling renders the high, $\Upsilon \simeq 6$ regime more likely.

Such a shock, heating a fraction f_s of the gas mass M_g and depositing a fraction ξ_e of the resulting thermal energy in CREs, leads to a synchrotron luminosity

$$\begin{aligned} \nu L_\nu &\simeq \frac{2\alpha - 1}{2} \gamma_\nu^{-(2\alpha-1)} \xi_e f_B \frac{v_s}{\Delta r(\nu)} \frac{f_s M_g}{m_p} k_B T \quad (6.3) \\ &\simeq 10^{40} \xi_1 f_B \left(\frac{f_s M_g}{10^{11} M_\odot} \right) \frac{T_1^{3/2} B_1^{0.05}}{\Delta r_{100}} \text{ erg s}^{-1}, \end{aligned}$$

where we defined $\xi_1 \equiv \xi_e/1\% \simeq 1$ based on detected continuum VS signals [13, 14, 17, 18, 20], and $\Delta r_{100} \equiv \Delta r/100$ kpc $\simeq 1$ based on our NVSS stacking. Equation (6.3) can explain at least the fainter of the $\nu L_\nu \simeq 10^{40-41}$ erg s $^{-1}$ sources, even without accounting for a compressed or re-accelerated pre-existing CRE population. As mentioned above, the counterpart IC signal (replacing $f_B \rightarrow f_e$ in Eq. 6.3) is much too faint to explain L_X for plausible, $B \gtrsim 0.1 \mu\text{G}$ fields.

An interesting possibility is that the excess sources, or a subset of these sources, are associated with remnant lobes produced by galactic outflows from previous AGN or star formation bursts. Such lobes could provide seed CREs and magnetic fields, more easily explaining the excess radio sources even at their high-luminosity end. For example, a VS-induced, factor ~ 10 brightening of faint lobes could account for the entire radio excess, if they comprise $\sim 10\%$ of the rapidly declining (without the F_ν^* cut) $\mathbb{N}(L_\nu)$ distribution of field sources. Remnant galactic outflows could better explain why in the radio, the radial width of the stacked excess and the high end of the source-size distribution are somewhat larger than in X-rays, and may possibly account for the elongation angle φ distribution in Fig. 14 if the lobes are, *e.g.*, longer than l_{cool} or are stronger along a large-scale filament feeding the cluster. While the X-ray sources should still have a thermal origin, they could be strengthened if such outflows enrich their host halos.

7. SUMMARY AND DISCUSSION

Following reports of excess X-ray sources in galaxy-cluster peripheries, we stack X-ray (2RXS) and radio (NVSS, GMRT, VLSSr) catalog sources around MCXC galaxy clusters. We impose cuts on the MCXC to match source-catalog limitations (Table I), and an upper (lower specific) flux cutoff on the X-ray (radio) catalog, to avoid the dominant bright (faint) sources in the foreground (background); see Fig. 2. Our results are not, however, sensitive to any of our cuts or analysis details (see §D).

The radially binned and stacked projected source-density profiles are very similar to each other in X-rays and in radio (see Fig. 6, the fit results in Table II, and their counterparts in §D), presenting a pronounced peak near the same, $\tau \simeq 2.4$ normalized radius where source-masked γ -ray [13] and radio [14] continuum signals were previously detected and attributed to emission from the VS. Both X-ray and radio catalog signals are highly localized ($\Delta\tau \lesssim 0.1$), indicating that the excess sources are directly driven by the VS.

These excess X-ray ($\sim 4\sigma$ CL for 443 clusters), radio ($\sim 4\sigma$ for 485 clusters), and joint ($> 5\sigma$) source signals are significant enough (even without priors; see §4 and §D) to see directly in the stacked images even without full radial binning (Figs. 5 and D.7). The signals present robustly, independently, and with similar parameters in the four (2RXS, NVSS, GMRT, and VLSSr) catalogs, and are not sensitive to variations in our analysis methods and parameters (see §D). The signals and their CLs are verified using control cluster samples, showing that the stacked excess closely follows the expected Poisson statistics (Fig. 3 and §C) away from the real clusters.

The properties of the excess VS sources can be deduced only statistically and separately in each catalog, because the individual sources comprising the excess cannot be isolated from the \sim twice as large number of coincident field sources, and we cannot demonstrate a VS excess of X-ray–radio source pairs (see §F) with present statistics. We thus characterize the excess distributions of the flux (Fig. 7), luminosity (Fig. 8), and size (Fig. 13) of the sources, the temperature (Fig. 10) of the X-ray sources, and the spectral index (Fig. 9) and elongation angle (Fig. 14) of the radio sources, as well as their linear polarization fraction (Fig. 11) and angle (Fig. 12). Additional source properties are provided in §E.

The inferred properties of the excess X-ray and radio sources support their association with the VS, and constrain the physical mechanism responsible for their emergence (see §6). In particular, the radial, $\phi \simeq 0$ polarization of the radio sources, and their elongation angle distribution with its tentative tangential, $\varphi \simeq 90^\circ$ component, relate these sources to the VS orientation. The hard, $0.55 \lesssim \alpha_{150}^{1.4 \text{ GHz}} \lesssim 0.8$, partially polarized radio signal is identified as synchrotron emission from CREs energized by the VS, gyrating in predominately tangential magnetic fields amplified by the VS, whereas the X-ray emission is most probably thermal, arising from

an extended plasma distribution, compressed and heated to $k_B T \gtrsim 1$ keV temperatures by the VS. The excess sources are thus identified as heated gas clumps accreted through the VS, probably the hot halos of galaxies or galaxy aggregates, possibly enriched by dormant lobes from galactic outflows.

The narrowness of the excess-source signals and their coincidence with each other and with the VS also corroborate previous claimed detections of VS signals based on continuum emission [13, 14, 17–20], which were more complicated due to smaller numbers of relevant clusters, as well as challenges associated for example with data reduction, point-source removal, and interferometric sidelobes. A comparison with these studies indicates that in all cases, planar models fit the stacked $\tau \sim 2.4$ signals better than their projected-shell counterparts, and that a secondary weaker, broader, and farther, $5 \lesssim \tau \lesssim 7$ signal emerges (*cf.* Ref. [13], [14], and the present Figs. 4–6). Both effects indicate that a spherical, isolated model of the VS is oversimplified. The secondary signal would imply, if established at high confidence, that projected VS are elongated, with a mean ~ 2.5 aspect ratio, as indicated in Coma [17, 18], while the better fit of the planar model may also reflect quenching of the background by the VS; for a discussion, see Ref. [14]. For the present signals, comprised of discrete excess sources, a planar model may also be favored by catalog selection effects preferring VS-compressed sources seen edge-on, but we are unable to study this possibility or the nature of the $\tau \sim 6$ excess sources with the available statistics.

Better statistics and new constraints are expected with future source and cluster catalogs, and are already accessible in part with catalogs recently made available. Following this work, an analysis [50] of the *eROSITA*-DE Early Data Release (EDR) catalogs [51–53] established a significant, 3σ – 4σ excess of X-ray sources at $2.0 < \tau < 2.25$ radii around EDR clusters. In radio, the deep LOFAR Two-metre Sky Survey [LoTSS; 54] and Rapid ASKAP Continuum Survey [RACS; 55] can be used to test our results, supplement them with better statistics, stronger spectral constraints, and additional polarization information, and possibly extend them in the future to higher redshifts.

A study of individual VS-driven source candidates is beyond the scope of the present work, but should become feasible with future dedicated studies and upcoming catalogs. In particular, excess VS-driven radio sources, which should become clearer and more radially elongated at very low frequencies due to the longer $l_{\text{cool}} \propto \nu^{-1/2}$, may have already been observed, for example as the “accretion relic” or the NGC 4849 signature in Coma [56], both extending out to the IC-traced elliptical VS [17, 18]. In the absence of concrete examples of VS-driven sources or an excess of X-ray–radio pairs, our statistical determination of the excess-source properties relies on a fairly small number of sources, and may be confused by superimposing different types of sources. Thus, the physical origins of the X-ray and radio sources may differ more

significantly from each other than inferred above, and tentative bimodality signatures (*e.g.*, in a , b , φ , and T) may indicate multiple source types within each catalog.

The excess radio sources should emit an IC signal at hard X-ray and γ -ray energies ϵ . In the strong, $p \rightarrow 2$ shock limit, the anticipated IC luminosity of such a source is $\epsilon L_\epsilon^{(\text{IC})} \simeq (f_\epsilon/f_B)\nu L_\nu \simeq 10^{40-41} B_1^{-2} \text{ erg s}^{-1}$ (assuming $l_{\text{cool}} \simeq \Delta r$ for NVSS sources, as inferred in §6). Such values are comparable, for $B \simeq 1 \mu\text{G}$ fields within the source, to the luminosity of the entire VS ring, as inferred from γ -rays in stacked [13] and individual [17, 18, 20] clusters. Hence, a few such sources, activated by some VS, may outshine the entire IC signal from smooth accretion through this VS, especially at the lower energies ϵ accessible by the $p > 2$ source CREs. Similarly, a $\nu L_\nu \simeq 10^{40-41} \text{ erg s}^{-1}$ radio source outshines the $\nu L_\nu \simeq 10^{39} \text{ erg s}^{-1}$ synchrotron ring from smooth accretion (extrapolating the Ref. [14] signal to higher frequencies with their median parameters).

Nevertheless, the radiative VS signatures due to excess sources vs. smooth accretion are easily distinguished from each other by their markedly different properties, in particular brightness, extent, spectra, and cluster-mass dependence. For instance, in contrast to the strong M_{500} dependence anticipated and measured [14] for smooth accretion, we find no significant mass dependence in the excess-source properties, as demonstrated in Fig. 15. Moreover, localized sources were vigorously removed and masked in previous *Fermi*-LAT and LWA analyses. In contrast, a discrete source component cannot be ruled out in the somewhat high [20] VS flux inferred in Coma from VERITAS data [17].

The link established here between the VS and a coincident spike in discrete thermal (X-ray) and non-thermal (radio, and possibly also X-ray and γ -ray) sources opens new pathways to tracing the VS, mapping its relation to the cosmic web, and uncovering the underlying physical processes. If the multiple, bright peripheral X-ray sources per cluster reported previously at $z \sim 1$ are indeed identified with the VS, then the redshift evolution of VS sources is substantial, and similar analyses could shed light on the cosmological evolution of clusters, galaxies, galactic outflows, or other infalling objects. The strong, naively $L_X \propto \rho^2 \propto (1+z)^6$ redshift dependence of thermal emission from shocked objects would render them useful VS tracers at high redshifts. If the weak dependence of the signal upon host cluster, hinted by Fig. 15, is confirmed, then a radial spike in discrete sources around an object could map its VS even on small, sub-cluster scales.

ACKNOWLEDGEMENTS

We thank T. Boller, I. Rofeh, D. Kushnir, I. Gurwich, I. Reiss, Y. Lyubarsky, M. Gedalin, and Y. Faerman, for helpful discussions and support. This research has received funding from the Israel Science Foundation (ISF grants No. 1769/15 and 2126/22), from the IAEC-UPBC joint research foundation (grant No. 300/18), and from the Ministry of Science, Technology & Space, Israel. May Gideon Ilani's memory be a blessing.

-
- [1] J. T. Ruderman and H. Ebeling, *The Astrophysical Journal Letters* **623**, L81 (2005).
- [2] R. Fassbender, R. Šuhada, and A. Nastasi, *Advances in Astronomy* **2012**, 138380 (2012), [arXiv:1203.5337 \[astro-ph.CO\]](#).
- [3] E. Koulouridis, M. Plionis, O. Melnyk, *et al.*, *Astronomy & Astrophysics* **567**, A83 (2014).
- [4] S. Ehlert, S. W. Allen, W. N. Brandt, *et al.*, *MNRAS* **446**, 2709 (2015), [arXiv:1407.8181 \[astro-ph.GA\]](#).
- [5] R. Gilmour, P. Best, and O. Almaini, *MNRAS* **392**, 1509 (2009), [arXiv:0901.2810 \[astro-ph.GA\]](#).
- [6] W. Mo, A. Gonzalez, D. Stern, *et al.*, *The Astrophysical Journal* **869**, 131 (2018).
- [7] E. Koulouridis and I. Bartalucci, *Astronomy & Astrophysics* **623**, L10 (2019).
- [8] R. Vijayaraghavan and P. M. Ricker, *MNRAS* **435**, 2713 (2013), [arXiv:1308.1311 \[astro-ph.CO\]](#).
- [9] I. G. McCarthy, C. S. Frenk, A. S. Font, *et al.*, *MNRAS* **383**, 593 (2008), [arXiv:0710.0964 \[astro-ph\]](#).
- [10] U. Keshet, E. Waxman, A. Loeb, *et al.*, *ApJ* **585**, 128 (2003), [arXiv:astro-ph/0202318](#).
- [11] K. Schaal and V. Springel, *MNRAS* **446**, 3992 (2015), [arXiv:1407.4117 \[astro-ph.CO\]](#).
- [12] I. Reiss, J. Mushkin, and U. Keshet, in *Proceedings of the 7th International Fermi Symposium* (2017) p. 163, [arXiv:1712.06591 \[astro-ph.HE\]](#).
- [13] I. Reiss and U. Keshet, *J. Cosmology Astropart. Phys.* **2018**, 010 (2018), [arXiv:1705.05376 \[astro-ph.HE\]](#).
- [14] K.-C. Hou, G. Hallinan, and U. Keshet, *MNRAS* **521**, 5786 (2023), [arXiv:2210.09317 \[astro-ph.HE\]](#).
- [15] C. T. Pratt, Z. Qu, and J. N. Bregman, *ApJ* **920**, 104 (2021), [arXiv:2105.01123 \[astro-ph.CO\]](#).
- [16] D. Anbajagane, C. Chang, B. Jain, *et al.*, *MNRAS* **514**, 1645 (2022), [arXiv:2111.04778 \[astro-ph.CO\]](#).
- [17] U. Keshet, D. Kushnir, A. Loeb, and E. Waxman, *ApJ* **845**, 24 (2017).
- [18] U. Keshet and I. Reiss, *ApJ* **869**, 53 (2018).
- [19] G. Hurier, R. Adam, and U. Keshet, *A&A* **622**, A136 (2019).
- [20] U. Keshet, I. Reiss, and G. Hurier, *ApJ* **895**, 72 (2020), [arXiv:1801.01494 \[astro-ph.CO\]](#).

- [21] S. More, H. Miyatake, M. Takada, *et al.*, *ApJ* **825**, 39 (2016), [arXiv:1601.06063 \[astro-ph.CO\]](#).
- [22] T. Shin, S. Adhikari, E. J. Baxter, *et al.*, *MNRAS* **487**, 2900 (2019), [arXiv:1811.06081 \[astro-ph.CO\]](#).
- [23] T. Boller, M. J. Freyberg, J. Trümper, *et al.*, *A&A* **588**, A103 (2016), [arXiv:1609.09244 \[astro-ph.HE\]](#).
- [24] J. J. Condon, W. D. Cotton, E. W. Greisen, *et al.*, *AJ* **115**, 1693 (1998).
- [25] R. Piffaretti, M. Arnaud, G. W. Pratt, *et al.*, *A&A* **534**, A109 (2011), [arXiv:1007.1916](#).
- [26] H. T. Intema, P. Jagannathan, K. P. Mooly, and D. A. Frail, *A&A* **598**, A78 (2017), [arXiv:1603.04368 \[astro-ph.CO\]](#).
- [27] W. M. Lane, W. D. Cotton, S. van Velzen, *et al.*, *MNRAS* **440**, 327 (2014), [arXiv:1404.0694 \[astro-ph.IM\]](#).
- [28] C. G. T. Haslam, F. D. Kahn, and J. Meaburn, *A&A* **12**, 388 (1971).
- [29] C. Dickinson, *Galaxies* **6**, 56 (2018).
- [30] D. A. Green, Bulletin of the Astronomical Society of India **39**, 289 (2011), [arXiv:1108.5083 \[astro-ph.IM\]](#).
- [31] R. Mewe, J. R. Lemen, and G. H. J. van den Oord, *A&AS* **65**, 511 (1986).
- [32] A. Kimball, K. Kellermann, J. Condon, *et al.*, *The Astrophysical Journal Letters* **739**, L29 (2011).
- [33] J. R. Mattox, D. L. Bertsch, J. Chiang, *et al.*, *ApJ* **461**, 396 (1996).
- [34] S. S. Wilks, *The Annals of Mathematical Statistics* **9**, 60 (1938).
- [35] U. Keshet, *MNRAS* **527**, 1194 (2024), [arXiv:2303.08146 \[astro-ph.HE\]](#).
- [36] A. R. Taylor, J. M. Stil, and C. Sunstrum, *ApJ* **702**, 1230 (2009).
- [37] A. Loeb and E. Waxman, *Nature* **405**, 156 (2000), [arXiv:astro-ph/0003447](#).
- [38] T. Totani and T. Kitayama, *ApJ* **545**, 572 (2000), [arXiv:astro-ph/0006176](#).
- [39] E. Waxman and A. Loeb, *ApJ* **545**, L11 (2000), [arXiv:astro-ph/0007049](#).
- [40] U. Keshet, E. Waxman, and A. Loeb, *J. Cosmology Astropart. Phys.* **4**, 6 (2004), [arXiv:astro-ph/0306442](#).
- [41] M. Arnaud, G. W. Pratt, R. Piffaretti, *et al.*, *A&A* **517**, A92 (2010), [arXiv:0910.1234 \[astro-ph.CO\]](#).
- [42] Planck Collaboration, P. A. R. Ade, N. Aghanim, *et al.*, *A&A* **550**, A131 (2013), [arXiv:1207.4061 \[astro-ph.CO\]](#).
- [43] M. E. Anderson, M. Gaspari, S. D. M. White, *et al.*, *MNRAS* **449**, 3806 (2015), [arXiv:1409.6965 \[astro-ph.CO\]](#).
- [44] Y. Faerman, A. Sternberg, and C. F. McKee, *ApJ* **893**, 82 (2020), [arXiv:1909.09169 \[astro-ph.GA\]](#).
- [45] U. Keshet, O. Arad, and Y. Lyubarski, *ApJ* **891**, 117 (2020), [arXiv:1910.08083 \[astro-ph.HE\]](#).
- [46] W. I. Axford, E. Leer, and G. Skadron, in *International Cosmic Ray Conference*, International Cosmic Ray Conference, Vol. 11 (1977) pp. 132–137.
- [47] G. F. Krymskii, *Akademiia Nauk SSSR Doklady* **234**, 1306 (1977).
- [48] A. R. Bell, *MNRAS* **182**, 147 (1978).
- [49] R. D. Blandford and J. P. Ostriker, *ApJ* **221**, L29 (1978).
- [50] G. Ilani, K.-C. Hou, G. Nadler, and U. Keshet, *A&A* **686**, L16 (2024), [arXiv:2402.17822 \[astro-ph.HE\]](#).
- [51] H. Brunner, T. Liu, G. Lamer, *et al.*, *A&A* **661**, A1 (2022), [arXiv:2106.14517 \[astro-ph.HE\]](#).
- [52] A. Liu, E. Bulbul, V. Ghirardini, *et al.*, *A&A* **661**, A2 (2022), [arXiv:2106.14518 \[astro-ph.CO\]](#).
- [53] Y. E. Bahar, E. Bulbul, N. Clerc, *et al.*, *A&A* **661**, A7 (2022).
- [54] T. W. Shimwell, C. Tasse, M. J. Hardcastle, *et al.*, *A&A* **622**, A1 (2019), [arXiv:1811.07926 \[astro-ph.GA\]](#).
- [55] D. McConnell, C. L. Hale, E. Lenc, *et al.*, *PASA* **37**, e048 (2020), [arXiv:2012.00747 \[astro-ph.IM\]](#).
- [56] A. Bonafede, G. Brunetti, L. Rudnick, *et al.*, *ApJ* **933**, 218 (2022), [arXiv:2203.01958 \[astro-ph.HE\]](#).

Supplementary Material

Appendix A: Spectral modeling

Figure A.1 shows that while the radio spectral index has a significant $\sim 5\sigma$ excess of $\alpha_{150\text{ MHz}}^{1.4\text{ GHz}} \simeq 0.55$ indices associated with ~ 10 sources, and, in addition, indications of ~ 10 more $0.6 \lesssim \alpha_{150\text{ MHz}}^{1.4\text{ GHz}} \lesssim 0.8$ excess sources

(right panel), there is no consistent signal in the Γ_X distribution of X-ray spectral indices in the power-law fit (left panel). The temperatures of both Mekeal and black-body X-ray spectral fits in Fig. A.2 show a more localized excess, consistent with about half of the excess sources having $T \gtrsim 1$ keV temperatures.

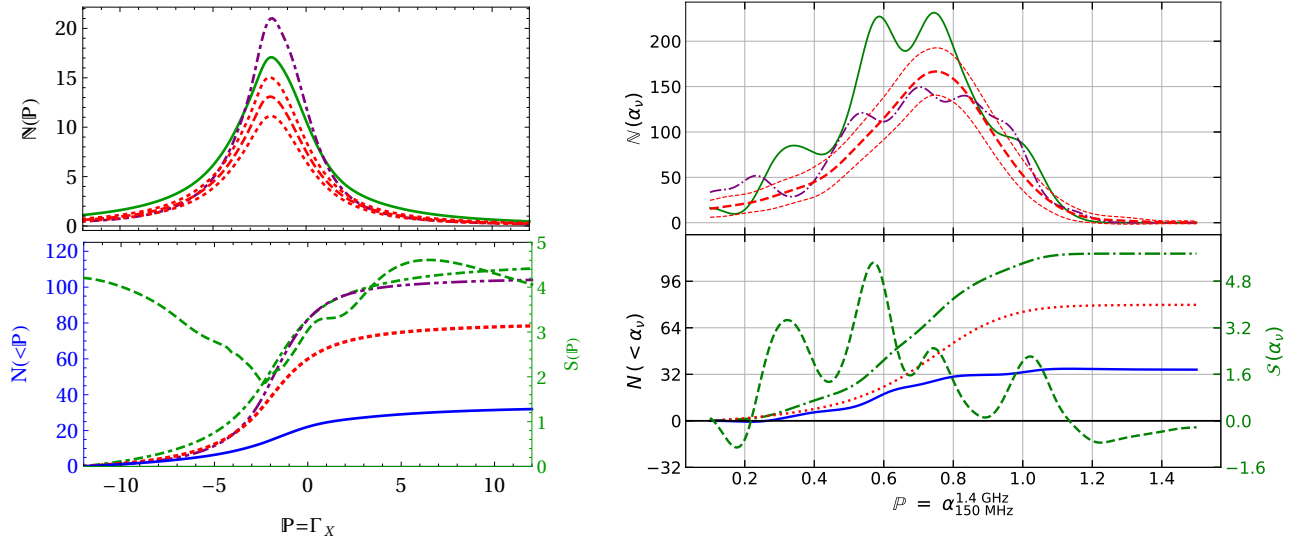


FIG. A.1. Distributions of power-law spectral indices $\mathbb{P} = \Gamma_X$ in X-rays (left panel) and $\mathbb{P} = \alpha_{150\text{ MHz}}^{1.4\text{ GHz}}$ in radio (right); notations are the same as in Fig. 7.

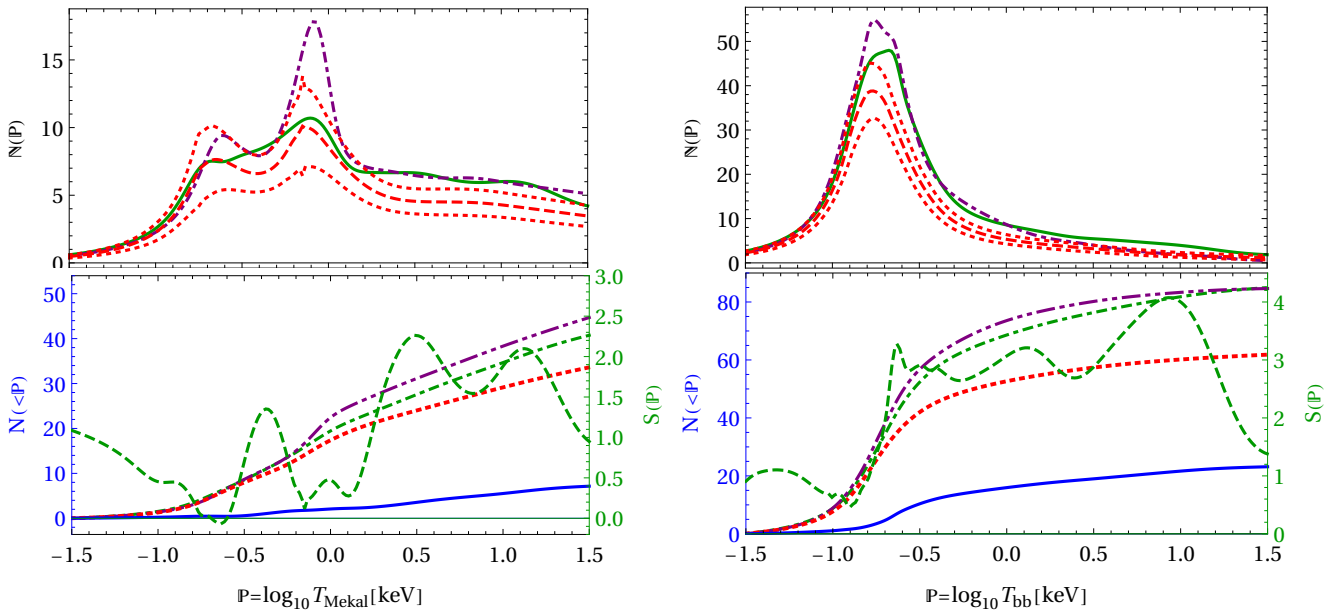


FIG. A.2. Distribution of X-ray Mekeal (left) and black-body (right) fitted temperature $\mathbb{P} = \log_{10} T$. Notations are as in Fig. 11.

Appendix B: Catalog source sizes

The 2RXS catalog provides an estimate of the angular extent of each source, expressed (T. Boller, private communications 2020) as the radius of the source minus the radius of the point spread function (PSF). For simplicity, we approximate the source radius as the e-fold drop in photon distribution [1]. The PSF varies with the location of the source across the PSPC field of view, so we adopt an averaged, approximate PSF value. For this purpose, we take the e-fold radius of the RASS PSF model [2], providing an estimated radius $r_{psf} \sim 40''$. We verify that this result is sensible, by examining individual sources. Our conclusions are not sensitive to the precise value of the actual PSF.

The NVSS catalog provides the FWHM major axes $2a$ and minor axes $2b$ of sources, constrained in the range $14'' < 2b < 2a < 286''$. Source localizations have an angular precision of $\gtrsim 7''$ for sources fainter than 15 mJy, but the brighter sources comprising our sample have a high, $\gtrsim 1''$ precision.

Appendix C: Confidence levels for Poisson statistics

Monte-Carlo simulations were used to numerically estimate the CLs S_p for Poisson, rather than normal, statistics, demonstrated in Fig. 3 (the empty black symbols show the S values corresponding to $S_p = \pm 1, \pm 2 \dots$), but it is useful to derive an approximate expression for S given S_p . For a Poisson distribution of mean λ , where measurement k has probability $p(k) = e^{-\lambda} \lambda^k / k!$, we may analytically sum the probabilities of equal or larger (smaller) k values, in order to quantify the significance of an excess (deficit) in units of Gaussian standard errors,

$$S_p(k; \lambda) = \begin{cases} \sqrt{2} \operatorname{erfc}^{-1} \left[\frac{\Gamma(k) - \Gamma(k, \lambda)}{\Gamma(k)/2} \right] > 0 & \text{if } k > \lambda; \\ -\sqrt{2} \operatorname{erfc}^{-1} \left[\frac{\Gamma(1+k, \lambda)}{\Gamma(1+k)/2} \right] < 0 & \text{if } k < \lambda; \\ 0 & \text{if } k = \lambda, \end{cases} \quad (\text{C.1})$$

where $\operatorname{erfc}(x)$ and $\Gamma(x)$ are respectively the complementary error and Euler Gamma functions. For SW co-addition, where S_{sw} is the function of \mathcal{N} and \mathcal{F} given in Eq. (3.13), one can thus relate S_{sw} to S_p for any given \mathcal{F} by solving the equation

$$S_p = S_p(\mathcal{N} = \mathcal{F} + S_{\text{sw}} \sqrt{\mathcal{F}}; \mathcal{F}). \quad (\text{C.2})$$

The resulting S_{sw} profiles are shown for integer S_p values in the SW figures (as dashed black curves).

For modelling, we Monte-Carlo simulate our χ_{sw}^2 and χ_{CW}^2 expressions under the field-only null hypothesis and Poisson statistics. We verify that the results follow the expected χ^2 distributions, thus justifying the parameter fit and TS significance estimates. In particular, when fitting models to the stacked excess, we estimate the relative goodness of fit using the TS test, following Eqs. (3.28)–(3.30) and Wilks' theorem [3], which are

based on underlying normal statistics. To verify that the results do not change significantly under Poisson statistics, we use Monte-Carlo simulations, with the null hypothesis of Poisson-distributed field sources only, to estimate χ^2 and TS. The resulting distributions are found to closely follow the anticipated χ_n^2 distribution with the correct effective number n of degrees of freedom.

Appendix D: Convergence and sensitivity tests

Our results are qualitatively insensitive to variations in the selection criteria (of clusters, sources, or field sources) and analysis methods (of field removal and source binning, stacking, or modeling). This robustness is demonstrated in Figs. D.1–D.7 below, each varying some analysis parameter with little qualitative impact on the outcome with respect to the nominal results (which are shown for reference as a solid red curve in most figures).

In particular, the results are shown to be robust to variations in the $|b|$ cut (Fig. D.1), the masking of clusters in different sky regions and the minimal projected cluster interdistance (Fig. D.2), the order of the polynomial fit to the field source distribution \mathcal{F} around each cluster (Fig. D.3), the radial $\Delta\tau$ resolution (Fig. D.4), the X-ray and radio flux cutoffs F^* (Fig. D.5), the likelihood \mathcal{L} cutoff on the X-ray sources (Fig. D.6), and the presentation and folding of stacked sources in 2D sky coordinates (*e.g.*, varying the resolution and smoothing of the map; Fig. D.7). When adopting the nominal, constant density \mathcal{F} of field sources (*i.e.* a polynomial of order zero) around each cluster, we vary the region used to measure \mathcal{F} , with inner radii spanning the range 1° – 5° and outer radii in the range 6° – 10° , resulting in only negligible changes to the $S(\tau)$ profile.

The same procedure used to test for a mass dependence in Fig. 15 is used in Fig. D.8 to examine the dependence of the excess upon θ_{500} , here with six bins of ~ 150 clusters each, extending beyond the nominal θ_{500} range. For sufficiently extended clusters, the θ_{500} dependence appears to be weak. However, the VS excess entirely vanishes for compact, $\theta_{500} \lesssim 0.1$ clusters, at least in X-rays. The high resolutions of the catalogs suggest that this disappearance is association with the intrinsic widths of the signals. Indeed, this cutoff scale corresponds to $d_A(\bar{z})\theta_{500}\Delta\tau \simeq 140$ kpc, broadly consistent with the signal widths inferred in §4. Here, d_A is the angular diameter distance, and we adopted the median $\bar{z} \simeq 0.08$ redshift in the sample.

Variations in the modelling of the VS excess are demonstrated in Table III, expanding on the nominal models presented in Table II. Here, we also examine the use of priors on the model (numbers in **bold** are frozen parameters). As the table shows, the determination of the position and width of the VS excess is robust, and the significance of the detection increases if prior information, in particular regarding the shock position, is used.

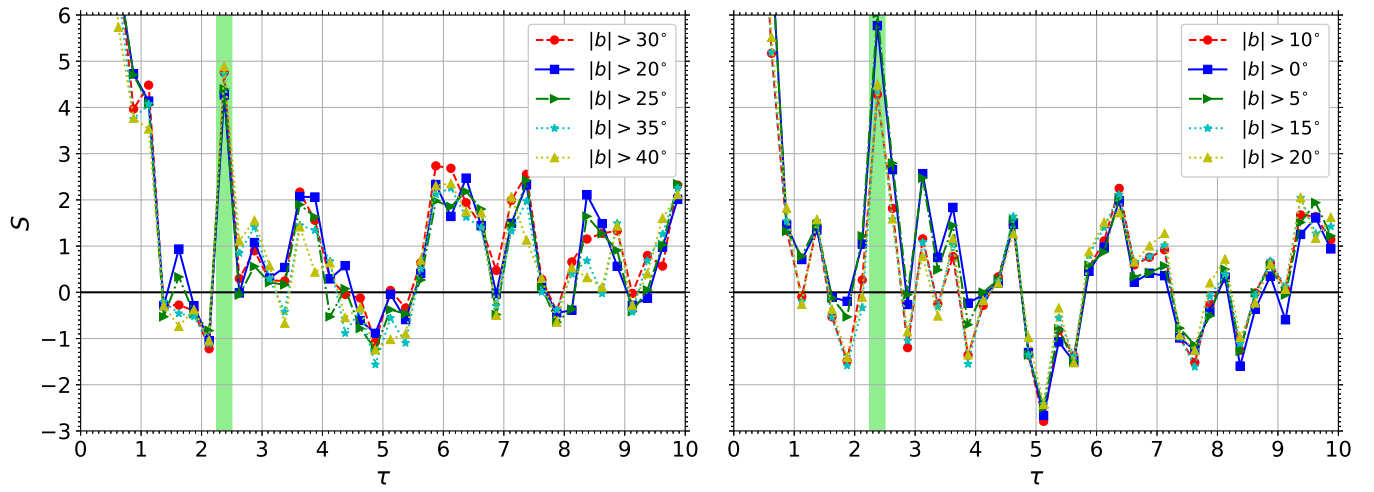


FIG. D.1. Significance $S(\tau)$ profiles of the SW-stacked X-ray (left panel) and radio (right panel) source excess under variations in the Galactic latitude cutoff $|b|$ (see legend); the nominal analysis is shown, for reference, as a solid red curve. The anticipated VS region is highlighted as in Fig. 3. Notice the contribution of $|b| < 10^\circ$ radio sources, neglected in the nominal analysis.

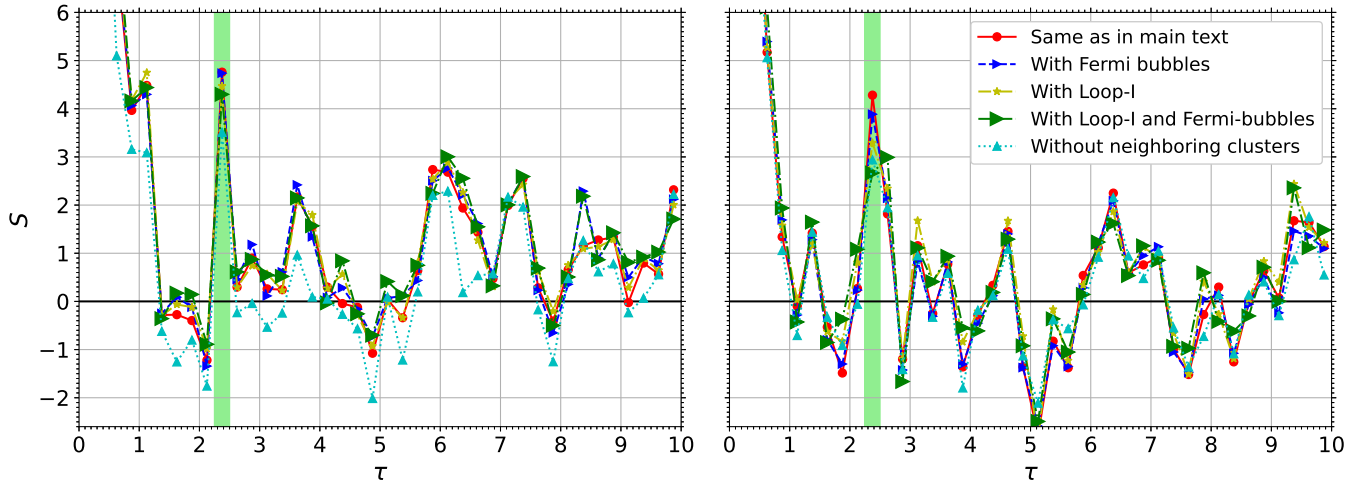


FIG. D.2. Variations in cluster masking in different regions (see legend), with neighboring clusters defined as pairs within $5\theta_{500}$ in projection; notations are the same as in Fig. D.1.

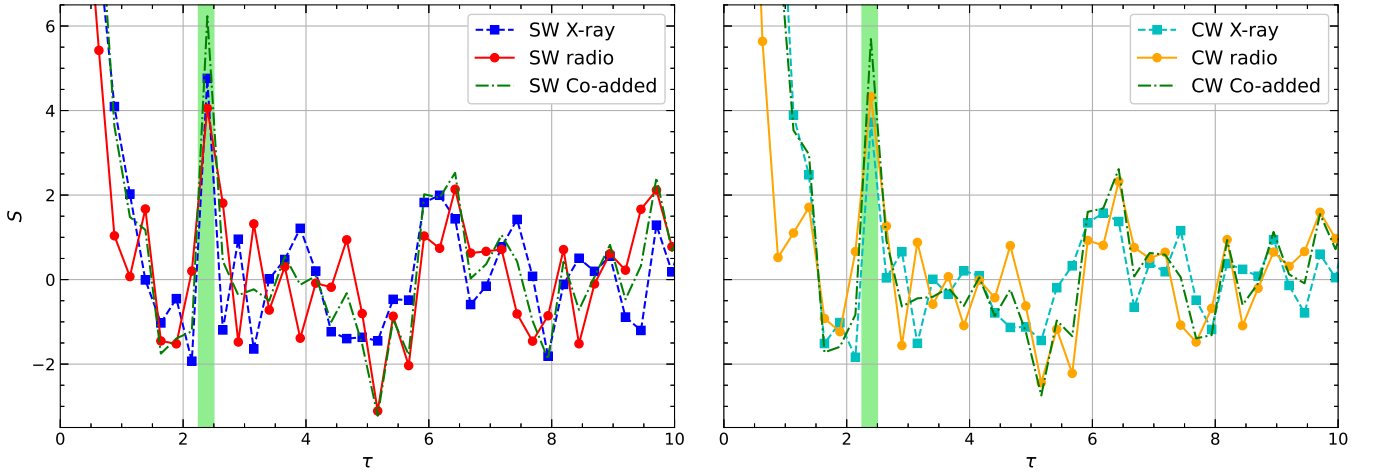


FIG. D.3. Same as the nominal Fig. 4, but with field source densities \mathcal{F} inferred from a fourth-order polynomial fit to their sky distribution within $1 \leq \tau \leq 15$ around each cluster.

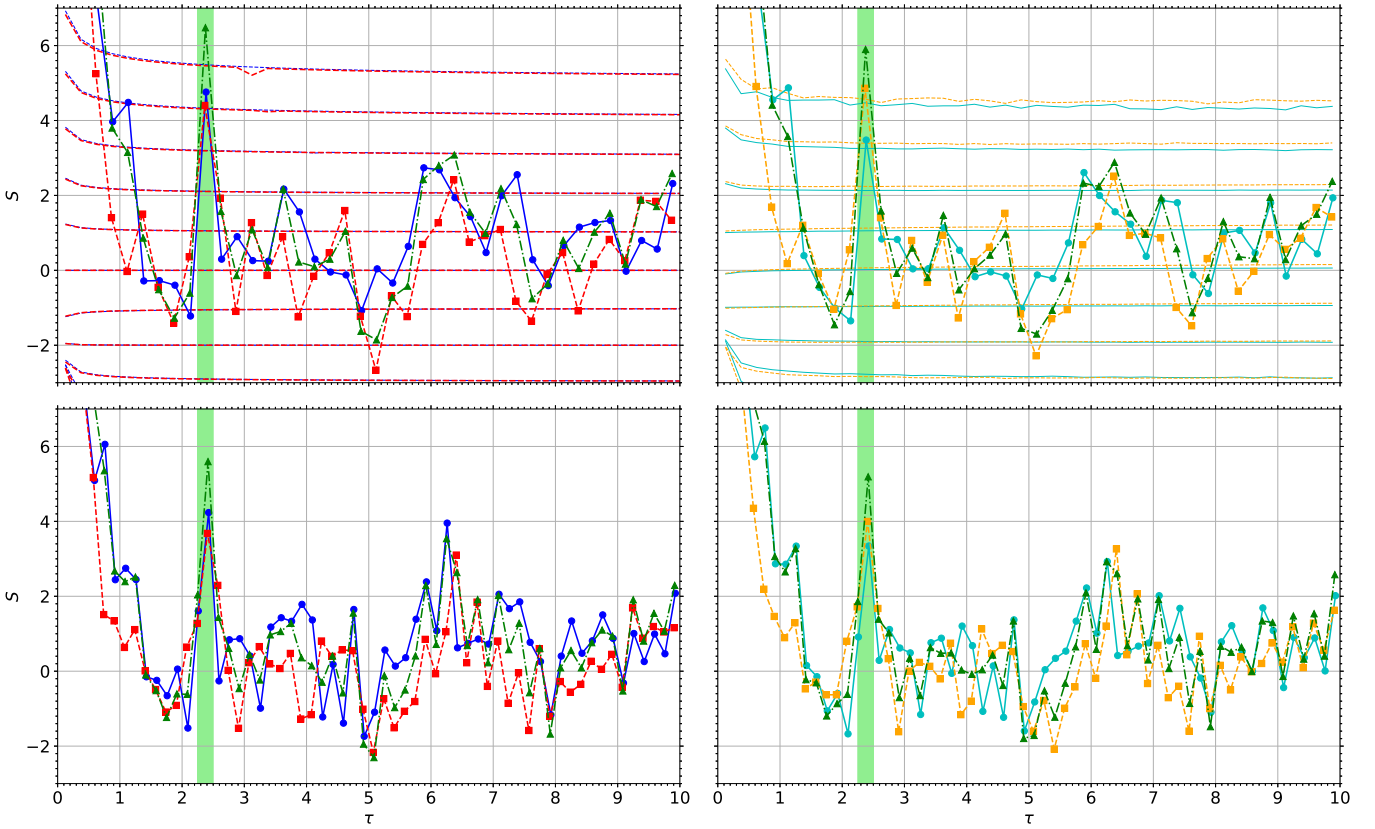


FIG. D.4. Same as the nominal Fig. 4, comparing $\Delta\tau = 1/4$ (top panels) and $\Delta\tau = 1/6$ (bottom) resolutions.

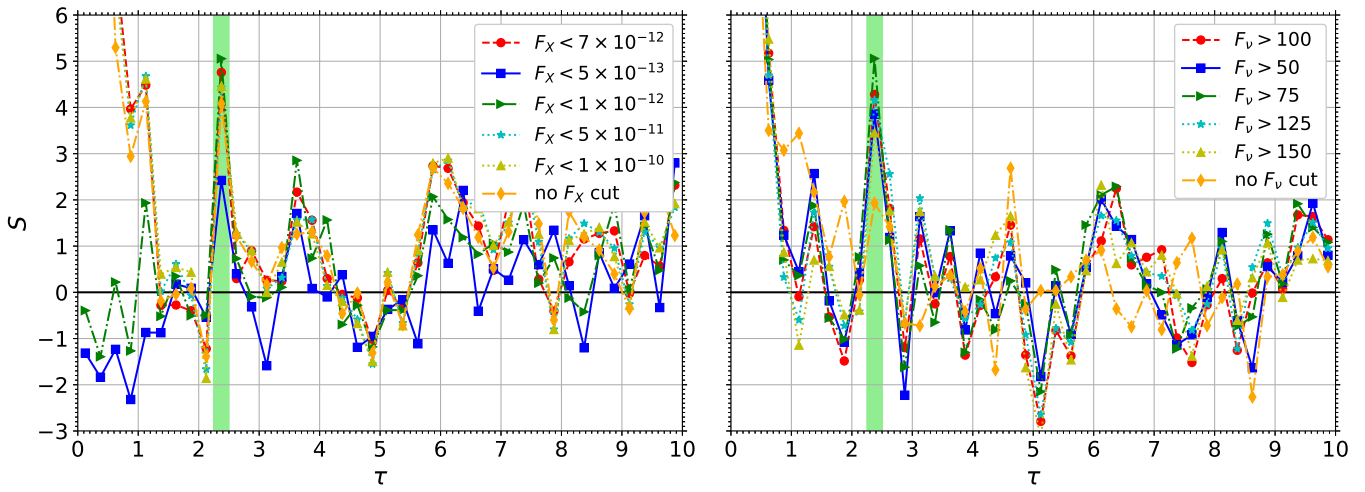


FIG. D.5. Variations in flux cutoffs (see legend), including the case of no flux cut at all (orange diamonds); notations are the same as in Fig. D.1.

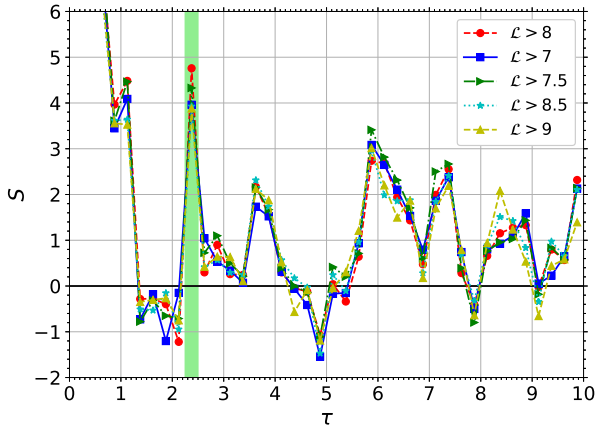


FIG. D.6. Variations in X-ray source likelihood (see legend); notations are the same as in the left panel of Fig. D.1.

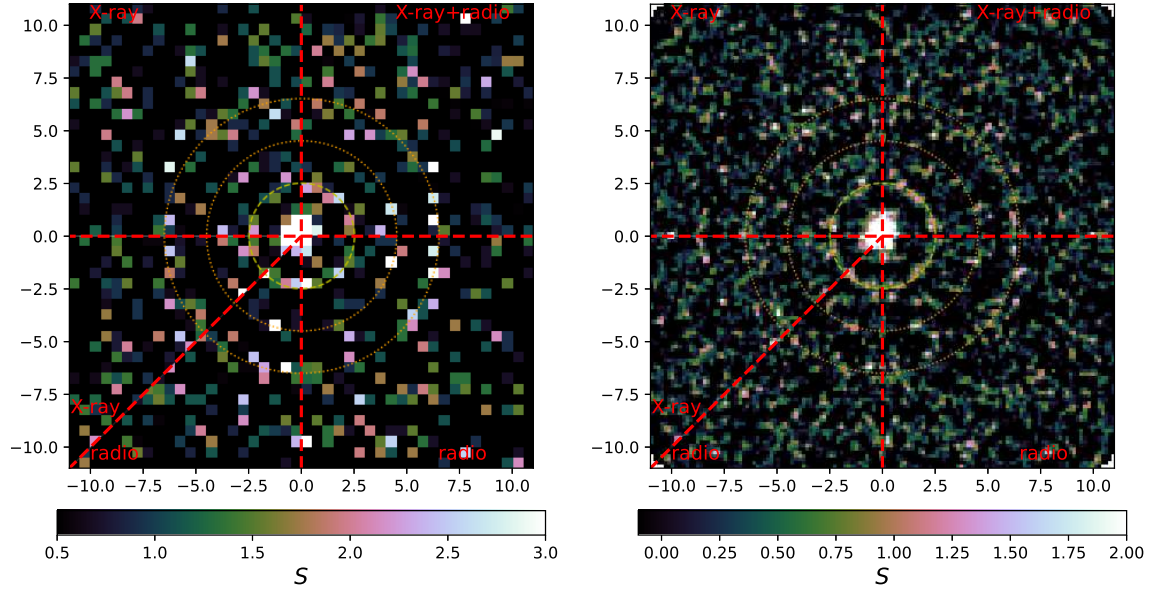


FIG. D.7. Same as Fig. 5, but for $\Delta\tau = 1/2$ resolution (left panel) or after convolution with a Gaussian matrix of $0.5\theta_{500}$ standard deviation (right panel).

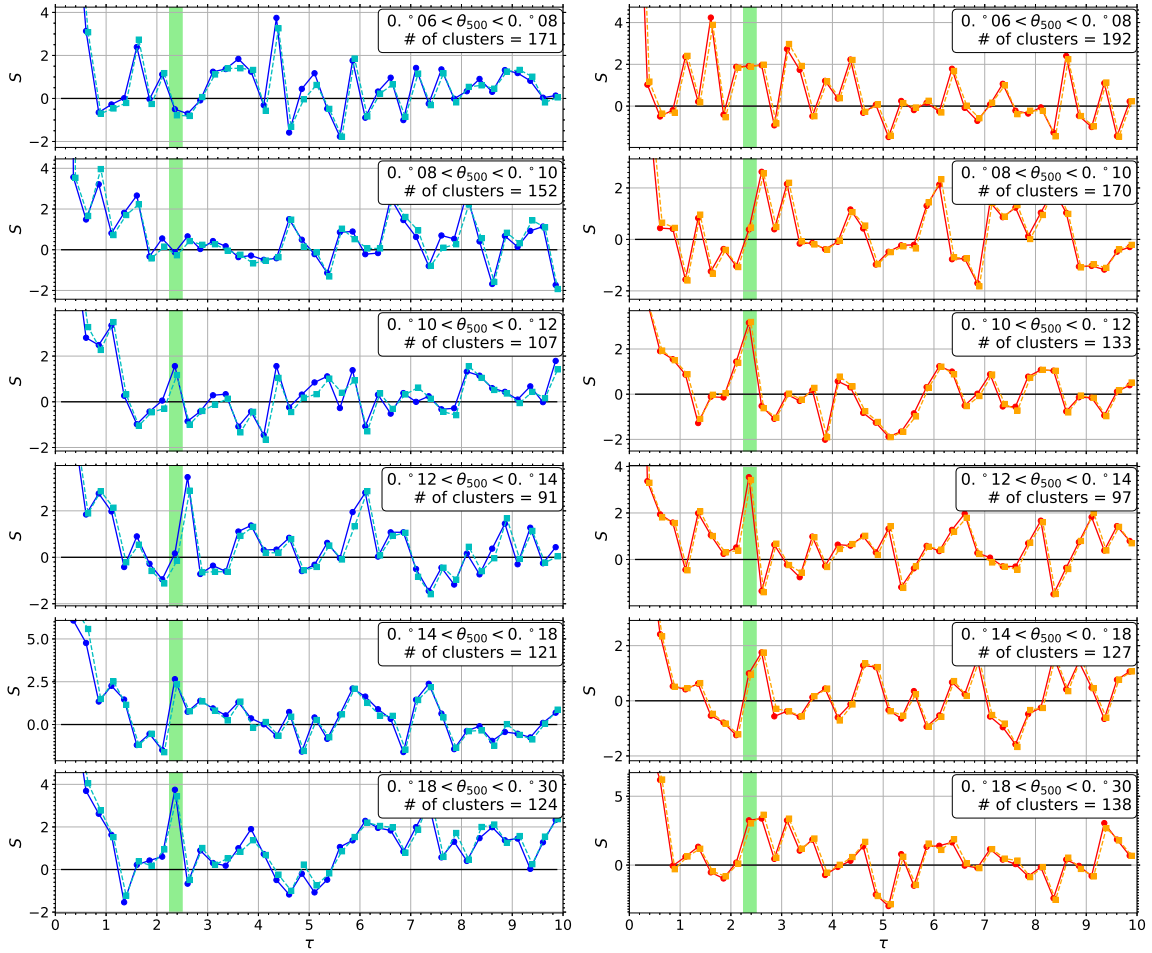


FIG. D.8. Same as Fig. 15, but for different θ_{500} bins (see legend).

TABLE III. Best-fitted parameters for different variants of the virial-excess model.

Method (1)	$\Delta\tau$ (2)	Catalog (3)	Model (4)	n (5)	$n_{0,x}$ (6)	$n_{0,r}$ (7)	τ_{sh} (8)	$\Delta\tau_{sh}$ (9)	TS (10)	σ_{TS} (11)	
SW	1/4	2RXS	Shell	2	$7.0^{+2.2}_{-2.0}$	—	$2.50^{+0.00}_{-0.02}$	—	14.0	3.32	
			Planar	1	$5.4^{+1.5}_{-1.6}$	—	2.40	0.01	22.8	4.77	
			Planar	2	$5.4^{+1.6}_{-1.1}$	—	2.40	$0.05^{+0.04}_{-0.05}$	22.8	4.39	
			Planar	3	$5.4^{+2.1}_{-1.7}$	—	$2.44^{+0.06}_{-0.19}$	$0.04^{+0.05}_{-0.04}$	22.8	4.08	
			NVSS	Shell	2	—	$8.4^{+2.5}_{-2.4}$	$2.52^{+0.05}_{-0.02}$	—	14.7	3.42
				Planar	1	—	$6.9^{+1.9}_{-1.7}$	2.40	0.01	21.3	4.61
		Planar	2	—	$6.9^{+1.4}_{-1.4}$	2.40	$0.12^{+0.04}_{-0.04}$	21.3	4.23		
		Planar	3	—	$6.6^{+2.1}_{-2.0}$	$2.44^{+0.06}_{-0.06}$	$0.10^{+0.05}_{-0.10}$	21.7	3.96		
		Joint	Shell	3	$7.0^{+2.2}_{-2.0}$	$6.9^{+0.7}_{-0.7}$	$2.50^{+0.24}_{-0.25}$	—	27.8	4.61	
			Planar	2	$6.1^{+1.2}_{-1.2}$	$5.9^{+1.2}_{-1.2}$	2.40	0.01	42.6	6.20	
		Planar	3	$6.1^{+1.2}_{-1.2}$	$6.9^{+0.7}_{-0.7}$	2.40	$0.09^{+0.03}_{-0.03}$	42.6	5.93		
		Planar	4	$5.9^{+1.7}_{-1.5}$	$5.7^{+1.7}_{-1.6}$	$2.47^{+0.02}_{-0.02}$	$0.04^{+0.02}_{-0.02}$	43.3	5.75		
	1/6	2RXS	Shell	2	$8.2^{+1.4}_{-3.4}$	—	$2.50^{+0.00}_{-0.04}$	—	14.2	3.34	
			Planar	1	$5.3^{+1.5}_{-1.5}$	—	2.40	0.01	19.8	4.45	
			Planar	2	$5.3^{+1.6}_{-1.6}$	—	2.40	$0.07^{+0.03}_{-0.03}$	19.8	4.06	
			Planar	3	$5.5^{+1.6}_{-1.5}$	—	$2.35^{+0.05}_{-0.02}$	$0.03^{+0.04}_{-0.03}$	20.6	3.83	
			NVSS	Shell	2	—	$8.1^{+2.4}_{-2.3}$	$2.54^{+0.06}_{-0.03}$	—	14.0	3.32
				Planar	1	—	$6.9^{+1.9}_{-1.8}$	2.40	0.01	19.8	4.45
		Planar	2	—	$6.9^{+2.1}_{-1.4}$	2.40	$0.14^{+0.04}_{-0.04}$	19.8	4.06		
		Planar	3	—	$6.5^{+2.1}_{-1.8}$	$2.44^{+0.04}_{-0.05}$	$0.12^{+0.05}_{-0.04}$	20.4	3.81		
		Joint	Shell	3	$7.3^{+2.3}_{-2.1}$	$6.8^{+2.2}_{-2.1}$	$2.50^{+0.83}_{-0.78}$	—	25.8	4.41	
			Planar	2	$5.8^{+1.2}_{-1.2}$	$5.9^{+1.2}_{-1.2}$	2.40	0.01	38.0	5.83	
		Planar	3	$5.8^{+1.2}_{-1.2}$	$5.9^{+1.8}_{-1.2}$	$0.10^{+0.03}_{-0.02}$	2.40	38.0	5.55		
		Planar	4	$5.8^{+1.7}_{-1.5}$	$5.9^{+1.9}_{-1.7}$	$2.41^{+0.02}_{-0.02}$	$0.10^{+0.03}_{-0.02}$	38.1	5.31		
CW	1/4	2RXS	Shell	2	$4.2^{+2.1}_{-1.9}$	—	$2.50^{+0.02}_{-0.05}$	—	5.9	1.94	
			Planar	1	$3.7^{+1.4}_{-1.1}$	—	2.40	0.01	12.1	3.48	
			Planar	2	$3.7^{+1.5}_{-1.1}$	—	2.40	$0.01^{+0.03}_{-0.01}$	12.1	3.04	
			Planar	3	$4.3^{+1.7}_{-1.5}$	—	$2.47^{+0.03}_{-0.21}$	$0.04^{+0.05}_{-0.04}$	12.8	2.80	
			NVSS	Shell	2	—	$7.6^{+2.4}_{-2.2}$	$2.50^{+0.03}_{-0.03}$	—	18.9	3.95
				Planar	1	—	$6.3^{+1.7}_{-1.5}$	2.40	0.01	24.9	4.99
		Planar	2	—	$6.3^{+1.9}_{-1.3}$	2.40	$0.11^{+0.03}_{-0.03}$	24.9	4.62		
		Planar	3	—	$6.2^{+1.9}_{-2.0}$	$2.41^{+0.08}_{-0.06}$	$0.11^{+0.04}_{-0.10}$	24.9	4.32		
		Joint	Shell	3	$4.9^{+2.4}_{-2.1}$	$7.7^{+0.7}_{-0.8}$	$2.50^{+0.24}_{-0.25}$	—	27.5	4.58	
			Planar	2	$3.8^{+1.2}_{-1.2}$	$5.9^{+1.8}_{-1.2}$	2.40	0.01	36.9	5.74	
		Planar	3	$3.8^{+1.2}_{-1.2}$	$7.7^{+0.7}_{-0.8}$	2.40	$0.10^{+0.03}_{-0.03}$	36.9	5.46		
		Planar	4	$3.8^{+1.4}_{-1.2}$	$5.5^{+2.1}_{-1.6}$	$2.47^{+0.02}_{-0.02}$	$0.04^{+0.02}_{-0.02}$	37.5	5.26		
	1/6	2RXS	Shell	2	$4.3^{+2.0}_{-1.8}$	—	$2.50^{+0.01}_{-0.04}$	—	6.7	2.10	
			Planar	1	$3.8^{+1.5}_{-1.2}$	—	2.40	0.01	12.0	3.47	
			Planar	2	$3.8^{+1.5}_{-1.2}$	—	2.40	$0.07^{+0.04}_{-0.07}$	12.0	3.03	
			Planar	3	$3.9^{+1.7}_{-1.5}$	—	$2.39^{+0.10}_{-0.06}$	$0.07^{+0.04}_{-0.07}$	12.1	2.69	
			NVSS	Shell	2	—	$7.6^{+2.3}_{-2.2}$	$2.51^{+0.03}_{-0.01}$	—	16.7	3.68
				Planar	1	—	$6.3^{+1.7}_{-1.6}$	2.40	0.01	22.0	4.69
		Planar	2	—	$6.3^{+1.9}_{-1.3}$	2.40	$0.14^{+0.05}_{-0.04}$	22.0	4.30		
		Planar	3	—	$6.2^{+2.1}_{-1.8}$	$2.42^{+0.05}_{-0.05}$	$0.13^{+0.05}_{-0.04}$	22.1	4.00		
		Joint	Shell	3	$4.8^{+2.4}_{-2.1}$	$7.2^{+0.7}_{-0.7}$	$2.51^{+0.24}_{-0.25}$	—	25.0	4.33	
			Planar	2	$3.8^{+1.1}_{-1.1}$	$5.6^{+1.1}_{-1.1}$	2.40	0.01	33.2	5.42	
		Planar	3	$3.8^{+1.1}_{-1.1}$	$7.2^{+0.7}_{-0.7}$	2.40	$0.10^{+0.04}_{-0.02}$	33.2	5.13		
		Planar	4	$3.7^{+1.5}_{-1.3}$	$5.6^{+1.8}_{-1.6}$	$2.41^{+0.02}_{-0.02}$	$0.10^{+0.04}_{-0.02}$	33.3	4.88		

Table columns: (1) Co-addition method (SW or CW); (2) Dimensionless (in θ_{500} units) binning resolution; (3) Stacked catalog (2RXS, NVSS, or joint catalogs); (4) Effective VS model (planar or shell); (5) Effective number of free parameters; (6) and (7) Normalized, $n_0^* \equiv 10^3 n_0$ X-ray and radio source densities in Eqs. (3.24) or (3.26); (8) Dimensionless shock radius; (9) Dimensionless signal width; (10) TS value; (11) TS-based significance. Numbers in **bold** are imposed constraints.

Appendix E: Additional VS excess-source properties

Figures E.1–E.6 demonstrate additional properties of the VS-excess sources, inferred in the same statistical method used in §5.

Figure E.1 shows that the black-body X-ray fit indicates similar, $L_X \simeq 10^{42-43}$ erg s⁻¹ luminosities as those inferred from the power-law fit. Next, a comparison of normalized and non-normalized sizes is shown for X-ray (Fig. E.2) and radio (Fig. E.3) sources.

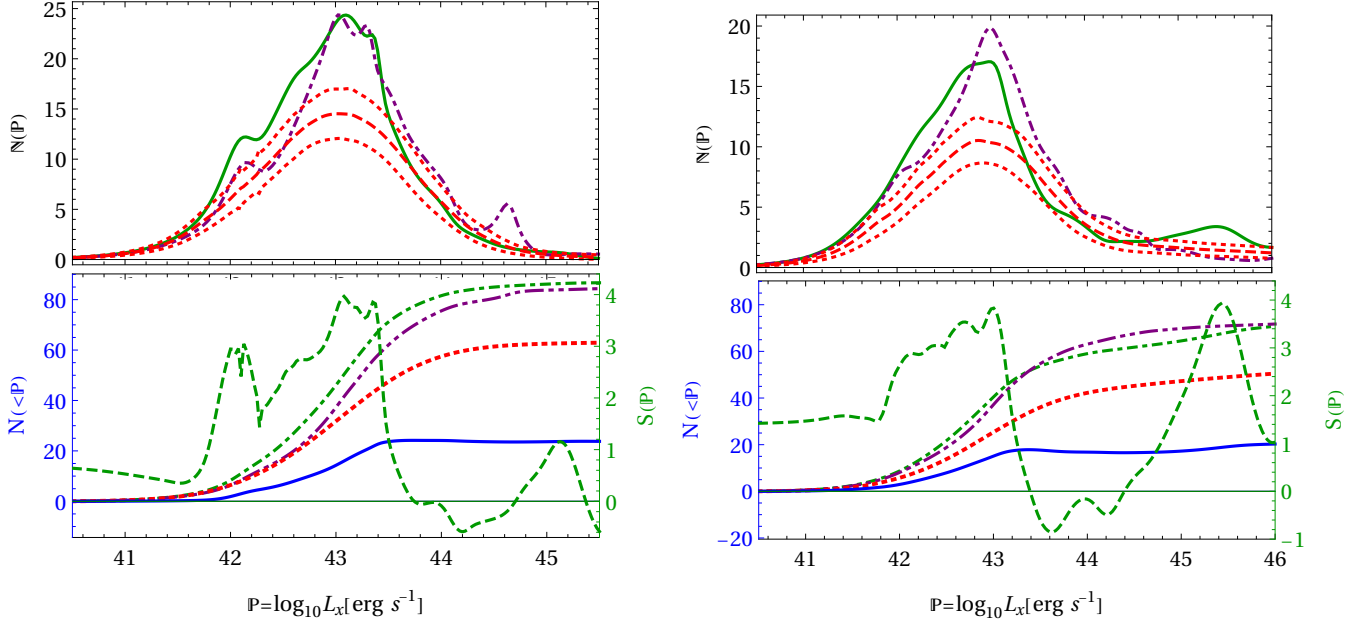


FIG. E.1. Distribution of X-ray luminosity $\mathbb{P} = \log_{10} L_X$ according to power-law (left panel) and black-body (right panel) spectral fits. Notations are the same as in Fig. 11.

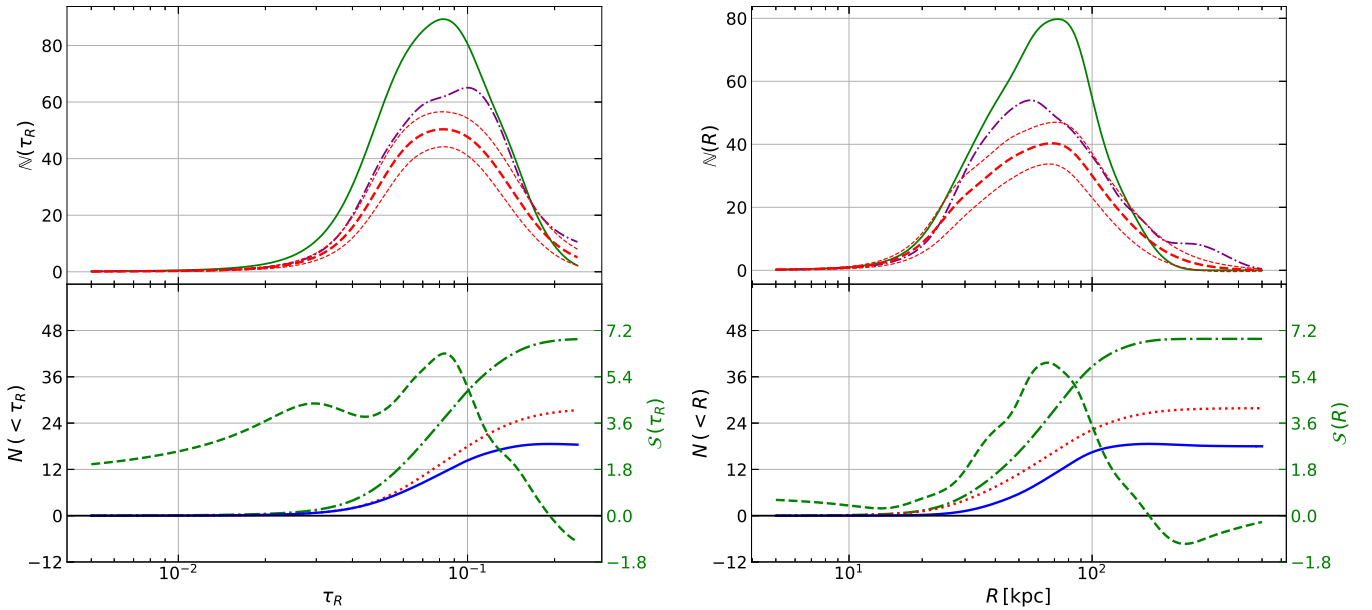


FIG. E.2. Distributions of normalized (to θ_{500}), dimensionless $\mathbb{P} = \tau_R$ (left panel) and non-normalized $\mathbb{P} = R$ (right panel) 2RXS source radii. Notations are the same as in Fig. 7.

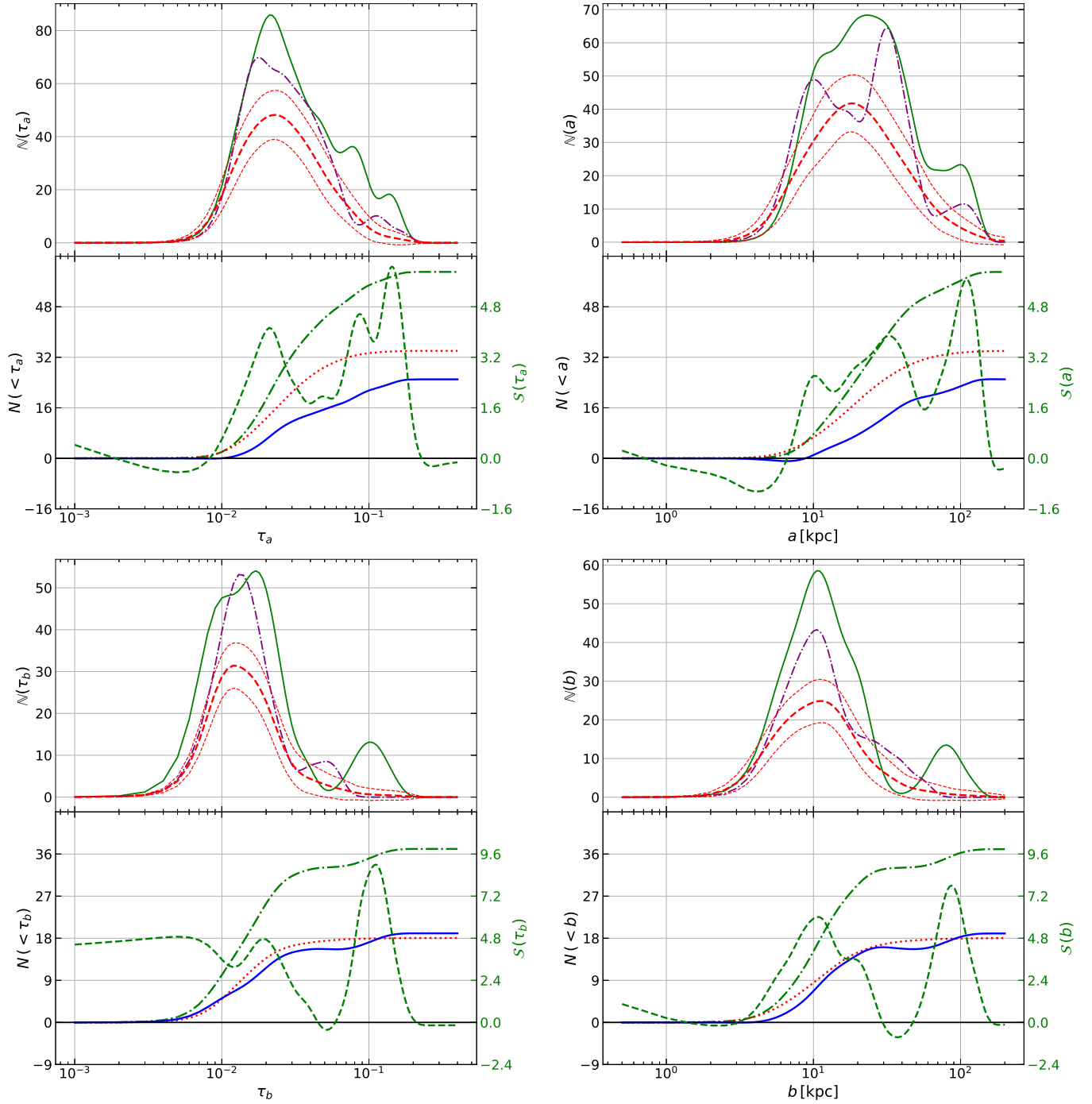


FIG. E.3. The same as Fig. E.2, but for the semi-major ($\mathbb{P} = a$, upper panels) and semi-minor ($\mathbb{P} = b$, lower panels) axes of radio sources. A variance $\sigma_{\text{smooth}}^2(x) = (0.2x)^2$ is added to each scale x , for visibility.

Figure E.4 shows that extended radio sources may preferentially be oriented with their long axis perpendicular to the cluster radius, *i.e.* $|\varphi| \simeq \pi/2$, but this result is of low significance, based on only several low-declination (see Fig. 14) sources.

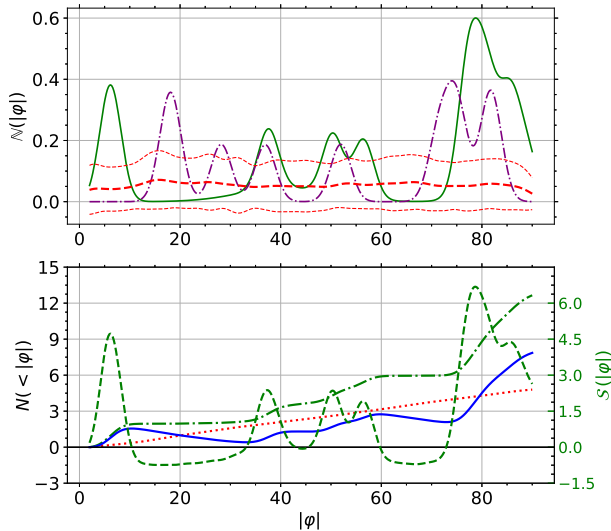


FIG. E.4. Distribution of the angle $\mathbb{P} = |\varphi|$ between source elongation and cluster radius, as in Fig. 14, but for extended, $\theta_a > 60''$ sources.

Finally, we examine the excess radio sources at lower frequencies, using the GMRT and VLSSr catalogs. Comparing the stacked profiles of NVSS, GMRT, and VLSSr sources in Fig. E.5 suggests that the signal may be broadened at 74 MHz, as expected due to the enhanced cooling length, but the effect is of low significance due to the poor statistics of stacking the smaller, low-frequency catalogs. Similarly, Fig. E.6 suggests that the luminosity of the excess GMRT sources is $\nu L_\nu(150 \text{ MHz}) \simeq 5 \times 10^{39-40} \text{ erg s}^{-1}$, as expected based on the NVSS luminosities and the GMRT–NVSS spectra, but again, the low-frequency statistics are poor.

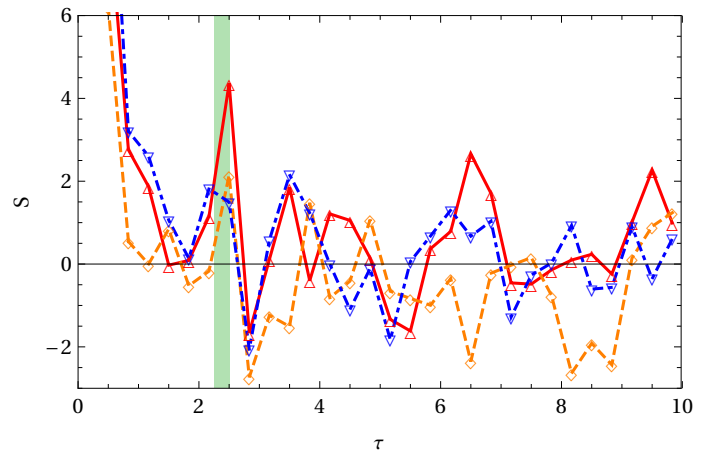


FIG. E.5. Significance $S(\tau)$ profiles of SW-stacked NVSS (red up triangles), GMRT (orange diamonds), and VLSSr (blue down triangles) sources around the same clusters used for the NVSS sample. A low, $\Delta\tau = 1/3$ resolution is used here, due to the smaller low-frequency catalogs.

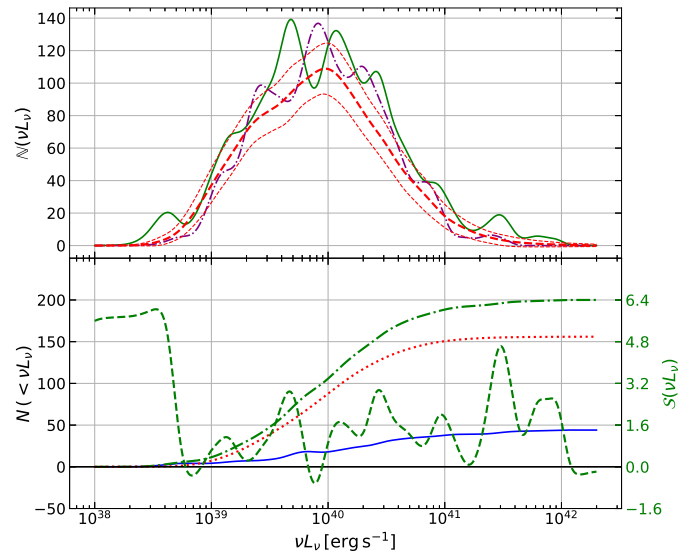


FIG. E.6. Same luminosity $\mathbb{P} = \log_{10} \nu L_\nu$ distribution as in Fig. 8, but for GMRT sources, around the same clusters as in the NVSS sample.

Appendix F: No significant 2RXS-NVSS pair excess

In search of excess VS sources that radiate both in X-rays and in radio, we construct a catalog of 2RXS–NVSS pairs with an angular separation $< 1'$, chosen such that $< 30\%$ of these pairs are likely to be coincidental projected overlaps. Stacking these pairs around our MCXC cluster sample does not produce a robust VS signal, as demonstrated in Fig. G.1. We conclude that the X-ray and radio excess VS signals are not dominated by the same individual objects.

Appendix G: Excess sources are not identified AGN

We examine the possible association of excess VS sources with previously-identified AGN. For X-rays, 2RXS already provides associations with an AGN catalog [4], whereas in radio, we cross-correlate NVSS with the same catalog using a proximity criterion of $< 3'$ angular separation. Almost all AGN associated with sources located in projection around an MCXC cluster are found to have redshifts inconsistent with the cluster. In addition, we find no significant difference in the results of stacking sources with vs. without an AGN association. Hence, we can rule out the possibility that a significant fraction of the sources comprising the excess VS signal is associated with these identified AGN.

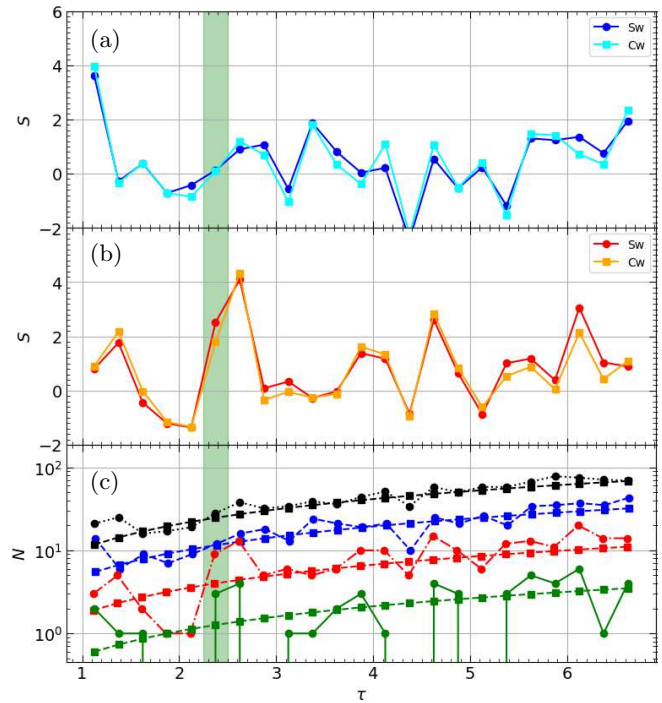


FIG. G.1. Excess significance $S(\tau)$ (panels a and b; see legends) and total number $N(\tau)$ (panel c; real pairs as disks with guidelines to the eye; expected field pairs as squares) profiles of 2RXS–NVSS pairs. Imposing the nominal flux cuts (solid green lines in panel c) leaves insufficient pairs. Relaxing F_{ν}^* (panel a and dashed blue in panel c) yields no signal. Relaxing F_X^* (panel b and dot-dashed red in panel c) or both F_{ν}^* and F_X^* (dotted black in panel c) leaves strong fluctuations, with a $\tau > 2.5$ signal we cannot substantiate.

Appendix H: VS-region sources

Tables IV and V list respectively the 2RXS and NVSS sources found in the VS region, naming the cluster tentatively associated with each source. Note that statistically, only about $\sim 1/3$ of these sources are associated with the localized VS excess, the rest attributed to field (foreground or background) sources.

TABLE IV: 2RXS sources in the VS region

Source (1)	R.A. (2)	Dec (3)	Cluster (4)	Alt. name (5)	z (6)
2RXS J213734.6-720725	324.3927	-72.1233	MCXC J2133.4-7156		0.0559
2RXS J043118.7-620535	67.8281	-62.0940	MCXC J0431.4-6126	A3266	0.0589
2RXS J034914.6-544813	57.3109	-54.8043	MCXC J0352.3-5453	RBS 0485	0.0447
2RXS J034324.8-530041	55.8534	-53.0122	MCXC J0342.8-5338	A3158	0.0590
2RXS J034517.9-530544	56.3248	-53.0963	MCXC J0342.8-5338	A3158	0.0590
2RXS J033852.2-532427	54.7174	-53.4082	MCXC J0342.8-5338	A3158	0.0590
2RXS J034710.8-533449	56.7951	-53.5811	MCXC J0342.8-5338	A3158	0.0590
2RXS J034329.7-541259	55.8740	-54.2171	MCXC J0342.8-5338	A3158	0.0590
2RXS J224403.1-525611	341.0127	-52.9362	MCXC J2246.3-5243	A3911	0.0965
2RXS J032345.2-513226	50.9385	-51.5412	MCXC J0321.9-5119	A3120	0.0696
2RXS J032133.8-514003	50.3907	-51.6683	MCXC J0321.9-5119	A3120	0.0696
2RXS J024638.7-461700	41.6615	-46.2840	MCXC J0245.2-4627	A3047	0.0868

Continued on next page

TABLE IV – continued from previous page

Source	R.A.	Dec	Cluster	Alt. name	z
2RXS J034211.4-455724	55.5477	-45.9575	MCXC J0340.8-4542	RBS 0459	0.0698
2RXS J224909.0-453551	342.2874	-45.5975	MCXC J2250.8-4521	S1067	0.0511
2RXS J232040.0-424706	350.1665	-42.7850	MCXC J2319.1-4206	ACOS1111	0.0450
2RXS J225144.6-371317	342.9362	-37.2214	MCXC J2249.2-3727	S1065	0.0289
2RXS J225159.4-373447	342.9978	-37.5797	MCXC J2249.2-3727	S1065	0.0289
2RXS J053523.7-362736	83.8495	-36.4610	MCXC J0533.3-3619	S0535	0.0479
2RXS J235847.4-340950	359.6976	-34.1640	MCXC J2357.0-3445	A4059	0.0475
2RXS J000606.1-350150	1.5255	-35.0306	MCXC J0006.0-3443	A2721	0.1147
2RXS J002301.4-330721	5.7563	-33.1225	MCXC J0025.5-3302	S0041	0.0491
2RXS J052401.7-320833	81.0078	-32.1435	MCXC J0525.5-3135	A3341	0.0380
2RXS J040615.2-304956	61.5638	-30.8330	MCXC J0408.2-3053	A3223	0.0600
2RXS J001131.5-282046	2.8817	-28.3462	MCXC J0011.3-2851	A2734	0.0620
2RXS J001247.7-291301	3.1991	-29.2171	MCXC J0011.3-2851	A2734	0.0620
2RXS J005049.8-284533	12.7079	-28.7594	MCXC J0051.3-2831	A2829	0.1125
2RXS J024421.9-262500	41.0917	-26.4172	MCXC J0244.1-2611		0.1362
2RXS J001358.9-233820	3.4958	-23.6391	MCXC J0015.4-2350	A14	0.0645
2RXS J010013.3-215003	15.0559	-21.8344	MCXC J0102.7-2152	A0133	0.0569
2RXS J005002.6-212709	12.5111	-21.4528	MCXC J0048.6-2114	A2824	0.0581
2RXS J215644.7-201430	329.1866	-20.2414	MCXC J2158.3-2006	A2401	0.0570
2RXS J045714.9-181757	74.3127	-18.3002	MCXC J0454.8-1806	CID 28	0.0335
2RXS J011459.1-153909	18.7467	-15.6530	MCXC J0116.1-1555	SCG 16	0.0448
2RXS J010832.7-155511	17.1369	-15.9202	MCXC J0108.9-1537	A0151S	0.0970
2RXS J010905.1-145729	17.2717	-14.9584	MCXC J0108.8-1524	A0151N	0.0533
2RXS J011029.5-151015	17.6233	-15.1712	MCXC J0108.8-1524	A0151N	0.0533
2RXS J005725.1-142056	14.3552	-14.3492	MCXC J0058.4-1425	A123	0.0957
2RXS J103914.9-090431	159.8131	-9.0757	MCXC J1039.7-0841	A1069	0.0650
2RXS J101848.3-062729	154.7021	-6.4585	MCXC J1020.4-0631	A0978	0.0540
2RXS J234648.0-014221	356.7006	-1.7059	MCXC J2347.4-0218	HCG 97	0.0223
2RXS J003606.6-021227	9.0281	-2.2078	MCXC J0034.6-0208		0.0812
2RXS J003545.5-020703	8.9403	-2.1178	MCXC J0034.2-0204	SH518	0.0822
2RXS J011731.8+002126	19.3833	0.3570	MCXC J0115.2+0019	A0168	0.0450
2RXS J011326.7+000035	18.3620	0.0095	MCXC J0115.2+0019	A0168	0.0450
2RXS J011703.9+000025	19.2671	0.0069	MCXC J0115.2+0019	A0168	0.0450
2RXS J213637.9+004203	324.1585	0.7016	MCXC J2137.1+0026	VMF98 202	0.0509
2RXS J013243.2+004109	23.1806	0.6856	MCXC J0131.7+0033	A208	0.0798
2RXS J013038.7+004006	22.6622	0.6683	MCXC J0131.7+0033	A208	0.0798
2RXS J010620.9+022017	16.5877	2.3380	MCXC J0108.1+0210	A0147	0.0436
2RXS J121929.8+034850	184.8748	3.8140	MCXC J1217.6+0339	ZW 1215.1+0400	0.0766
2RXS J122710.3+090646	186.7935	9.1131	MCXC J1227.4+0849	A1541	0.0896
2RXS J025806.4+093216	44.5277	9.5373	MCXC J0255.8+0918	IC 1867	0.0258
2RXS J110233.0+105722	165.6382	10.9561	MCXC J1100.8+1033	A1142	0.0353
2RXS J235542.9+114259	358.9297	11.7166	MCXC J2355.6+1120	A2675	0.0726
2RXS J224939.6+110016	342.4157	11.0048	MCXC J2250.0+1137	RX J2250.0+1137	0.0255
2RXS J114410.5+151430	176.0442	15.2417	MCXC J1145.3+1529	A1371	0.0670
2RXS J011459.8+152854	18.7499	15.4816	MCXC J0113.0+1531	A0160	0.0442
2RXS J145502.0+164416	223.7590	16.7386	MCXC J1454.4+1622		0.0456
2RXS J145502.0+164416	223.7590	16.7386	MCXC J1452.9+1641	A1983	0.0444
2RXS J145427.1+162242	223.6136	16.3790	MCXC J1452.9+1641	A1983	0.0444
2RXS J160624.0+181522	241.6005	18.2569	MCXC J1604.5+1743	A2151A	0.0370
2RXS J160726.2+175017	241.8596	17.8390	MCXC J1604.5+1743	A2151A	0.0370
2RXS J160624.0+181522	241.6005	18.2569	MCXC J1606.8+1746	A2151B	0.0321
2RXS J124142.2+181103	190.4265	18.1845	MCXC J1241.3+1834	A1589	0.0730
2RXS J232047.5+182931	350.1989	18.4924	MCXC J2318.5+1842	A2572	0.0403
2RXS J232047.5+182931	350.1989	18.4924	MCXC J2318.4+1843	A2572B	0.0389
2RXS J111124.7+212406	167.8532	21.4016	MCXC J1109.7+2145	A1177	0.0319
2RXS J112204.0+245206	170.5169	24.8684	MCXC J1122.3+2419	HCG 51	0.0258
2RXS J083659.6+243500	129.2488	24.5828	MCXC J0838.1+2506	CGCG120-014	0.0286
2RXS J142324.0+264159	215.8503	26.7003	MCXC J1423.1+2615	RX J1423.1+2616	0.0375
2RXS J134738.5+271451	206.9107	27.2479	MCXC J1348.8+2635	A1795	0.0622
2RXS J135006.7+271253	207.5284	27.2153	MCXC J1348.8+2635	A1795	0.0622
2RXS J134755.3+255544	206.9809	25.9292	MCXC J1348.8+2635	A1795	0.0622

Continued on next page

TABLE IV – continued from previous page

Source	R.A.	Dec	Cluster	Alt. name	z
2RXS J233319.1+271429	353.3308	27.2417	MCXC J2335.0+2722	A2622	0.0613
2RXS J152419.8+275742	231.0828	27.9625	MCXC J1522.4+2742	A2065	0.0723
2RXS J120914.3+280712	182.3100	28.1201	MCXC J1206.6+2811	NGC 4104	0.0283
2RXS J120745.5+273652	181.9399	27.6145	MCXC J1206.6+2811	NGC 4104	0.0283
2RXS J091750.4+341607	139.4603	34.2682	MCXC J0919.8+3345	A779	0.0230
2RXS J093429.7+333438	143.6241	33.5770	MCXC J0933.4+3403	UGC 05088	0.0269
2RXS J133712.0+344230	204.3001	34.7087	MCXC J1334.3+3441	NGC 5223	0.0240
2RXS J102045.2+381116	155.1885	38.1876	MCXC J1022.0+3830	RX J1022.1+3830	0.0491
2RXS J102128.8+380655	155.3702	38.1150	MCXC J1022.0+3830	RX J1022.1+3830	0.0491
2RXS J131156.8+385139	197.9870	38.8612	MCXC J1311.1+3913	A1691	0.0720
2RXS J120722.0+385213	181.8417	38.8705	MCXC J1205.2+3920	RX J1205.1+3920	0.0381
2RXS J171026.5+400332	257.6108	40.0598	MCXC J1711.0+3941	A2250	0.0647
2RXS J163031.2+410137	247.6304	41.0277	MCXC J1627.6+4055	A2197	0.0301
2RXS J162959.4+423008	247.4980	42.5030	MCXC J1627.3+4240	A2192	0.0317
2RXS J141348.9+440015	213.4539	44.0047	MCXC J1413.7+4339	A1885	0.0890
2RXS J141229.3+435534	213.1223	43.9267	MCXC J1413.7+4339	A1885	0.0890
2RXS J171124.1+434903	257.8508	43.8184	MCXC J1714.3+4341	NGC 6329	0.0276
2RXS J152115.3+485847	230.3139	48.9806	MCXC J1520.9+4840	A2064	0.1076
2RXS J113803.7+490500	174.5151	49.0835	MCXC J1134.8+4903	A1314	0.0341
2RXS J113408.7+483414	173.5360	48.5705	MCXC J1134.8+4903	A1314	0.0341
2RXS J161157.2+490138	242.9884	49.0280	MCXC J1614.1+4909	A2169	0.0579
2RXS J142404.6+493154	216.0190	49.5323	MCXC J1421.5+4933	ZW 1420.2+4952	0.0716
2RXS J142354.7+492828	215.9781	49.4749	MCXC J1421.5+4933	ZW 1420.2+4952	0.0716
2RXS J141945.7+491822	214.9405	49.3067	MCXC J1421.5+4933	ZW 1420.2+4952	0.0716
2RXS J102406.0+500302	156.0250	50.0504	MCXC J1022.5+5006	A980	0.1580
2RXS J100837.2+543735	152.1549	54.6262	MCXC J1010.2+5430	VMF98 84	0.0450
2RXS J105939.2+563211	164.9127	56.5363	MCXC J1058.4+5647	A1132	0.1369
2RXS J143027.2+565003	217.6129	56.8346	MCXC J1428.4+5652	A1925	0.1051
2RXS J162948.3+584616	247.4515	58.7720	MCXC J1629.7+5831	A2208	0.1329
2RXS J133520.4+584501	203.8343	58.7508	MCXC J1336.1+5912	A1767	0.0701
2RXS J170902.9+641730	257.2623	64.2925	MCXC J1712.7+6403	A2255	0.0809
2RXS J171640.0+641048	259.1670	64.1808	MCXC J1712.7+6403	A2255	0.0809
2RXS J171708.3+640146	259.2850	64.0304	MCXC J1712.7+6403	A2255	0.0809
2RXS J175341.7+654242	268.4244	65.7126	MCXC J1751.1+6531	NGC6505	0.0428
2RXS J174833.2+652351	267.1389	65.3985	MCXC J1751.1+6531	NGC6505	0.0428
2RXS J113146.0+660731	172.9404	66.1254	MCXC J1133.2+6622	A1302	0.1160
2RXS J174532.3+674811	266.3849	67.8039	MCXC J1742.7+6735		0.0420
2RXS J174603.5+672706	266.5151	67.4525	MCXC J1742.7+6735		0.0420
2RXS J175614.0+680708	269.0588	68.1198	MCXC J1755.7+6752		0.0833
2RXS J173039.0+681130	262.6628	68.1925	MCXC J1736.3+6803	ZW 1745.6+6703	0.0248
2RXS J174241.6+680013	265.6739	68.0045	MCXC J1736.3+6803	ZW 1745.6+6703	0.0248
2RXS J170234.2+681129	255.6427	68.1922	MCXC J1659.6+6826		0.0504
2RXS J170102.2+680513	255.2593	68.0878	MCXC J1659.6+6826		0.0504
2RXS J172207.7+694303	260.5323	69.7183	MCXC J1724.2+6956		0.0386
2RXS J172400.1+694026	261.0006	69.6749	MCXC J1724.2+6956		0.0386
2RXS J115509.4+734312	178.7870	73.7202	MCXC J1156.0+7325	A1412	0.0830

Table columns: (1) Source name; (2) Right ascension (deg); (3) Declination (deg); (4) Name of tentatively-associated cluster; (5) Alternative cluster name; (6) Cluster redshift. Note that each of the two sources, 2RXS J145502.0+164416 and 2RXS J232047.5+182931, appears twice, as it falls in the VS radii of two clusters. Such double counting affects field sources, too, and has a negligible effect on our results.

TABLE V: NVSS sources in the VS region

Source	R.A.	Dec	Cluster	Alt. name	z
(1)	(2)	(3)	(4)	(5)	(6)
NVSS J000029-345224	0.1227	-34.8734	MCXC J2357.0-3445	A4059	0.0475
NVSS J011413-321800	18.5563	-32.3002	MCXC J0113.9-3145	S141A	0.0191
NVSS J011448-321951	18.7037	-32.3310	MCXC J0113.9-3145	S141A	0.0191
NVSS J011632-314001	19.1349	-31.6671	MCXC J0113.9-3145	S141A	0.0191

Continued on next page

TABLE V – continued from previous page

Source	R.A.	Dec	Cluster	Alt. name	z
NVSS J004839-294718	12.1645	-29.7885	MCXC J0049.4-2931	S0084	0.1084
NVSS J005037-292128	12.6577	-29.3578	MCXC J0049.4-2931	S0084	0.1084
NVSS J000956-282923	2.4846	-28.4898	MCXC J0011.3-2851	A2734	0.0620
NVSS J001001-282940	2.5052	-28.4944	MCXC J0011.3-2851	A2734	0.0620
NVSS J054438-253222	86.1613	-25.5395	MCXC J0545.4-2556	A0548W	0.0424
NVSS J054916-260421	87.3176	-26.0727	MCXC J0548.6-2527	A0548E	0.0420
NVSS J055016-255502	87.5699	-25.9173	MCXC J0548.6-2527	A0548E	0.0420
NVSS J001403-233834	3.5152	-23.6430	MCXC J0015.4-2350	A14	0.0645
NVSS J234326-215422	355.8610	-21.9062	MCXC J2344.4-2153	A2655	0.1122
NVSS J220245-214333	330.6908	-21.7259	MCXC J2203.8-2130		0.0732
NVSS J055158-211948	87.9928	-21.3302	MCXC J0552.8-2103	A0550	0.0989
NVSS J082717-202622	126.8221	-20.4397	MCXC J0826.7-2007	S611	0.0876
NVSS J215707-202441	329.2812	-20.4116	MCXC J2158.3-2006	A2401	0.0570
NVSS J023743-193235	39.4324	-19.5432	MCXC J0236.6-1923	A0367	0.0907
NVSS J221145-122639	332.9387	-12.4442	MCXC J2210.3-1210	A2420	0.0846
NVSS J091541-114807	138.9248	-11.8022	MCXC J0918.1-1205	A0780	0.0539
NVSS J104108-114139	160.2867	-11.6944	MCXC J1041.5-1123		0.0839
NVSS J221519-090004	333.8319	-9.0011	MCXC J2216.2-0920	A2428	0.0825
NVSS J094446-082722	146.1937	-8.4562	MCXC J0945.4-0839	A0868	0.1535
NVSS J205703-075258	314.2643	-7.8830	MCXC J2058.2-0745	A2331	0.0793
NVSS J234515-035930	356.3143	-3.9918	MCXC J2344.2-0422		0.0786
NVSS J033834-022200	54.6449	-2.3668	MCXC J0340.6-0239		0.0352
NVSS J003438-014309	8.6595	-1.7192	MCXC J0034.2-0204	SH518	0.0822
NVSS J222347-020135	335.9484	-2.0265	MCXC J2223.8-0138	A2440	0.0906
NVSS J101444-000417	153.6845	-0.0715	MCXC J1013.7-0006	A0954	0.0927
NVSS J234057+000447	355.2402	0.0797	MCXC J2341.1+0018		0.1100
NVSS J011546+005204	18.9441	0.8679	MCXC J0115.2+0019	A0168	0.0450
NVSS J213638+004154	324.1607	0.6985	MCXC J2137.1+0026	VMF98 202	0.0509
NVSS J101135+005747	152.8969	0.9631	MCXC J1013.6-0054	A0957	0.0445
NVSS J091800+003450	139.5004	0.5808	MCXC J0920.0+0102	MKW 1S	0.0175
NVSS J092035+002330	140.1490	0.3918	MCXC J0920.0+0102	MKW 1S	0.0175
NVSS J092124+013834	140.3506	1.6428	MCXC J0920.0+0102	MKW 1S	0.0175
NVSS J023101+014958	37.7542	1.8330	MCXC J0231.9+0114	RCS145	0.0221
NVSS J102710+033927	156.7941	3.6577	MCXC J1028.3+0346	A1024	0.0730
NVSS J235254+060033	358.2277	6.0092	MCXC J2350.8+0609	A2665	0.0562
NVSS J003808+071223	9.5341	7.2066	MCXC J0040.0+0649	A76	0.0395
NVSS J082152+080430	125.4679	8.0751	MCXC J0821.0+0751	RX J0820.9+0751	0.1100
NVSS J122631+090037	186.6315	9.0105	MCXC J1227.4+0849	A1541	0.0896
NVSS J041528+103317	63.8691	10.5548	MCXC J0413.4+1028	A0478	0.0882
NVSS J114049+105754	175.2069	10.9651	MCXC J1141.2+1044	A1345	0.1090
NVSS J122901+120012	187.2546	12.0034	MCXC J1229.9+1147	A1552	0.0852
NVSS J122935+120548	187.3960	12.0968	MCXC J1229.9+1147	A1552	0.0852
NVSS J123056+115933	187.7336	11.9927	MCXC J1229.9+1147	A1552	0.0852
NVSS J025829+133328	44.6227	13.5579	MCXC J0257.8+1302	A0399	0.0722
NVSS J025831+133417	44.6329	13.5715	MCXC J0257.8+1302	A0399	0.0722
NVSS J025914+132735	44.8122	13.4598	MCXC J0257.8+1302	A0399	0.0722
NVSS J025634+133435	44.1457	13.5765	MCXC J0258.9+1334	A0401	0.0739
NVSS J232309+140444	350.7902	14.0789	MCXC J2324.3+1439	A2593	0.0428
NVSS J091204+161829	138.0167	16.3083	MCXC J0912.4+1556	A763	0.0851
NVSS J145602+162702	224.0084	16.4508	MCXC J1454.4+1622		0.0456
NVSS J145605+162652	224.0235	16.4480	MCXC J1454.4+1622		0.0456
NVSS J145608+162646	224.0339	16.4462	MCXC J1454.4+1622		0.0456
NVSS J123535+164732	188.8974	16.7924	MCXC J1236.4+1631	A1569	0.0780
NVSS J145420+162055	223.5846	16.3488	MCXC J1452.9+1641	A1983	0.0444
NVSS J145430+162250	223.6253	16.3806	MCXC J1452.9+1641	A1983	0.0444
NVSS J232609+171745	351.5393	17.2960	MCXC J2323.8+1648	A2589	0.0416
NVSS J160148+175401	240.4511	17.9004	MCXC J1604.5+1743	A2151A	0.0370
NVSS J160616+181459	241.5669	18.2498	MCXC J1604.5+1743	A2151A	0.0370
NVSS J160616+181459	241.5669	18.2498	MCXC J1606.8+1746	A2151B	0.0321
NVSS J075000+182311	117.5014	18.3866	MCXC J0748.1+1832		0.0400
NVSS J231822+191452	349.5954	19.2478	MCXC J2317.1+1841	A2572A	0.0422

Continued on next page

TABLE V – continued from previous page

Source	R.A.	Dec	Cluster	Alt. name	z
NVSS J232046+182925	350.1948	18.4905	MCXC J2318.5+1842	A2572	0.0403
NVSS J232046+182925	350.1948	18.4905	MCXC J2318.4+1843	A2572B	0.0389
NVSS J003912+213405	9.8002	21.5681	MCXC J0039.6+2114	A0075	0.0619
NVSS J104702+221033	161.7617	22.1761	MCXC J1048.7+2214	A1100	0.0450
NVSS J115427+233804	178.6144	23.6346	MCXC J1155.3+2324	A1413	0.1427
NVSS J160212+241010	240.5525	24.1695	MCXC J1604.9+2355	AWM 4	0.0326
NVSS J115752+240748	179.4701	24.1302	MCXC J1156.9+2415	ZWCL4673	0.1392
NVSS J112145+245201	170.4414	24.8672	MCXC J1122.3+2419	HCG 51	0.0258
NVSS J112331+235047	170.8832	23.8465	MCXC J1122.3+2419	HCG 51	0.0258
NVSS J005122+242232	12.8430	24.3756	MCXC J0049.8+2426	A104	0.0815
NVSS J204130+244822	310.3752	24.8062	MCXC J2042.1+2426		0.1019
NVSS J204140+244924	310.4190	24.8234	MCXC J2042.1+2426		0.1019
NVSS J005655+263125	14.2296	26.5236	MCXC J0055.9+2622	A115	0.1971
NVSS J134612+261413	206.5509	26.2371	MCXC J1348.8+2635	A1795	0.0622
NVSS J134756+255812	206.9839	25.9702	MCXC J1348.8+2635	A1795	0.0622
NVSS J135011+271338	207.5472	27.2275	MCXC J1348.8+2635	A1795	0.0622
NVSS J172026+265456	260.1105	26.9157	MCXC J1720.1+2637	RX J1720.1+2638	0.1644
NVSS J005654+270909	14.2266	27.1527	MCXC J0058.9+2657	RX J0058.9+2657	0.0451
NVSS J111018+292016	167.5758	29.3379	MCXC J1110.7+2842	A1185	0.0314
NVSS J075248+294630	118.2031	29.7750	MCXC J0753.4+2921	A602	0.0621
NVSS J004204+294712	10.5179	29.7869	MCXC J0040.4+2933	A0077	0.0712
NVSS J154034+310239	235.1442	31.0442	MCXC J1539.8+3043	A2110	0.0980
NVSS J015715+315417	29.3137	31.9049	MCXC J0157.4+3213	A278	0.0894
NVSS J170011+323533	255.0491	32.5926	MCXC J1659.0+3229		0.0621
NVSS J170013+322549	255.0566	32.4305	MCXC J1659.0+3229		0.0621
NVSS J132218+325254	200.5753	32.8818	MCXC J1320.2+3308	NGC 5098	0.0362
NVSS J160047+325445	240.1991	32.9126	MCXC J1600.3+3313	A2145	0.0880
NVSS J101735+334031	154.3995	33.6754	MCXC J1016.3+3338	A961	0.1240
NVSS J174018+350549	265.0763	35.0969	MCXC J1740.5+3538	RX J1740.5+3539	0.0428
NVSS J174132+360724	265.3845	36.1235	MCXC J1740.5+3538	RX J1740.5+3539	0.0428
NVSS J105544+374601	163.9356	37.7671	MCXC J1057.7+3738		0.0353
NVSS J185527+374256	283.8652	37.7156	MCXC J1857.6+3800		0.0567
NVSS J015823+413739	29.5992	41.6276	MCXC J0157.1+4120	A276	0.0810
NVSS J084513+423918	131.3047	42.6553	MCXC J0844.9+4258		0.0541
NVSS J171123+434842	257.8475	43.8118	MCXC J1714.3+4341	NGC 6329	0.0276
NVSS J171202+431555	258.0089	43.2653	MCXC J1714.3+4341	NGC 6329	0.0276
NVSS J171205+431701	258.0234	43.2839	MCXC J1714.3+4341	NGC 6329	0.0276
NVSS J063932+474721	99.8868	47.7892	MCXC J0638.1+4747	ZWCL 0634.1+4750	0.1740
NVSS J102310+475146	155.7940	47.8628	MCXC J1025.0+4750	A1003	0.0520
NVSS J090650+500334	136.7102	50.0597	MCXC J0907.8+4936	VV 196	0.0352
NVSS J180947+492544	272.4500	49.4291	MCXC J1811.0+4954	ZWCL8338	0.0501
NVSS J184203+502404	280.5142	50.4012	MCXC J1843.6+5021		0.1158
NVSS J164934+535817	252.3950	53.9716	MCXC J1649.2+5325	ARP 330, SHK 016	0.0290
NVSS J160016+533945	240.0697	53.6625	MCXC J1601.3+5354	A2149	0.1068
NVSS J124538+551134	191.4106	55.1929	MCXC J1247.3+5500	A1616	0.0830
NVSS J134442+555313	206.1759	55.8870	MCXC J1343.7+5538	A1783	0.0766
NVSS J114558+552222	176.4947	55.3730	MCXC J1147.3+5544	A1377	0.0510
NVSS J142824+563611	217.1032	56.6032	MCXC J1428.4+5652	A1925	0.1051
NVSS J172338+562857	260.9112	56.4827	MCXC J1723.3+5658	NGC 6370	0.0272
NVSS J165438+583617	253.6584	58.6047	MCXC J1654.7+5854	A2239	0.0869
NVSS J175341+654238	268.4246	65.7108	MCXC J1751.1+6531	NGC6505	0.0428
NVSS J163540+655813	248.9171	65.9705	MCXC J1635.8+6612	A2218	0.1709
NVSS J113025+662605	172.6060	66.4349	MCXC J1133.2+6622	A1302	0.1160
NVSS J072754+665812	111.9751	66.9701	MCXC J0724.9+6658	A0578	0.0863
NVSS J062025+673640	95.1045	67.6111	MCXC J0618.6+6724	A0554	0.1127
NVSS J175049+680826	267.7083	68.1406	MCXC J1754.6+6803	ZW 1754.5+6807	0.0770
NVSS J173339+683557	263.4159	68.5994	MCXC J1736.3+6803	ZW 1745.6+6703	0.0248
NVSS J185609+680634	284.0397	68.1095	MCXC J1853.9+6822	A2312	0.0928
NVSS J181702+694125	274.2606	69.6904	MCXC J1814.2+6939	A2301	0.0863
NVSS J185101+732316	282.7568	73.3879	MCXC J1847.2+7320	A2310	0.1125
NVSS J115626+730650	179.1125	73.1141	MCXC J1156.0+7325	A1412	0.0830

Continued on next page

TABLE V – continued from previous page

Source	R.A.	Dec	Cluster	Alt. name	z
NVSS J171206+774613	258.0265	77.7704	MCXC J1718.1+7801	A2271	0.0584
NVSS J165135+782853	252.8989	78.4815	MCXC J1703.8+7838	A2256	0.0581

Table columns: (1) Source name; (2) Right ascension (deg); (3) Declination (deg); (4) Name of tentatively-associated cluster; (5) Alternative cluster name; (6) Cluster redshift. Note that the source NVSS J160616+181459 appears twice, as it falls in the VS radius of two clusters.

-
- [1] F. Boese and S. Doebereiner, *Astronomy & Astrophysics* **370**, 649 (2001).
[2] F. Boese, *Astronomy and Astrophysics Supplement Series* **141**, 507 (2000).
[3] S. S. Wilks, *The Annals of Mathematical Statistics* **9**, 60 (1938).
[4] M. P. Véron-Cetty and P. Véron, *A&A* **518**, A10 (2010).